

5-2023

Understanding and Tuning Magnetism in van der Waals Magnetic Compounds

Rabindra Basnet
University of Arkansas-Fayetteville

Follow this and additional works at: <https://scholarworks.uark.edu/etd>



Part of the [Condensed Matter Physics Commons](#), and the [Materials Science and Engineering Commons](#)

Citation

Basnet, R. (2023). Understanding and Tuning Magnetism in van der Waals Magnetic Compounds. *Graduate Theses and Dissertations* Retrieved from <https://scholarworks.uark.edu/etd/5068>

This Dissertation is brought to you for free and open access by ScholarWorks@UARK. It has been accepted for inclusion in Graduate Theses and Dissertations by an authorized administrator of ScholarWorks@UARK. For more information, please contact scholar@uark.edu.

Understanding and Tuning Magnetism in van der Waals Magnetic Compounds

A dissertation submitted in partial fulfillment
of the requirements for the degree of
Doctor of Philosophy in Physics

by

Rabindra Basnet
Tribhuvan University
Bachelor of Science in Physics, 2012
Tribhuvan University
Master of Science in Physics, 2016

May 2023
University of Arkansas

This dissertation is approved for recommendation to the Graduate Council.

Jin Hu, Ph.D.
Dissertation Director

Hugh O. H. Churchill, Ph.D.
Committee Member

Yong Wang, Ph.D.
Committee Member

Abstract

The recently discovered two-dimensional (2D) magnetism has attracted intensive attention due to possible magnetic phenomenon arising from 2D magnetism and their promising potential for spintronics applications. The advances in 2D magnetism have motivated the study of layered magnetic materials, and further enhanced our ability to tune their magnetic properties. Among various layered magnets, tunable magnetism has been widely investigated in metal thiophosphates MPX_3 . It is a class of magnetic van der Waals (vdW) materials with antiferromagnetic ordering persisting down to atomically thin limit. Their magnetism originates from the localized moments due to $3d$ electrons in transition metal ions. So, their magnetic properties are strongly dependent on the choice of M .

With this motivation, we synthesized metal-substituted MPX_3 compounds such as $Ni_{1-x}Mn_xPS_3$ ($0 \leq x \leq 1$), $Ni_{1-x}Cr_xPS_3$ ($0 \leq x \leq 0.09$), and $Fe_{1-x}Mn_xPSe_3$ ($0 \leq x \leq 1$). The magnetic properties have been found to be very tunable with metal substitutions. Furthermore, we performed previously unexplored non-magnetic X substitution in $MnPS_{3-x}Se_x$ ($0 \leq x \leq 3$), $FePS_{3-x}Se_x$ ($0 \leq x \leq 3$), and $NiPS_{3-x}Se_x$ ($0 \leq x \leq 1.3$). Interestingly, such non-magnetic S-Se substitution also effectively modifies the magnetic exchange and anisotropy in MPX_3 . In addition to M and X substitutions, we conducted electrochemical intercalation of Li into $NiPS_3$. We found the emergence of ferrimagnetism at low temperature in Li-intercalated $NiPS_3$, which has never been observed due to substitution technique. Such efficient engineering of magnetism provides a suitable platform to understand low-dimensional magnetism and design future magnetic devices.

Acknowledgements

The journey of PhD has been long and arduous, yet a great opportunity to learn and develop as a professional in the field of science and technology. First, I would like to thank the Department of Physics at the University of Arkansas for selecting me for its graduate program in Fall 2017. Through its advanced teaching and research opportunities, the department of physics has offered me a suitable learning environment for deep understanding of physics.

I would like to deeply express my gratitude to Prof. Jin Hu for his generous support and caring mentorship. With no research experience when I first came to the USA, his invaluable guidance has been simply unparalleled and always motivated me to develop as a researcher. I would like to acknowledge the research facilities at the Institute of Nanoscience and Engineering at the University of Arkansas, without which nothing would have been possible. I would deeply thank Prof. Hugh Churchill and Prof. Yong Wang for being on all my annual reviews, qualifier, and dissertation committee. I would also like to thank Prof. Salvador Barraza-Lopez for being on my qualifier committee. Their tough questions and important suggestions during the presentation were very helpful to improve my presentation skill and identify fundamental research questions. I would like to thank Prof. Jie Xiao (Chemistry) and her former graduate student Dr. Joshua Lochala for granting me access to their lab, using her intercalation supplies, and helping with the electrochemical intercalation experiment. I would like to thank Dr. Mourad Benamara and Prof. Josh Sakon (Chemistry) for their training and helping with EDS and XRD measurements. I would acknowledge Prof. Churchill's Quantum device group for allowing me to work in their lab especially for growing nanostructures using CVD from very onset of my research starting from Dec 2017, and helping me with exfoliation, flake hunting, measurement, and gold coating of my samples. I greatly appreciate all the collaborators for contributing to my research: Prof. Jian Wang

(Crystal structure, Wichita State University), Fei Wang (Crystal structure, Missouri State University), Dr. Ivana Vobornik (ARPES, Institute of Materials (IOM)-CNR), Prof. Antonio Politano (ARPES, University of L'Aquila), Prof TeYu Chien (STM, University of Wyoming), Prof. Zhiqiang Mao (Transport and magnetization, Pennsylvania State University), Prof. Magdalena Birowska (Theory, Poland), and Prof. Carmine Autieri (Theory, Poland). Last but not least, I would like to thank all my former and current lab mates at Quantum materials research group for their daily support in my research. I would like to acknowledge Post doc Dr. Aaron Wegner; fellow graduate students Dr. Krishna Pandey, Gokul Acharya, Md Rafique Un Nabi, Santosh Karki Chhetri, Dinesh Upreti, and Sudip Acharya; undergraduate students Stephen Storment, Cory Stephenson, Brycelynn Bailey (REU 2019), Anna Corbitt (REU 2019), Dawn Ford (REU 2021), and Kaylee TenBarge (REU 2021); and high school students Sam Bishop (Haas Hall Academy) and Taksh Patel (Fayetteville High School).

Above all, I would like to wholeheartedly thank my parents for raising and motivating me to be a good person.

Table of Contents

Chapter 1: Introduction	Error! Bookmark not defined.
1.1 Background	Error! Bookmark not defined.
1.1.1 Families of layered magnetic materials.....	2
1.1.2 Type of magnetism.....	7
1.2. Antiferromagnetic van der Waals material (vdW) metal thiophosphates MPX_3 ($M =$ Transition metal and $X =$ Chalcogen).....	8
1.3. Tuning magnetism in MPX_3	16
Chapter 2: Experimental Methods	20
2.1 Single crystal Growth	20
2.1.1 Chemical vapor transport (CVT)	21
2.2 Electrochemical intercalation.....	23
2.3 Characterization	24
2.3.1 Energy-dispersive X-ray spectroscopy (EDS).....	24
2.3.2 X-ray diffraction (XRD)	25
2.3.3 Magnetization	26
2.3.4 Heat capacity.....	27
Chapter 3: Highly sensitive spin-flop transition in antiferromagnetic van der Waals material MPS_3 ($M = Ni$ and Mn).....	29
3.1 Introduction.....	29
3.2 Experiment.....	31
3.3 Results and Discussion	32
3.4 Conclusion	41
Chapter 4: Field-induced ferromagnetism in Cr-substituted antiferromagnetic van der Waals material $NiPS_3$	42
4.1 Introduction.....	42
4.2 Experiment.....	44

4.3 Result and discussion.....	44
4.4 Conclusion	52
Chapter 5: Controlling magnetic exchange and anisotropy by nonmagnetic ligand substitution in layered MPX_3 ($M = Ni, Mn; X = S, Se$).....	53
5.1. Introduction.....	53
5.2 Experiment.....	55
5.3 Results and Discussions.....	56
5.4 Conclusion	73
5.5 Appendix: Theoretical exchange couplings.....	73
Chapter 6: Understanding and tuning magnetism in layered Ising-type antiferromagnet $FePSe_3$ for potential 2D magnets	75
6.1 Introduction.....	75
6.2 Experiment.....	77
6.3 Results and Discussion	77
6.4 Conclusion.....	87
Chapter 7: Emergence of ferrimagnetism in Li-intercalated $NiPS_3$	88
7.1 Introduction.....	88
7.2 Experiment.....	90
7.3 Results and Discussion	90
7.4 Conclusion	103
Chapter 8: Conclusion and Outlook.....	104
References.....	107
Appendix A: All Publications Published, Submitted and Planned	131

List of Figures

Figure 1.1: Splitting of five $3d$ orbitals of transition metal cations into three t_{2g} and two e_g levels.....	3
Figure 1.2: Schematic of (a) isotropic exchange interaction, (b) anisotropic exchange interaction, and (c) single-ion anisotropy. In (a) and (b), the length of arrows represents strength of exchange interaction. In (c) the length of arrow denotes energy of magnetic moments along that direction.	6
Figure 1.3: Schematic of superexchange interaction between two cations through anion.....	7
Figure 1.4: Magnetic order for layered magnetic materials. (a) Ferromagnetic (FM) order. Left and right figures show interlayer and intralayer FM order, respectively. (b) A-type antiferromagnetic (AFM) order. (c) C- and G-type AFM order. From left to right: intralayer AFM-zigzag, AFM-stripy, and AFM-Néel order. Blue and pink color represent spin up and spin down, respectively.....	8
Figure 1.5: Crystal structures of MPX_3 . (a) MPX_3 materials exhibit common structural features with $(P_2X_6)^{4-}$ ($X = S$ or Se) anion sublattice within each layer. (b) Metal M arranged in a honeycomb lattice around the $(P_2X_6)^{4-}$ bipyramids. (c) Layered structure with finite van der Waals gap between the layers.....	10
Figure 1.6: Magnetic structures of various MPX_3 materials.....	12
Figure 1.7: Trigonal distortion in MPX_3 materials; z -axis is the trigonal axis.....	13
Figure 1.8: Conceptual schematic of metal substitution in MPX_3	17
Figure 1.9: Conceptual schematic of inter-layer intercalation in MPX_3	18
Figure 2.1: (a) Schematic of chemical vapor transport (CVT) growth. (b) Two-zone furnace used to grow single crystals of layered magnetic materials through CVT method. (c) Optical microscope images of various layered magnetic materials synthesized by CVT method.	22
Figure 2.2: (a) Electrochemical workstation used for intercalation. (b) Conceptual schematic of electrochemical intercalation of guest atoms into layered magnetic materials. (c) Homemade battery used for electrochemical intercalation.....	24
Figure 2.3: Schematic showing principle of Energy dispersive X-ray spectroscopy (EDS).....	25
Figure 2.4: Schematic showing principle of X-ray diffraction (XRD)	26
Figure 2.5: (a) Dynacool physical property measurement system (PPMS) from Quantum Design [92]. (b) Coil used for ACMS-II magnetization measurement in PPMS [92]	27
Figure 2.6: Schematic of sample platform for heat capacity measurement in PPMS [92].....	28

Figure 3.1: (a) Single-crystal x-ray-diffraction pattern for $\text{Ni}_{1-x}\text{Mn}_x\text{PS}_3$ showing the (00L) reflections. Right panels show (001) diffraction peak. Inset: Optical microscope images of the single crystals. (b) Crystal structure of MPS_3 ($M = \text{Ni}/\text{Mn}$) 32

Figure 3.2: Field induced spin flop transitions in pristine MnPS_3 and NiPS_3 . (a-b) Isothermal magnetization of MnPS_3 at different temperatures under (a) $H \perp ab$ and (b) $H \parallel ab$. Inset in (b): magnetic structure of MnPS_3 . (c-d) Isothermal magnetization of NiPS_3 at different temperatures under (a) $H \perp ab$ and (d) $H \parallel ab$. Upper inset in (c): 3D view of magnetic structure of NiPS_3 . Lower inset in (c): Top view of magnetic structure of NiPS_3 . Inset in (d): Isothermal magnetization at 50 – 140 K measured with $H \parallel ab$. The same color code is used to indicate temperatures for (a-d). (e) Isothermal magnetization at 2 K under $H \parallel ab$ with different in-plane field orientations. Inset: Optical microscope image of NiPS_3 single crystal with arrows pointing the applied field direction. (f) Temperature dependence of susceptibility of NiPS_3 measure with 1, 3, 5, 7, 8, and 9 T fields, measured with $H \parallel ab$. Inset: Temperature dependence of susceptibility at 9 T under $H \parallel ab$. The solid and dotted lines represent zero-field cooled (ZFC) and field-cooled (FC) data, respectively..... 34

Figure 3.3: (a-b) Isothermal magnetization of $\text{Ni}_{1-x}\text{Mn}_x\text{PS}_3$ samples ($0 \leq x \leq 1$) at $T = 2$ K under (a) $H \parallel ab$ and (b) $H \perp ab$. The same color code is used to indicate temperatures for (a) and (b). (c) Trigonal distortion in MPS_3 compounds. z -axis is the trigonal axis. (d) Isothermal magnetization of $\text{Ni}_{1-x}\text{Mn}_x\text{PS}_3$ ($x = 0$ and 0.05) at $T = 2$ K under $H \parallel ab$ (Left panel) and $H \perp ab$ (Right panel). Inset: zoom in of the low-field magnetization. (e) Isothermal magnetization of $\text{Ni}_{1-x}\text{Mn}_x\text{PS}_3$ ($x = 0.95$ and 1) at $T = 2$ K under $H \parallel ab$ (Left panel) and $H \perp ab$ (Right panel). Inset: zoom in of the low-field magnetization. 36

Figure 3.4: (a-c) Temperature dependence of out-of-plane ($H \perp ab$, red, upper panels) and in-plane ($H \parallel ab$, black, lower panels) susceptibilities of (a) $\text{Ni}_{0.95}\text{Mn}_{0.05}\text{PS}_3$, (b) $\text{Ni}_{0.1}\text{Mn}_{0.9}\text{PS}_3$, and (c) $\text{Ni}_{0.05}\text{Mn}_{0.95}\text{PS}_3$ samples. The dashed lines denote T_N . (d) Temperature dependence of heat capacity of $\text{Ni}_{1-x}\text{Mn}_x\text{PS}_3$ samples with $x = 0, 0.1, 0.2, 0.8$ and 1 . The black triangles denote T_N . Data are shifted for clarity. (e) Magnetic phase diagram of $\text{Ni}_{1-x}\text{Mn}_x\text{PS}_3$ ($0 \leq x \leq 1$). The transition temperatures are determined by susceptibility measurements on single- (χ -single crystal) and poly-crystals (χ -polycrystal), and heat capacity (C)..... 40

Figure 4.1: (a) Magnetic structure of NiPS_3 . (b) Optical microscope images of $\text{Ni}_{1-x}\text{Cr}_x\text{PS}_3$ single crystals. (c) Energy dispersive x-ray spectroscopy (EDS) spectra for $\text{Ni}_{1-x}\text{Cr}_x\text{PS}_3$ samples. (d) Powder x-ray-diffraction pattern for $\text{Ni}_{1-x}\text{Cr}_x\text{PS}_3$ samples..... 44

Figure 4.2: (a-b) Isothermal magnetization of $\text{Ni}_{1-x}\text{Cr}_x\text{PS}_3$ at $T = 2$ K under (a) $B \parallel ab$ and (b) $B \perp ab$. (c-d) Isothermal magnetization of $x = 0.09$ sample at different temperatures under (c) $B \parallel ab$ and (d) $B \perp ab$. The dashed lines denote B_{sat} . (e) Temperature dependence of susceptibility

(χ) at $B = 0.1$ T under $B||ab$ (Blue) and $B\perp ab$ (Red). The black triangles denote T_N . Inset: Temperature dependence of derivative $d\chi/dT$ 48

Figure 4.3: (a) Isothermal magnetization of $Ni_{1-x}Cr_xPS_3$ at $T = 2$ K under $B||ab$ (Blue) and $B\perp ab$ (Red) reproduced from Figure 4.2 (a and b). The blue and red arrows show spin-flop field (B_{SF}) under $B||ab$ and $B\perp ab$, respectively. The dashed lines guide to eye. (b) Doping dependence of B_{SF} 50

Figure 4.4: Conceptual schematic of moment reorientation in $NiPS_3$ with Cr substitution up to $x = 0.09$ in $Ni_{1-x}Cr_xPS_3$. For $x = 0.09$ sample, the evolution of moment orientation under in-plane and out of plane magnetic fields are demonstrated..... 51

Figure 5.1: (a) Crystal structure of MPX_3 ($M = Mn/Ni$; $X = S/Se$). (b) Optical microscope images of the as-grown single crystals and Single-crystal x-ray-diffraction pattern of $MnPS_{3-x}Se_x$ ($0 \leq x \leq 3$) showing the $(00L)$ reflections. Right panels show (002) diffraction peak. (c) Optical microscope images of the as-grown single crystals and Single-crystal x-ray-diffraction pattern of $NiPS_{3-x}Se_x$ ($0 \leq x \leq 1.3$) showing the $(00L)$ reflections. Right panels show (001) diffraction peak. The value of Se content x for each sample is determined by EDS..... 57

Figure 5.2: (a) Temperature dependence of out-of-plane ($H\perp ab$, red) and in-plane ($H||ab$, blue) molar susceptibility (χ) of $MnPS_{3-x}Se_x$ ($0 \leq x \leq 3$) samples. The black triangles denote T_N . (b) Temperature dependence of derivative $d\chi/dT$ of $MnPS_{3-x}Se_x$ samples. The dashed lines denote T_N . (c) Doping dependence of Néel temperature (T_N) for $MnPS_{3-x}Se_x$. (d) Magnetic structure of pristine $MnPS_3$ showing nearest-neighbor (J_1), second nearest-neighbor (J_2), and third nearest-neighbor (J_3) interactions..... 59

Figure 5.3: (a) Temperature dependence of out-of-plane ($H\perp ab$, red) and in-plane ($H||ab$, blue) molar susceptibility (χ) of $NiPS_{3-x}Se_x$ ($0 \leq x \leq 3$) samples. The dark yellow and wine color data represent $x = 2$ and 3 polycrystals samples, respectively. The black triangles denote T_N . (b) Temperature dependence of derivative $d\chi/dT$ of $NiPS_{3-x}Se_x$ samples. The dashed lines denote T_N . (c) Doping dependence of Néel temperature (T_N) of $NiPS_{3-x}Se_x$. (d) Magnetic structure of pristine $NiPS_3$ showing nearest-neighbor (J_1), second nearest-neighbor (J_2), and third nearest-neighbor (J_3) interactions..... 62

Figure 5.4: (a) Field dependence of magnetization of $MnPS_{3-x}Se_x$ samples ($0 \leq x \leq 3$) at $T = 2$ K for out-of-plane ($H\perp ab$, red) and in-plane ($H||ab$, blue) fields. Inset: Low-field magnetizations (b) Doping dependence of Spin-flop field (H_{SF}) of $MnPS_{3-x}Se_x$. (c) Magnetic structure of pristine $MnPS_3$. (d) Magnetic structure of pristine $MnPS_3$ 65

Figure 5.5: (a) Left: Energy difference between the particular direction of the spins and the magnetic ground state for $MnPS_3$ system including the SOC and neglecting the magnetic dipolar interactions within the DFT studies. The latter is crucial for the proper arrangement of the spins for this system. The θ angle indicates the rotation angle from out-of-plane to in-plane position.

Right: Schematic arrangement of the Mn spins in MnPS₃ structure. The theoretical studies predict the easy plane of magnetization in contradiction to the experimental results. (b) Left: Energy difference between the particular direction of the spins and the magnetic ground state for MnPSe₃ system. Right: Schematic arrangements of the Mn spins. Note, that the magnetic ordering within the layer exhibits AFM-Néel type of order, whereas the adjacent layers have antiferromagnetically aligned spins (reversed AFM-N). The easy plane of magnetization is predicted for this system..... 67

Figure 5.6: (a) Field dependence of magnetization of NiPS_{3-x}Se_x samples ($0 \leq x \leq 1.3$) at $T = 2$ K for out-of-plane ($H \perp ab$, red) and in-plane ($H \parallel ab$, blue) fields. The dashed lines are a guide to the eye. (b) Upper Panels: Energy difference between the particular directions of the spins and the magnetic ground state for NiPS₃ and NiPSe₃ using DFT calculations. The spins of the Ni atoms are collinearly aligned. The θ angle indicates the rotation angle from out-of-plane to in-plane position. The changes in rotation angle within the layer are negligible (negligible difference between the spins oriented in a and b directions). Lower Panels: Schematic pictures of magnetic spins for NiPS₃ and NiPSe₃. Note that, the NiPS₃ exhibits an easy plane (XY) of magnetization, whereas the NiPSe₃ has an easy axis oriented perpendicular to the layer..... 71

Figure 6.1: (a) Magnetic structures of MPSe₃ (M = Fe/Mn). (b) Powder x-ray-diffraction pattern of FePS_{3-x}Se_x ($0 \leq x \leq 3$) (upper panel) and Fe_{1-x}Mn_xPSe₃ ($0 \leq x \leq 1$) (lower panel)..... 78

Figure 6.2: (a) Temperature dependence of out-of-plane ($B \perp ab$, solid line) and in-plane ($B \parallel ab$, dashed line) susceptibility (χ) of (a) FePSe_{3-x}S_x ($0 \leq x \leq 3$) and (b) Fe_{1-x}Mn_xPSe₃ ($0 \leq x \leq 1$) samples. The black triangles denote Néel temperature (T_N)..... 81

Figure 6.3: Field dependence of magnetization of (a) FePS_{3-x}Se_x ($0 \leq x \leq 3$) (b) Fe_{1-x}Mn_xPSe₃ ($0 \leq x \leq 1$) samples at $T = 2$ K for out-of-plane ($B \perp ab$, solid line) and in-plane ($B \parallel ab$, dashed line) fields. Inset: Low-field magnetizations..... 84

Figure 6.4: (a) Temperature dependence of derivative $d\chi/dT$ of FePS_{3-x}Se_x ($0 \leq x \leq 3$) (upper panel) and Fe_{1-x}Mn_xPSe₃ ($0 \leq x \leq 1$) (lower panel) samples. (b) Doping dependence of Fe-Fe distance (upper panel) and Néel temperature (T_N) (lower panel) for FePS_{3-x}Se_x. (c) Doping dependence of T_N for Fe_{1-x}Mn_xPSe₃. (d) Magnetic structure of pristine FeP(S/Se)₃ showing nearest-neighbor (J_1), second nearest-neighbor (J_2), and third nearest-neighbor (J_3) interactions..... 87

Figure 7.1: (a) Conceptual schematic of electrochemical intercalation process. (b) Schematic of a coin cell used for electrochemical intercalation (Left image). Optical image of an electrochemical coin cell used for intercalation (Right image). (c) Discharge curves showing cell voltage (voltage vs Li/Li⁺) as a function of Li content (x) for Li_xNiPS₃ ($0.1 \leq x \leq 0.6$) single crystals. (d) Optical microscope (Left panel) and scanning electron microscope (SEM) (Right panel) images of the pristine and intercalated single crystals..... 91

Figure 7.2: (a) Single-crystal x-ray-diffraction pattern of Li_xNiPS_3 ($0 \leq x \leq 0.6$) showing the (00L) reflections. Right panels show (001) diffraction peak. (b) Evolution of inter-layer distance with Li content (x). (c) Schematic of the expanding inter-layer spacing upon Li intercalation... 95

Figure 7.3: (a) Field dependence of magnetization of Li_xNiPS_3 ($0 \leq x \leq 0.4$) at $T = 2$ K for out-of-plane ($H \perp ab$, red) and in-plane ($H \parallel ab$, blue) fields. The dashed lines are guide to eye. (b) Low field magnetization of Li_xNiPS_3 ($0 \leq x \leq 0.4$) at $T = 2$ K. (c) Field dependence of magnetization of Li_xNiPS_3 ($0.1 \leq x \leq 0.4$) at $T = 2$ K for in-plane fields after subtraction of linear magnetization background. (d) Evolution of saturation moment (μ_{sat}) (left axis) and coercive fields (H_c) (right axis) with Li content x 97

Figure 7.4: (a) Temperature dependence of out-of-plane ($H \perp ab$, red) and in-plane ($H \parallel ab$, blue) molar susceptibility (χ) of Li_xNiPS_3 ($0 \leq x \leq 0.4$) samples. The black triangles denote T_N . (b) Temperature dependence of out-of-plane ($H \perp ab$, red) and in-plane ($H \parallel ab$, blue) molar susceptibility χ of Li_xNiPS_3 ($0 \leq x \leq 0.4$) samples in the temperature range 100-200 K..... 99

Figure 7.5: (a) Temperature dependence of specific heat capacity of Li_xNiPS_3 ($0 \leq x \leq 0.4$) samples. The black triangles denote T_N . (b) Low temperature specific heat capacity of Li_xNiPS_3 ($0 \leq x \leq 0.4$) samples. (c) C/T vs T^2 data plotted for $x = 0$ and 0.1 samples with linear fits (Black solid lines) to $C/T = \gamma + \beta T^2$ 100

Figure 7.6: In-plane magnetic structure of pristine NiPS_3 showing two antiferromagnetically aligned Ni chains. The total magnetic moments of these chains become unequal upon Li intercalation..... 102

List of Tables

Table 1: Summary of layered magnetic materials.....	2
Table 2: Orbital occupancy for $3d$ valence electrons of various transition metal cations.....	4
Table 3: Information about crystal structure and magnetism for MPX_3 materials [28, 29]	10
Table 4: Magnetic exchange and anisotropy parameters for MPX_3 materials. Here, negative and positive signs denote AFM and FM interactions, respectively.....	15
Table 5: The exchange couplings J_i , the strength of a single ion anisotropy A and M - X - M bond angle using DFT calculations assuming the experimental lattice parameters. Positive (negative) values of J_i and A indicate the FM (AFM) couplings and out-of-plane (in-plane) direction of spins, respectively. The critical temperature is evaluated in mean-field approach.....	63

Chapter 1: Introduction

1.1 Background

Since the discovery of graphene in 2004 [1], numerous families of two-dimensional (2D) materials have been theoretically predicted and experimentally realized. For a long time, the 2D material research was mainly focused on the study of graphene family and transition metal dichalcogenides (TMDs). These 2D materials were widely used for the investigation of electronic properties because they display almost all functionalities of solid-state systems such as metal, semimetal, semiconductor, insulator, and superconductor, As well as various quantum phases such as superconductivity, charge density wave, and Dirac and Weyl semimetal. Due to fundamental scientific interest of low dimensional magnetism and technological demands of spintronics, the incorporation of magnetism in 2D materials has become imperative more than ever. This has led to the efforts to induce magnetism in graphene [2] and TMDs [3–5]. Given their non-magnetic nature, the magnetism in these materials mainly resulted from defects or doping of guest atoms. So, there has been an intensive search for 2D materials with intrinsic magnetism.

Recently, there have been breakthroughs in 2D magnetic materials which open a new route to explore intrinsic magnetism in true 2D limit. The discoveries of novel 2D magnets [6–11] provide opportunities to understand the mechanism of low dimensional magnetism as well as to develop applications based on the integration of 2D magnetic layers into next-generation devices. The integration of 2D magnets in nanodevices and heterostructures has also provided the platform to investigate their magnetic and electronic properties, and further improved our ability to tune them [12–24]. Such developments in 2D magnetism have motivated the search for

novel magnetic van der Waals (vdW) materials to explore the low-dimensional magnetism in real materials.

1.1.1 Families of layered magnetic materials

Various van der Waals (vdWs) materials hosting stable long-range magnetic orders have been recently discovered. There is a rich collection of vdW magnetic materials that possess a wide range of magnetic properties. So far, these materials can be broadly divided into two large families: (1) transition metal halides (consists of both dihalides and trihalides) and (2) transition metal chalcogenides (including both binary and ternary chalcogenides), which are summarized in Table 1. These transition metals ranging from V to Ni (i.e., V, Cr, Mn, Fe, Co, and Ni) in 3d transition metal row of the periodic table. Most of these materials are semiconductors with bandgap ranging from the near-infrared to the ultraviolet spectral range, while a few such as Fe_3GeTe_2 , and MnBi_2Te_4 are metallic [25,26].

Table 1: Summary of layered magnetic materials.

Magnetic states	Chalcogenides	Halides
Ferromagnetic	CrXTe_3 ($X = \text{Si, Ge}$) (Cr^{3+})	CrX_3 ($X = \text{Br, I}$) (Cr^{3+})
	Fe_3GeTe_2 (Fe^{2+} and Fe^{3+})	VI_3 (V^{3+})
Antiferromagnetic	MnBi_2Te_4 (Mn^{2+})	CrCl_3 (Cr^{3+})
	MPX_3 ($M = \text{V, Cr, Mn, Fe, Co, Ni}$, and $X = \text{S, Se}$) (M^{2+})	FeX_2 ($X = \text{Cl, Br}$) (Fe^{2+}) NiX_2 ($X = \text{Br, I}$) (Ni^{2+})

These transition metal cations are arranged in honeycomb lattice structure in most of layered magnetic materials except few of them such as transition metal dihalides exhibit triangular lattice structure [25]. In each layer of these magnetic materials included in Table 1, the transition metal cations are bonded to non-magnetic anions in octahedral coordination. These layers are stacked on top of each other and separated by a finite vdW gap to form the bulk

crystal. Different types of layer stacking such as monoclinic and rhombohedral can occur in these materials depending on the selection of transition metal cations and non-magnetic anions. The interlayer bonding between the adjacent layers is weak, allowing for the exfoliation of bulk crystal to obtain atomically thin flakes. Thus, these layered magnetic materials offer a good platform to study magnetism from bulk to 2D limit.

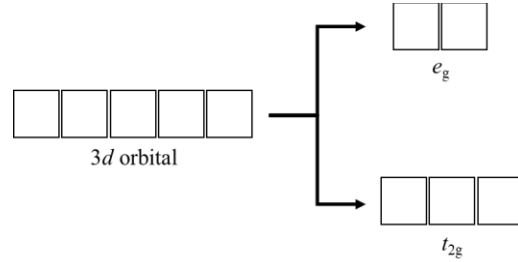
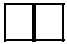

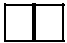
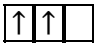
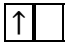
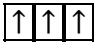
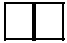
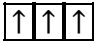
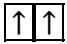
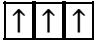
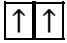
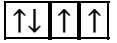
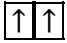
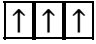
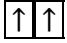
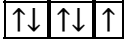
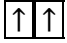



Figure 1.1: Splitting of five 3d orbitals of transition metal cations into three t_{2g} and two e_g levels under octahedral crystal field.

Magnetism in vdW magnetic materials arise from the magnetic moment due to the spin and orbital momenta of the 3d electrons of the transition metal cations. So, the magnetic properties in layered materials are strongly dependent on the transition metal cations. In presence of crystal field from the octahedral coordination of the transition metal cations in layered magnetic materials mentioned in Table 1, the five 3d orbitals splits into three low-energy t_{2g} orbitals (d_{xy} , d_{xz} , and d_{yz}) and two high-energy e_g orbitals ($d_{x^2-y^2}$ and d_z^2) due to octahedral crystal fields [27] as shown in Figure 1.1. Then, the d electrons of the transition metal cations fill these orbitals according to Hund's rule, as summarized in Table 2 for various transition metal cations. The occupancy of these orbitals determines the total magnetic moment of the 3d transition metal cations. Under the octahedral crystal field, if t_{2g} levels are partially filled, the total orbital angular momentum (L) is non-zero. Here, the orbital angular momentum for higher energy e_g orbitals ($d_{x^2-y^2}$ and d_z^2) is always zero. Whereas the octahedral crystal field (along z -direction) will affect d_{xz} , and d_{yz} orbitals belonging to low-energy t_{2g} levels. In this case when $L \neq 0$ due to partial

Table 2: Orbital occupancy for $3d$ valence electrons of various transition metal cations under octahedral crystal field.

Transition metal ions	$3d$ orbital occupancy
$V^{2+} (3d^3)$	e_g  t_{2g} 
$V^{3+} (3d^2)$	e_g  t_{2g} 
$Cr^{2+} (3d^4)$	e_g  t_{2g} 
$Cr^{3+} (3d^3)$	e_g  t_{2g} 
$Mn^{2+} (3d^5)$	e_g  t_{2g} 
$Fe^{2+} (3d^6)$	e_g  t_{2g} 
$Fe^{3+} (3d^5)$	e_g  t_{2g} 
$Co^{2+} (3d^7)$	e_g  t_{2g} 
$Ni^{2+} (3d^8)$	e_g  t_{2g} 

filling of t_{2g} orbitals, the total magnetic moment becomes equal to $g_J[j(j+1)]^{1/2}\mu_B$, where $|j|$, g_J , and μ_B are the total angular momentum quantum number, Landé g -factor, and, Bohr magneton, respectively. Now, when orbital angular momentum is quenched (i.e., $L = 0$) which happens for either half-filled or fully filled t_{2g} orbitals, only the spin magnetic moment contributes the total

magnetic moment. This leads a magnetic moment per transition metal atom to be $2[s(s+1)]^{1/2}\mu_B$, where s and μ_B are the total spin quantum number.

The magnetism in these materials can be explained within the framework of isotropic Heisenberg Hamiltonian: $H = -2 \sum J S_i S_j$, where J is the exchange coupling constant the summation is over all pairs of magnetic ions in the lattice and the spins are treated as three-component vectors. Here, the magnetic exchange J is considered to be isotropic as depict in Figure 1.2(a). In the case of layered magnetic materials, the magnetic interactions are usually anisotropic. Generally, the magnetic exchanges within the plane are much stronger than the inter-plane exchanges in vdW magnetic materials. So, the magnetism is described by Heisenberg Hamiltonian with anisotropic exchange: $H = -2(J_x S_i S_j + J_y S_i S_j + J_z S_i S_j)$, where J_x , J_y , and J_z are exchange coupling constants along three different directions and they are unequal as seen in Figure 1.2(b).

The combination of crystal field from the octahedral coordination and SOC of the transition metal cations introduce anisotropy to the system. Now, with an additional anisotropy term the full Hamiltonian becomes: $H = -2 \sum (J S_i S_j + \lambda S_i^z S_j^z) - \sum A (S_i^z)^2$, where J , λ , and A are isotropic exchange, anisotropic exchange and single-ion anisotropy parameters, respectively. The single-ions anisotropy (A) defines the magnetic anisotropy of the system [Figure 1.2(c)].

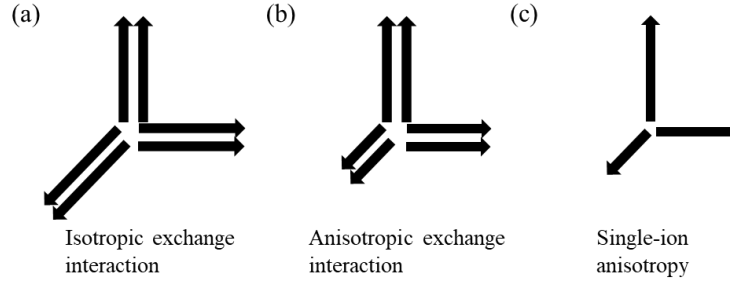


Figure 1.2: Schematic of (a) isotropic exchange interaction, (b) anisotropic exchange interaction, and (c) single-ion anisotropy. In (a) and (b), the length of arrows represents strength of exchange interaction. Double arrows in (a) and (b) indicate interaction between two moments.

The long-range magnetic ordering in layered magnetic materials is mainly governed by intralayer exchange interaction because the interlayer interactions are usually weak in layered materials. Most of the layered magnetic materials summarized in Table 1 are insulating in which the transition metal ions carry localized magnetic moments. The magnetic exchanges among those localized moments are mediated through direct and superexchange interactions. However, the direct exchange between two cations is usually weak for most of these materials due to large cation-cation distances. Therefore, the superexchange interactions between magnetic cations which are mediated through non-magnetic anions are the dominant magnetic coupling. Together with the nearest-neighbor superexchange, the second and third nearest-neighbor superexchanges stabilize the magnetic interactions in layered magnetic materials. The nature and strength of these superexchange interactions are mainly dependent on the cation-anion bond length, cation-anion-cation bond angle, and the orbital overlap between magnetic cation and nonmagnetic anion. (Figure 1.3). In addition, for metallic layered magnets such as Fe_3GeTe_2 , and MnBi_2Te_4 the magnetic interactions are also mediated by itinerant electrons.

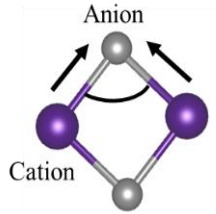


Figure 1.3: Schematic of superexchange interaction between two cations through anion.

1.1.2 Types of magnetism

The interplay between different exchange interactions and magnetic anisotropy arising from crystal field and SOC can give rise to a rich variety of magnetic states (Table 1) though they possess similar crystal structures. Broadly, layered magnetic materials exhibit two types of magnetism: (1) ferromagnetism and (2) antiferromagnetism.

In ferromagnetic state, both intralayer and interlayer exchange interactions favor parallel spin alignment [Figure 1.4(a)]. As seen in Table 1, ferromagnetism exists in both transition metal chalcogenides and halides material families, most of which feature out-of-plane magnetic moments such as CrX_3 ($X = \text{Br}, \text{I}$), VI_3 , Fe_3GeTe_2 , etc. On the other hand, antiferromagnetic (AFM) layered materials possess various magnetic ordering, which can be divided into two types: (1) A-type and (2) C- and G-type [Figures 1.4(b and c)]. In an A-type AFM state, the magnetic moments within the layer have ferromagnetic alignment but exhibit interlayer AFM ordering, such as MnBi_2Te_4 , FeX_2 ($X = \text{Cl}, \text{Br}$), and CrCl_3 . Whereas the C- and G-type antiferromagnets show intralayer AFM correlations and can be further divided into AFM-zigzag (such FePS_3 , NiPS_3 , etc), AFM-stripy, and AFM-Néel (such as MnPS_3), as shown in Figure 1.4(c).

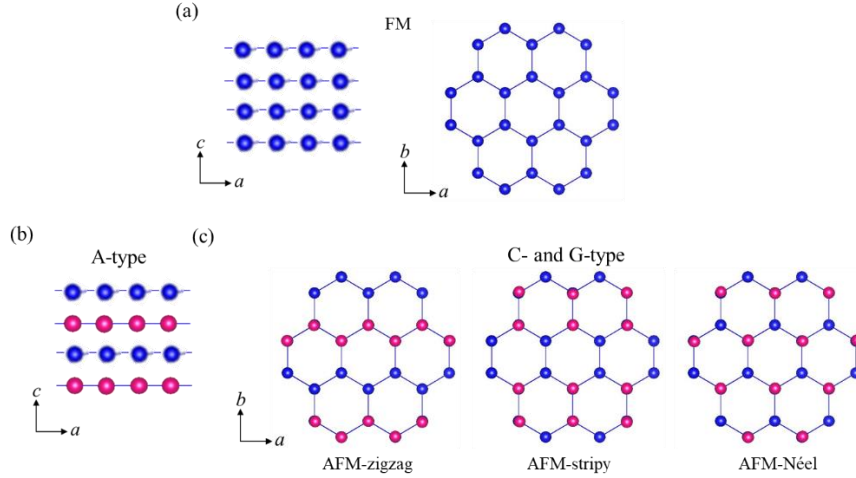


Figure 1.4: Magnetic order for layered magnetic materials. (a) Ferromagnetic (FM) order. Left and right figures show interlayer and intralayer FM order, respectively. (b) A-type antiferromagnetic (AFM) order. (c) C- and G-type AFM order. From left to right: intralayer AFM-zigzag, AFM-stripy, and AFM-Néel order. AFM-zigzag and AFM-stripy belong to C-type whereas AFM-Néel belongs to G-type categories. Blue and pink color represent spin up and spin down, respectively.

1.2 Antiferromagnetic van der Waals (vdW) metal thiophosphates MPX_3 (M = Transition metal and X = Chalcogen)

Recent developments in 2D magnetism have intensified the study of vdW magnetic materials. Among various 2D magnetic materials, one model system is metal thiophosphates. This material family was discovered in the late 1800s by Friedel and Ferrand [28,29]. It is usually represented by a chemical formula MPX_3 or $M_2P_2X_6$, where M stands for transition metals, P is phosphorus, and X denotes for chalcogens. Since its discovery, this material family has been studied in various fields including magnetism, ferroelectricity, optoelectronics, photo-electrochemical reactions, hydrogen storage, and Li-ion batteries [28,29]. Most MPX_3 ($M = V, Cr, Mn, Fe, Co, \text{ and } Ni$) compounds are antiferromagnetic, whereas some MPX_3 ($M = Cd, Zn, Sn, \text{ and } Hg$) compounds exhibit diamagnetism because of fully filled d orbitals. Due to layered structures, these materials have also been established as potential 2D magnets. In addition, the

band gaps ranging from 1.3 to 3.5 eV make MPX_3 materials suitable for device applications at relatively higher temperatures with higher voltage and current ranges [28,29]. Such a wide band gap also enhances their light absorption efficiency. Furthermore, their unusual intercalation-reduction behavior and higher ionic conductivity facilitate potential applications in Li-ion batteries. Because of such versatility, MPX_3 materials have gained intensive attention in recent years.

MPX_3 materials crystallize in monoclinic ($C2/m$ space group), rhombohedral ($R\bar{3}$ space group) or triclinic ($P\bar{1}$ space group) layered structure as summarized in Table 3. Despite three different crystal structures, all MPX_3 materials exhibit common structural feature with $(P_2X_6)^{4-}$ ($X = S$ or Se) anion sublattice within each layer [Figure 1.5]. The metal atoms M are arranged in a honeycomb lattice which is situated around the $(P_2X_6)^{4-}$ bipyramids as shown in Figure 1.5(b). Thus, these compounds can also be represented as $M_2P_2X_6$. As seen in Figure 1.5(c), a finite vdW gap (shortest distance between the X layers) about 3.22-3.24 Å is present in MPX_3 . Various metal ions with different ionic radii can be incorporated into MPX_3 resulting in the alteration of the slab size. The flat pyramid consisting of X^{2-} ions remain invariable within $(P_2X_6)^{4-}$ structural modification, but the P-P distance is slightly adjusted to accommodate the changing metal cations. For example, the P-P length is changed from 2.148 Å in $NiPS_3$ to 2.222 Å in $CdPS_3$ [28]. Such an increase in P-P distance is also accompanied by the elongation of the layer thickness. This demonstrates the structural flexibility of MPX_3 compounds that leads to the abundant material choices by varying M and X atoms.

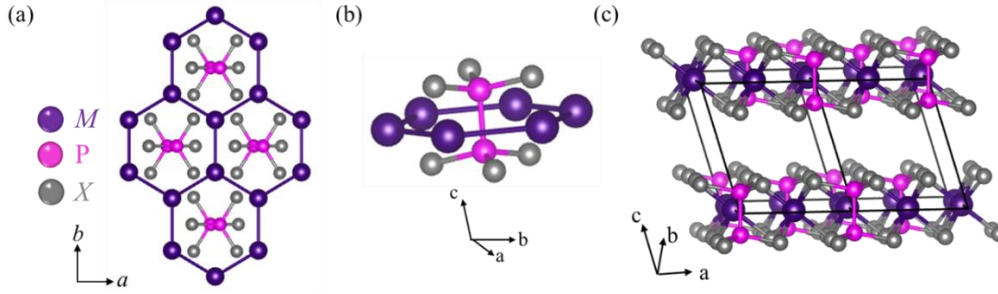


Figure 1.5: Crystal structures of MPX_3 . (a) MPX_3 materials exhibit common structural features with $(P_2X_6)^{4-}$ ($X = S$ or Se) anion sublattice within each layer. (b) Metal M arranged in a honeycomb lattice around the $(P_2X_6)^{4-}$ bipyramids. (c) Layered structure with finite van der Waals gap between the layers.

Table 3: Information about crystal structure and magnetism for MPX_3 materials [28,29].

Materials	Crystal structure	Space group	Magnetic ordering	Ordering temperature (K)
VPS ₃	Monoclinic	$C2/m$	AFM	61
MnPS ₃	Monoclinic	$C2/m$	AFM	78
FePS ₃	Monoclinic	$C2/m$	AFM	118
CoPS ₃	Monoclinic	$C2/m$	AFM	122
NiPS ₃	Monoclinic	$C2/m$	AFM	155
ZnPS ₃	Monoclinic	$C2/m$	Non-magnetic	-
CdPS ₃	Monoclinic	$C2/m$	Non-magnetic	-
MgPS ₃	Monoclinic	$C2/m$	Non-magnetic	-
PdPS ₃	Monoclinic	$C2/m$	Non-magnetic	-
SnPS ₃	Monoclinic	$C2/m$	Non-magnetic	-
HgPS ₃	Triclinic	$P\bar{1}$	Non-magnetic	-
CrPSe ₃	Monoclinic	$C2/m$	AFM	126
MnPSe ₃	Rhombohedral	$R\bar{3}$	AFM	74
FePSe ₃	Rhombohedral	$R\bar{3}$	AFM	112
NiPSe ₃	Monoclinic	$C2/m$	AFM	205
ZnPSe ₃	Rhombohedral	$R\bar{3}$	Non-magnetic	-
CdPSe ₃	Rhombohedral	$R\bar{3}$	Non-magnetic	-
MgPSe ₃	Rhombohedral	$R\bar{3}$	Non-magnetic	-
HgPSe ₃	Monoclinic	$C2/m$	Non-magnetic	-

Although the individual lamella is similar for all MPX_3 compounds, their symmetry and layer stacking in bulk may vary depending on the M and X as summarized in Table 3. In particular, the symmetries and crystal structures for sulfides and selenides of MPX_3 materials are distinct. Generally, the sulfides MPS_3 exhibit monoclinic crystal structure with $C2/m$ symmetry, except triclinic structure with $P\bar{1}$ symmetry for $HgPS_3$. On the other hand, for selenides $MPSe_3$ with larger P-Se bond lengths and Se-P-Se bond angles as compared to their sulfides counterparts, these materials mostly crystallize in rhombohedral structure with $R\bar{3}$ symmetry. The only exceptions are $NiPSe_3$, $CrPSe_3$, and $HgPSe_3$ which exhibit monoclinic crystal structure.

The crystal lattice and symmetries are important in determining magnetic properties. Coupling of crystal lattice and symmetries with magnetism has been theoretically predicted in MPX_3 [30]. Variation of lattice parameters have been found to modify the magnetic properties. In fact, magnetic interactions are strongly dependent on the lattice parameters. As mentioned earlier, the crystal lattice and symmetry modify with the substitutions of M and X atoms in MPX_3 . Therefore, the magnetic properties in MPX_3 compounds vary with the choices of M and X atoms. For example, the Néel temperature (T_N) changes with transition metal M , increasing from 78 K for $MnPS_3$, to 118, 122, and 155 K for $FePS_3$, $CoPS_3$, and $NiPS_3$, respectively [31–36]. Similarly, the T_N also varies upon substituting Se for S. For example, $MnPSe_3$, $FePSe_3$, and $NiPSe_3$ have different T_N (74 K, 112 K and 205 K, respectively) as compared to their sulfide counterparts [37,38]. The T_N for different MPX_3 compounds has been provided in Table 3. In addition, magnetic structure also changes with the substitutions of M and X atoms. For instance, $MnPS_3$, $FePS_3$, and $NiPS_3$ exhibit different magnetic structures as shown in Figure 1.6. Likewise, the magnetic structure can also be modified with S and Se substitution as seen for $MnPS_3$ and $MnPSe_3$ (Figure 1.6).

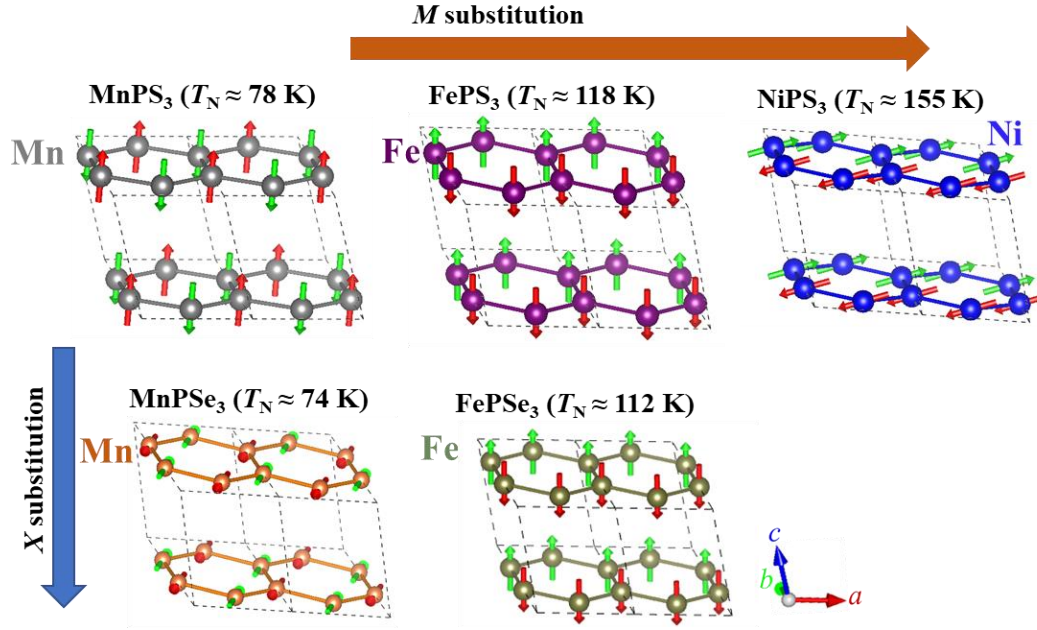


Figure 1.6: Known magnetic structures of various MPX_3 materials. Magnetic structure for NiPSe_3 have not been experimentally determined.

Furthermore, the magnetism has also been found to be related to a structural distortion in MPX_3 compounds [39–41]. As illustrated in Figure 1.7, every metal atom M in MPX_3 is located at the center of an octahedron formed by six X atoms. Such MX_6 octahedra, however, possesses a trigonal distortion that is characterized by the angle θ between the trigonal axis (perpendicular to the ab -plane) and the M - S bond (Figure 1.7). Therefore, magnetism in MPX_3 can be described by an isotropic Heisenberg Hamiltonian with additional single-ion anisotropy due to the combined effect of crystal field and spin-orbit splitting: $H = -2 \sum J S_i S_j + A S_{iz}^2$, where J and A are the magnetic exchange and single-ion anisotropy parameters, respectively [39]. The relative strengths of J and A determine the magnetic properties in MPX_3 [39,41].

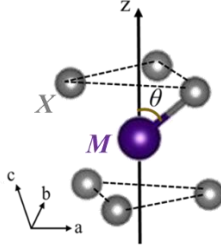


Figure 1.7: Trigonal distortion in MPX_3 materials; z -axis is the trigonal axis.

In MPX_3 , the magnetic exchanges J between magnetic moments are mainly mediated by superexchange couplings through X atoms with additional direct exchange for interactions between nearest neighbors [39,40]. The superexchange couplings will contribute both the nearest-neighbor interaction (J_1) and the interactions between further neighbors. The nature of superexchange interaction depends on the M - X - M bond angle [Figure 1.3] and the d -electron occupancy of the M atoms [39]. According to Goodenough-Kanamori rules [42,43], the superexchange interaction is ferromagnetic (FM) if M - X - M bond angle is close to 90° and AFM when M - X - M bond angle is 180° . In addition, the superexchange process is also determined by the occupancy of d orbital. For example, $NiPS_3$ and $CoPS_3$ have different magnitudes for superexchange because of distinct occupancy of d orbitals for Ni^{2+} and Co^{2+} ions although they have the same magnetic structure [41]. On the other hand, the direct exchange depends on the distance between the nearest neighbors. Increasing the distance between nearest neighbors will weaken the direct exchange between them. The direct exchange usually influences the nearest neighbor interaction J_1 . The direct exchange is AFM and FM in $MnPS_3$ and $FePS_3$, respectively [40]. Whereas the direct exchange does not exist in $NiPS_3$ because of the filled t_{2g} orbitals for Ni^{2+} [40]. All the magnetic interactions are superexchange in nature in $NiPS_3$.

The combination of spin-orbit coupling (SOC) and trigonal distortion of MX_6 octahedra leads to the single-ion anisotropy (A) in an otherwise isotropic system. The effect of A is to introduce anisotropy in the system. The relative values of J and A determine the moment orientation in MPX_3 . In the case when $J \gg A$ (for very small A), the magnetism is isotropic and can be explained by the 3D isotropic Heisenberg Hamiltonian. For higher values of A , the magnetism becomes anisotropic and corresponds to XY or Ising-type magnetism depending on the sign and magnitudes of A . In Mn and Ni systems, the orbital angular momentum (L) is quenched for Mn^{2+} (d^5) and Ni^{2+} (d^8) because of their half and fully filled t_{2g} orbitals respectively leading to the negligible SOC for the magnetic atoms [39]. In $MnPS_3$, the effect of spin-orbit splitting and trigonal distortion is found to be negligible for the high spin ground state of Mn^{2+} [39], so the magnetism of the less distorted $MnPS_3$ is governed by the dipolar anisotropy that leads to out-of-plane moment direction with small tilt towards a -axis [33,44,45], as shown in Figure 1.6. On the other hand, $NiPS_3$ exhibits greater trigonal distortion as compared to $MnPS_3$. In $NiPS_3$ and $MnPS_3$, θ has been found to be 51.05° and 51.67° , respectively [41]. Compared with $\theta \approx 54.75^\circ$ for the undistorted octahedra, the greater trigonal distortion in $NiPS_3$ leads to much stronger single-ion anisotropy (0.3 meV) than that of $MnPS_3$ (0.0086 meV), as revealed by inelastic scattering measurements [33,40,41]. This causes the Ni moments to be aligned within the basal plane perpendicular to the trigonal axis (Figure 1.6) [34,39,45], which is likely explained by the anisotropic Heisenberg Hamiltonian with XY -type anisotropy. The situation is different for $FePS_3$ in which the SOC is much stronger for Fe^{2+} (d^6). So, the contribution of the SOC and trigonal distortion is much greater in $FePS_3$, which gives rise to highly anisotropic magnetic ordering as characterized by higher single-ion anisotropy $A \approx 2.66$ meV for $FePS_3$ [46]. Thus, $FePS_3$ is best described by the Ising Hamiltonian corresponding to the

highly anisotropic Ising-type magnetic ordering with magnetic moments aligned along the out-of-plane direction [39,46]. In this way, the combination of J and A parameters determine the magnetic properties in MPX_3 . The experimental values of J and A parameters obtained by neutron scattering experiments for various MPX_3 materials are summarized in Table 4.

Table 4: Magnetic exchange and anisotropy parameters for MPX_3 materials. Here, negative and positive signs denote AFM and FM interactions, respectively.

Parameters	MnPS ₃ [33]	FePS ₃ [46]	CoPS ₃ [41]	NiPS ₃ [40]
S	5/2	2	3/2	1
T_N (K)	78	118	120	155
J_1 (meV)	-1.54	2.96	2.04	3.8
J_2 (meV)	-0.14	-0.08	0.26	-0.1
J_3 (meV)	-0.36	-1.92	-4.21	-13.8
A (meV)	0.0086	2.66	2.06	0.3

Due to their layered structures, MPX_3 materials can be easily exfoliated down to atomically thin layers. The feasibility of obtaining thin flakes allows for the study of magnetic properties in the 2D limit. However, the study of magnetism in atomically thin MPX_3 has been limited because of difficulty in probing AFM ordering in 2D. Recently, the magnetic properties of only a few atomically thin MPX_3 materials such as MnPS₃, FePS₃, NiPS₃, and MnPSe₃ have been studied. Using techniques such as Raman spectroscopy [47–49], second harmonic generation [50], and magnetotransport [10] measurements, the persistence of AFM ordering have been demonstrated in atomically thin MPX_3 crystals.

Although the long-range magnetic ordering has been found to exist in thin layers of MPX_3 , only FePS₃ [48] and MnPSe₃ [50] exhibit magnetic ordering down to monolayer. The persistence of magnetism in monolayer FePS₃ [48] and MnPSe₃ [50] have been ascribed to their highly anisotropic Ising-type and XY-type antiferromagnetism, respectively. The ordering

temperature T_N of 118 K for FePS₃ remains independent of the thickness from bulk to the monolayer limit [48]. Whereas the T_N decreases from 74 K in bulk to 40 K in single layer of MnPSe₃ [50]. In NiPS₃ [49] and MnPS₃ [47], magnetism is found to be stable up to bilayer with slightly reduced T_N , but does not persist in the monolayer limit. Because of their highly insulating nature, the magnetotransport measurement is challenging to probe the magnetic properties in MPX_3 . So far, the tunneling transport measurement has been only been successful to reveal magnetic ordering in atomically thin crystals of MnPS₃ [10]. Through tunneling magnetoresistance, the signatures of spin-flop transition seen in the bulk MnPS₃ have been demonstrated in thin layers. This provides a new experimental route that can be applied to study 2D magnetism in other MPX_3 materials.

1.3 Tuning magnetism in MPX_3

Tuning magnetism in layered magnetic materials provides deep understanding of the low-dimensional magnetism as well as broaden their scope for potential applications in next-generation devices. Various strategies such as doping [37,51–80], application of pressure [81–84] and electrostatic gating [13,15] have been adopted to tune the magnetic properties of layered magnets. These techniques have been successful in controlling the spin orientation in vdW magnetic materials, which leads to novel magnetic phenomenon arising from 2D magnetism.

Engineering magnetic properties is one of the major research directions in MPX_3 family, and extensive efforts have already been put to tune their magnetism. Varying lattice parameters and magnetic moments through elemental substitution is an effective way to modify magnetism. Substituting metal atoms have been adopted as an important method to manipulate the magnetic properties in MPX_3 . The metal atoms are arranged in a honeycomb lattice in MPX_3 as shown in Figure 1.5. The structural similarity of the MPX_3 materials facilitates the realization of

polymetallic “mixed” compounds with substitution of M atoms. Here, two different metal atoms are mixed in a honeycomb lattice to create a substituted compound (Figure 1.8). Since the magnetic properties are strongly dependent on M atoms, the magnetic exchange (J) and anisotropy (A) are found to be modulated with metal substitutions which lead to tunable magnetic properties.

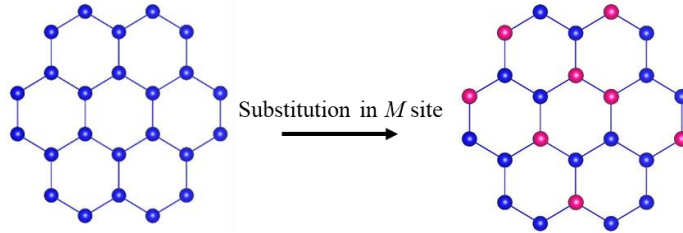


Figure 1.8: Conceptual schematic of metal substitution in MPX_3 .

Tunable magnetism arising from competing magnetic interactions, magnetic anisotropies, and spin fluctuations have been observed in metal-substituted MPX_3 compounds such as $Ni_{1-x}Mn_xPS_3$, $Mn_xFe_{1-x}PS_3$, $Fe_{1-x}Ni_xPS_3$, $Mn_{1-x}Zn_xPS_3$, $Ni_{1-x}Co_xPS_3$ and $Mn_{1-x}Fe_xPSe_3$ [51–66]. For example, Zn substitution for Mn can systematically tune magnetic order and spin orientations in $MnPS_3$ [51–53]. In Mn-substituted $FePS_3$, spin glass is found to arise from the competing $3d$ magnetism [54–56]. In addition, substitutions of M in $NiPS_3$ and $MnPS_3$ have also been found to effectively modify their magnetic anisotropies [37,39,50,52]. Varying the Ni:Mn ratio in $Ni_{1-x}Mn_xPS_3$ can re-orientate the magnetic easy axes from nearly the ab -plane to the out-of-plane direction [62,64]. In $NiPS_3$, Fe substitution can trigger a crossover from XY to Ising anisotropy [63,66]. Moreover, the magnetic anisotropy can be reduced with magnetic dilution by substituting non-magnetic Zn in $MnPS_3$ [53,60]. Such tuning of magnetic properties through metal substitutions provides deeper understanding of low dimensional magnetism as well as promising material platform to investigate 2D magnetism. Therefore, the metal substitution in

MPX_3 is still an active research direction, and new works are expected to focus on materials other than $MnPS_3$, $FePS_3$, and $NiPS_3$ as well as extend beyond traditional isovalent metal substitution.

In addition to metal substitution, the layered structure of MPX_3 materials allows for another doping strategy i.e., the inter-layer interaction of guest atoms as depicted in Figure 1.9. Although various AFM spin configurations can be obtained through metal substitutions, but these works reported so far [51–66] are unable to achieve novel magnetic phases. So, new doping techniques are necessary to stabilize novel magnetic states in MPX_3 . Doping charge carriers has been predicted to drive AFM to ferromagnetic (FM) transition in MPX_3 [30,85]. Inter-layer intercalation might lead to charge carrier doping, and thus it could provide a promising route to achieve novel magnetic phases in MPX_3 that are not accessible through metal substitutions.

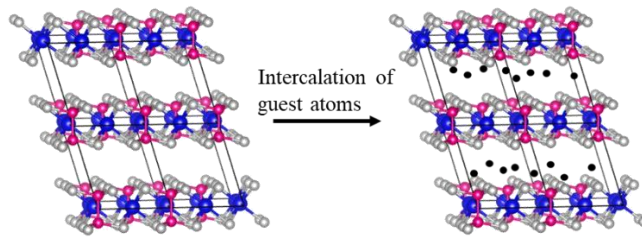


Figure 1.9: Conceptual schematic of inter-layer intercalation in MPX_3 .

Among various MPX_3 materials, inter-layer intercalation studies have been mainly focused on $NiPS_3$ [86–89], which may be due to its high reactivity towards intercalation as compared to other MPX_3 materials [89]. The magnetic susceptibility has been reduced in Li-intercalated $NiPS_3$, while no noticeable changes observed in $FePS_3$, $FePSe_3$ and $MnPSe_3$ [89]. In addition, various organic-ion intercalations have been successful to drive AFM-to-ferrimagnetic (FIM) [78,86,88] transitions in $NiPS_3$. These are in stark contrast to metal-substituted $NiPS_3$ [58,62–66] which only feature tunable AFM ground states. The distinct results for inter-

layer intercalation might be attributed to charge carrier doping, whereas substituting M atoms might only alter magnetic exchange and anisotropy. Increased vdw gap may also play some role in mediating magnetism. These results suggest that intercalation can be an effective route to control magnetism in MPX_3 .

Chapter 2: Experimental Methods

This research involves the synthesis and characterizations of various layered magnetic materials. First, we synthesized the single crystals and confirmed their elemental and structural phases. Then, we performed magnetization and thermodynamic measurements to characterize their magnetic properties. The following experimental methods were used in this research:

2.1 Single crystal Growth

The growth of high-quality single crystals is essential for the advancements of experimental condensed matter and material science research. For many years, most of the condensed matter experiments relied on polycrystalline samples because good single crystals are difficult to synthesize. The polycrystals samples are more prone to defects and impurities and thus the good single crystals have become a necessity in condensed matter experiments. An ideal single crystal contains a single grain, so the defects like grain boundaries usually seen in polycrystals can be eliminated. A single crystal has a well-defined crystalline axis and thus the measurements such as magnetic and electronic transport can be conveniently performed along different crystal axes. This will help to determine the anisotropic physical properties of a material. For example, the magnetic properties along different crystal orientation can be known using a good single crystal sample. In addition, single crystals possess well-defined surfaces and edges, which makes them suitable for surface-sensitive measurements such as angle resolved photoemission spectroscopy (ARPES), scanning tunneling microscopy/spectroscopy (STM/S), etc. This work focuses on vdW magnets, and it is important to obtain good single crystals of layered materials. This is because high-quality nanoflakes with less defects can be exfoliated from bulk crystals, providing access to explore 2D physics.

With all these advantages, physicists and material scientists in the field have been working to develop techniques for single crystal growth and understand their mechanism to yield the best-quality single crystals for scientific research. In general, crystal growth occurs in two stages: (1) nucleation and (2) crystal formation. First, a small number of atoms, ions or molecules nucleate to form tiny clusters which is known as nucleation. Such small clusters start bonding with nearby atoms or molecules and increase in size, resulting in growth of larger crystals. There are different techniques to synthesize single crystals such as flux, chemical vapor transport (CVT), Bridgman, Optical floating zone (OFZ), and Czochralski methods. The growth technique is mainly based on volatility, thermodynamic stability, and the size of the crystals. Here, we have used the CVT method to grow high-quality sizeable single crystals of pristine and doped MPX_3 .

2.1.1 Chemical vapor transport (CVT)

The chemical vapor transport (CVT) method is based on vaporization of source, transportation of the vapor along some temperature gradient, and condensation at the cold zone. Both the mixture of starting elements and the polycrystal precursors obtained by solid state reaction can be used as a source. Depending on the desired target compound, I_2 , $TeCl_4$, $SeCl_4$, etc, can be used as transport agent to aid the vapor transportation process. Some layered magnetic compounds such as $MnPS_3$ and CrI_3 which have volatile elements like S and I_2 respectively can be grown without transport agents. The source end where the starting materials are loaded is kept at a higher temperature whereas the sink end is relatively colder to maintain the thermal gradient. When the source end is heated the transport agent reacts with the source to form intermediate gaseous compounds. The thermal gradient will drive the intermediate

compound towards the sink where it will disassociate and nucleate as a target compound. This will happen only if the free energy of formation for the target phase is lower than the

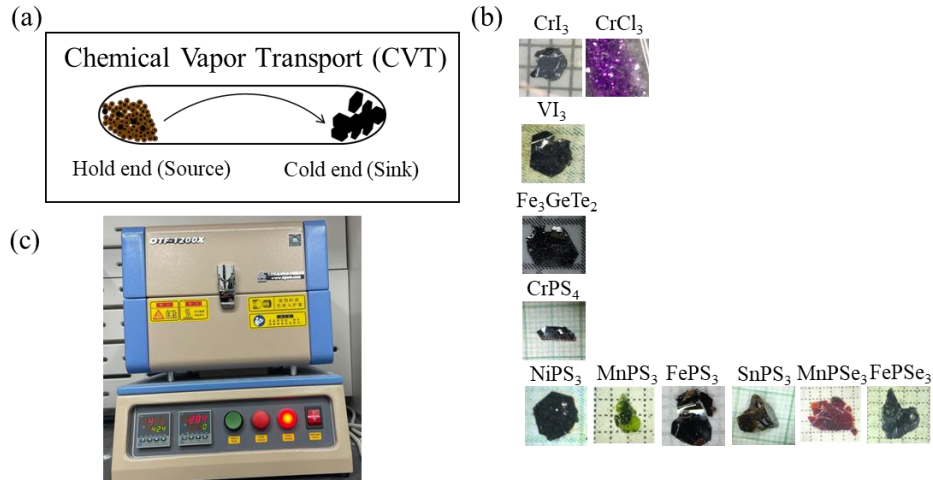


Figure 2.1: (a) Schematic of chemical vapor transport (CVT) growth. (b) Two-zone furnace used to grow single crystals of layered magnetic materials through CVT method. (c) Optical microscope images of various layered magnetic materials synthesized by CVT method.

intermediate gaseous phase at the cold end. After disassociation the transport agent will travel back to the source, form the intermediate phase and again transport to sink. This process repeats several times leading to the formation of single crystal mostly at the cold end as shown in Figure 2.1(a). Since this process mainly depend on the transport of source from hot to cold end, the important factors that determine the successful growth are source and sink temperature, temperature gradient, the type of transport agent, and amount of source. The optical microscope images of single crystals of few vdW magnetic materials are shown in Figure 2.1(b).

For MPX_3 materials, source elementary powders with proper molar ratio or pre-reacted polycrystal precursors along with transport agent I_2 are sealed in an evacuated quartz tube about 15 cm long. Then, it is placed in a two-zone furnace [Figure 2.1(c)] and heated at a suitable temperature for about 1-2 weeks. The growth tube is heated slowly to high temperatures to avoid

excessive pressure due to volatile elements. After growth is completed, the furnace is naturally cooled down to room temperature. The details for growth and the images of the single crystals studied in this dissertation are summarized in experiment sections of each respective chapters.

2.2 Electrochemical intercalation

The electrochemical intercalations are performed in a two-electrode battery system using electrochemical workstation (Battery testing system 8.0, Neware) [Figure 2.2(a)]. Figure 2.2(b) shows the conceptual schematic of electrochemical intercalation process. The setup consists of a two-electrode system immersed in an electrolyte in which the host single crystal and intercalatant are fixed on cathode (working electrode) and anode (counter and reference electrode), respectively. As shown in Figure 2.2(c), a battery is composed of a few other components such as spring, spacer, and separator. The spacer and spring help to maintain pressure and compactness inside the battery. The function of separator is to avoid anode and cathode from touching each other.

In this method, the electrical potential causes electrons to flow from anode to cathode through the circuit within the battery leading to the intercalation of guest ions into vdW gap of the host sample (Fig. 5). The total number of ions intercalated into the host can be controlled by controlling the total amount of charge (i.e., integral current over time) transferred from anode to cathode. The degree of lithiation x (number of atoms intercalated per mole of host) is calculated using, $x = (ItM)/(eN_A m)$, where I , t , M , e , N_A , and m are discharge current, time of intercalation, molar mass of host, electron charge, Avogadro's constant, and mass of the host single crystal, respectively. The detailed electrochemical intercalation process is described in chapter 7.

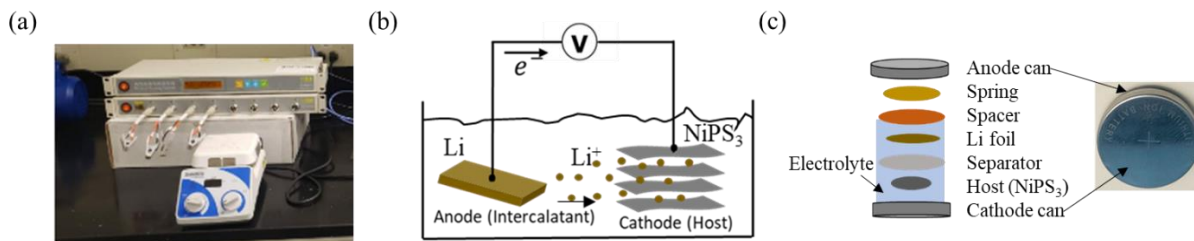


Figure 2.2: (a) Electrochemical workstation used for intercalation. (b) Conceptual schematic of electrochemical intercalation of guest atoms into layered magnetic materials. (c) Homemade battery used for electrochemical intercalation.

2.3 Characterization

After successful crystal growth, the next step is property characterization. First, we determine the elemental and structural phases of the crystals. Then, we characterize their magnetic and thermodynamic properties as described below:

2.3.1 Energy-dispersive X-ray spectroscopy (EDS)

The elemental characterization of a material is important prior to any measurement. The elemental composition of a material is characterized by Energy-dispersive X-ray Spectroscopy (EDS) inside scanning electron microscope (SEM, FEI Nova Nanolab). A high energy electron beam is focused on to the sample surface, resulting in the ejection of electrons from the inner shells of an atom. This creates an electron “hole” in the inner shell and the electrons from the outer shell tend to fill this “hole”, releasing energy in the form of x-ray (Figure 2.3). This x-ray is the characteristics of each element, depending on their unique atomic structure and electronic arrangement. Thus, analyzing the energy and intensity of these characteristics X-ray, EDS provides the elemental composition of any element.

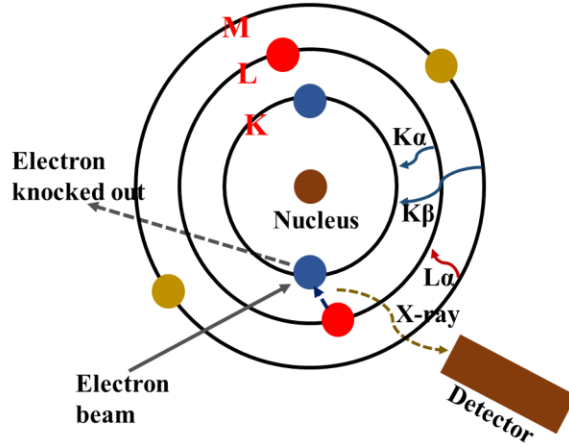


Figure 2.3: Schematic showing principle of Energy dispersive X-ray spectroscopy (EDS).

2.3.2 X-ray diffraction (XRD)

The crystal structure of a single crystal can be determined by x-ray diffraction (XRD). In this work, the single crystal and powder XRD are performed using the in-house Panalytical X'pert Pro MRD and Rigaku XtaLAB Synergy Cu-K α diffractometers, respectively at room temperature. Atoms form a periodic arrangement in a crystal, and this periodic lattice diffract incident x-rays. The adjacent parallel lattice planes with path difference $2d\sin\theta$ undergo constructive interference satisfying Bragg's law (Figure 2.4): $2d\sin\theta = n\lambda$, where n is the diffraction order, λ (wavelength of x-ray) = 1.5406 Å for Cu-K α , d is the inter-planar distance and θ is the diffraction angle.

Different crystals are characterized by different sets of lattice planes. XRD can be used to determine the interplanar distance of the crystal planes from which lattice parameters and atomic position can be resolved, which consequently provides accurate structure phase characterization. In a typical XRD setup, x-ray source is fixed whereas sample holder and detector can be rotated by angle θ and 2θ respectively. At some angle θ , Bragg's law is satisfied, and intensity peaks are

observed in XRD spectrum, which provides the information about the phase and lattice parameter of the crystals.

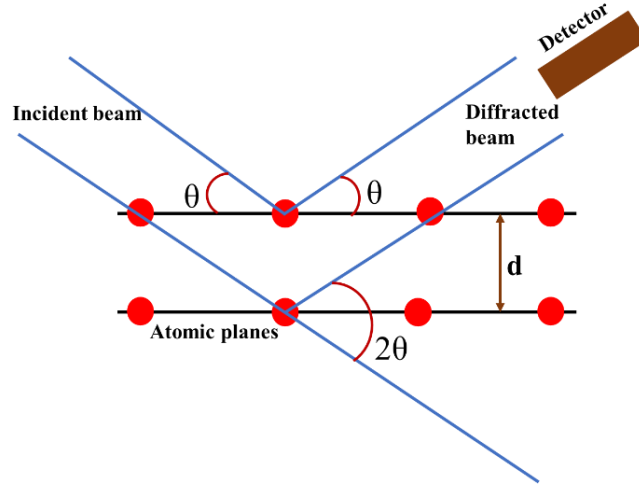


Figure 2.4: Schematic showing principle of X-ray diffraction (XRD).

2.3.3 Magnetization

Magnetization measurements are performed in a physical property measurement system (PPMS, Quantum Design) [Figure 2.5(a)]. PPMS is able to measure both DC and AC magnetizations. In this work, we use DC magnetization to study magnetism. In DC magnetization measurement, the sample is vibrated at a set frequency within the coil set. Due to the vibration of the sample the magnetic flux changes that induces a voltage in a pickup coil [Figure 2.5(b)] based on Faraday's law. This generated voltage is proportional to the magnetization, amplitude, and vibration frequency. The pick-up coil is used to detect the voltage generated from the internal field and motion, which consists of series connection of two counterwound coils just above and below the sample. Finally, the DC magnetic moment with the sensitivity on the order of 10^{-5} - 10^{-6} emu is determined by measuring the coefficient of the sinusoidal voltage response from the detection coil.

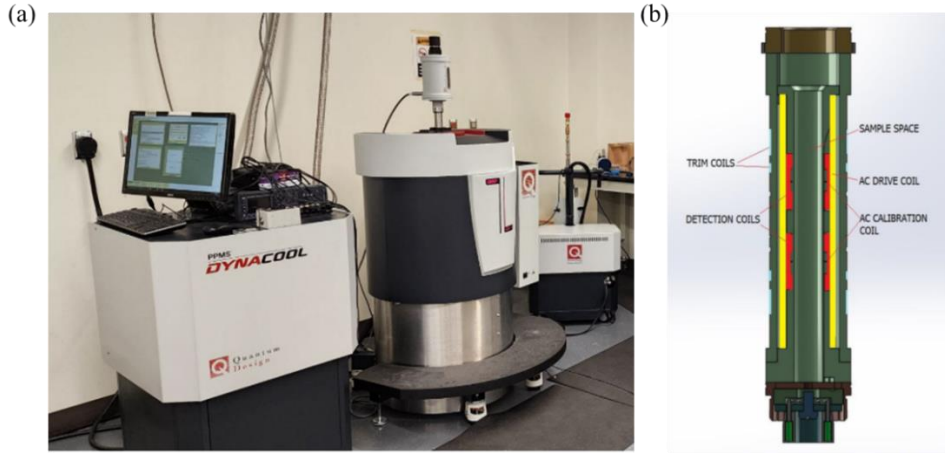


Figure 2.5: (a) Dynacool physical property measurement system (PPMS) from Quantum Design [92]. (b) Coil used for ACMS-II magnetization measurement in PPMS [92].

2.3.4 Heat Capacity

Heat capacity (C) measurements provide information about crystal lattice, electronic, and magnetic properties of a material. We measured heat capacity to understand the magnetic properties of a sample used in this work. Heat capacity measurements are performed in a physical property measurement system (PPMS, Quantum Design). Samples with flat surface are loaded onto a $2 \times 2 \text{ mm}^2$ platform [Figure 2.5]. The flat surface ensures good thermal contact with the platform, which is further enhanced by using Apiezon N and H greases for low and high temperature ranges, respectively. MPX_3 materials studied in this work display magnetic orders well below room temperature, so we performed heat capacity measurements below room temperature and only used Apiezon N grease. Unlike electronic and magnetization measurements which can be performed under normal vacuum conditions, the heat capacity measurement requires a high vacuum to minimize thermal transport through the gas medium. It also involves two steps: (1) the measurement of puck (without sample) to record background heat capacity and (2) the measurement with the sample which gives the actual heat capacity for sample after subtracting the background heat capacity i.e., $C_{\text{sample}} = C_{\text{total}} - C_{\text{background}}$.

The thermodynamic measurement in PPMS is measured by relaxation technique. The principle of this measurement is to add heat to the system and monitor temperature change during sample relaxation. First, heat is supplied at constant power for a short period of time followed by gradual heat loss to the environment through the supporting wires. The temperature change on the platform during this heating and cooling cycle is recorded using following equation:

$$C_{\text{total}} \frac{dT}{dt} = -K_w(T-T_0) + P(t)$$

Here, K_w is the thermal conductance of the wires, T_0 is the PPMS temperature, $P(t)$ is the power of the heat, and C_{total} is the total heat capacity (Sample + background). This equation gives the total heat capacity which will eventually be subtracted with the background heat capacity to give the heat capacity for the sample only.

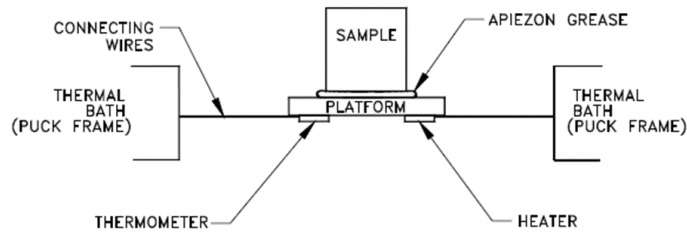


Figure 2.6: Schematic of sample platform for heat capacity measurement in PPMS [92].

Chapter 3: Highly sensitive spin-flop transition in antiferromagnetic van der Waals material MPS_3 ($M = Ni$ and Mn)

Recent developments in two-dimensional (2D) magnetism have motivated the search for novel vdW magnetic materials to explore new magnetic phenomenon in the 2D limit. Metal thiophosphates, MPX_3 , is a class of magnetic vdW materials with AFM ordering persisting down to the atomically thin limit. The magnetism in this material family has been found to be highly dependent on the choice of transition metal M . In this work, we synthesized the intermediate compounds $Ni_{1-x}Mn_xPS_3$ ($0 \leq x \leq 1$) and investigated their magnetic properties. Our study reveals that the variation of Ni and Mn content in $Ni_{1-x}Mn_xPS_3$ can efficiently tune the spin-flop transition, likely due to the modulation of the magnetic anisotropy. Such effective tuning offers a promising candidate to engineer 2D magnetism for future device applications. This chapter is based on our published work in PHYSICAL REVIEW MATERIALS 5, 064413 (2021) (<https://doi.org/10.1103/PhysRevMaterials.5.064413>) [64].

3.1 Introduction

Recent breakthroughs in two-dimensional (2D) magnetic materials open a new route in exploring intrinsic magnetism in the 2D limit. The discoveries of novel 2D magnets [6–11] provide opportunities not only to understand the mechanism of low dimensional magnetism but also to design next-generation devices. For example, advances in devices and heterostructures involving 2D magnets enable the effective tuning of their electronic and magnetic properties, providing a fascinating platform to study fundamental physics [12–23]. These breakthroughs have greatly enriched our understanding of magnetism in the 2D limit.

Among 2D magnetic materials, one model system is metal thiophosphates MPX_3 ($M =$ transition metal ions, $X =$ chalcogen ions). MPX_3 materials crystallize in a monoclinic layered

structure with $C_{2/m}$ space group, in which the transition metal ions form a honeycomb layer and carry localized magnetic moments [28,93–95]. The van der Waals (vdW)-type crystal structure allows for the inter-layer intercalation [89,96–99] and mechanical exfoliations down to atomically thin layers [10,48,49,100–106]. The magnetic and electronic properties of the MPX_3 family are strongly dependent on the choice of the transition metal M . $MnPS_3$, $NiPS_3$, and $FePS_3$ have been found to exhibit Heisenberg-type, XY or XXZ -type, and Ising-type antiferromagnetism, respectively [31–33,39,46,107]. The Neel temperature (T_N) also varies with transition metal M , increasing from 78 K for $MnPS_3$, to 118, 122, and 155 K for $FePS_3$, $CoPS_3$, and $NiPS_3$, respectively [31–36]. Besides magnetism, the electronic properties of MPX_3 are also tunable with M , exhibiting a wide range of band gaps from 1.3 eV for $FePSe_3$ to 3.5 eV for $ZnPS_3$ [28]. Recent studies on $NiPS_3$ and $MnPS_3$ have established these materials as platforms to study correlated electrons in 2D magnetic materials [104,108,109]. Furthermore, theoretical and experimental high-pressure studies revealed insulator-to-metal transitions in $MnPS_3$ [109,110], $MnPSe_3$ [110], $FePS_3$ [111–114], $NiPS_3$ [109,115] and $V_{0.9}PS_3$ [113,116], and even the emergence of superconductivity in $FePSe_3$ [117].

The structural similarity of the MPX_3 materials allows for the synthesis of polymetallic “mixed” compounds with substitution of transition metal M [51–61]. Varying lattice constant and magnetic moments through elemental substitution is an effective way to tune magnetism and probe the underlying physics of magnetic materials. Coupling of magnetism with lattice constants and symmetries in MPX_3 has been theoretically predicted [30]. Tuning of magnetism has also been observed in mixed compounds such as $Mn_xFe_{1-x}PS_3$, $Mn_{1-x}Fe_xPSe_3$, $Fe_{0.5}Ni_{0.5}PS_3$ and $Mn_{1-x}Zn_xPS_3$ [51–61]. For example, magnetic order and spin orientations in $MnPS_3$ can be

systematically tuned by Zn substitution for Mn [51–53]. Spin glass is also found to arise from the competing $3d$ magnetism in Mn substituted FePS_3 [54–56].

In this work, we report the systematic study on previously unexplored $\text{Ni}_{1-x}\text{Mn}_x\text{PS}_3$ ($0 \leq x \leq 1$). We synthesized single crystals and characterized the evolution of magnetic properties with substitutions. In addition to the known field-induced spin-flop (SF) transition in MnPS_3 , we have also discovered the previously unreported SF transitions in NiPS_3 . Furthermore, we found these SF transitions are extremely sensitive to magnetic substitutions, likely due to the re-orientation of the magnetic moments of $3d$ elements controlled by trigonal distortion of MS_6 octahedral. Such tunable magnetism offers a promising platform for studying new phenomenon arising from 2D magnetism and future device applications.

3.2 Experiment

Single crystals of $\text{Ni}_{1-x}\text{Mn}_x\text{PS}_3$ ($0 \leq x \leq 1$) used in this work were synthesized by the chemical vapor transport method using I_2 as the transport agent. Elemental powders with stoichiometric ratio were sealed in a quartz tube and placed in a two-zone furnace with a temperature gradient from 750 to 550 °C for 1 week. Millimeter to centimeter size single crystals with various colors have been obtained, as shown in the insets of Figure 3.1(a). These crystals are thin plate-like and easily exfoliable with hexagonal facets which are consistent with the vdW structure of MPX_3 shown in Figure 3.1(b). The elemental compositions examined by energy-dispersive x-ray spectroscopy (EDS) reveal successful Ni-Mn substitution. We have carefully characterized the compositions of all the $\text{Ni}_{1-x}\text{Mn}_x\text{PS}_3$ single crystals used in this paper. The Mn contents x throughout this paper are measured values. In addition to composition analysis, the x-ray diffraction (XRD) on single crystals also indicates successful substitution. As shown in Figure 3.1(a), the $(00L)$ diffraction peaks exhibit a systematic low-angle shift with increasing x in

$\text{Ni}_{1-x}\text{Mn}_x\text{PS}_3$, which is consistent with the greater ionic radius of Mn^{2+} as compared with Ni^{2+} , respectively.

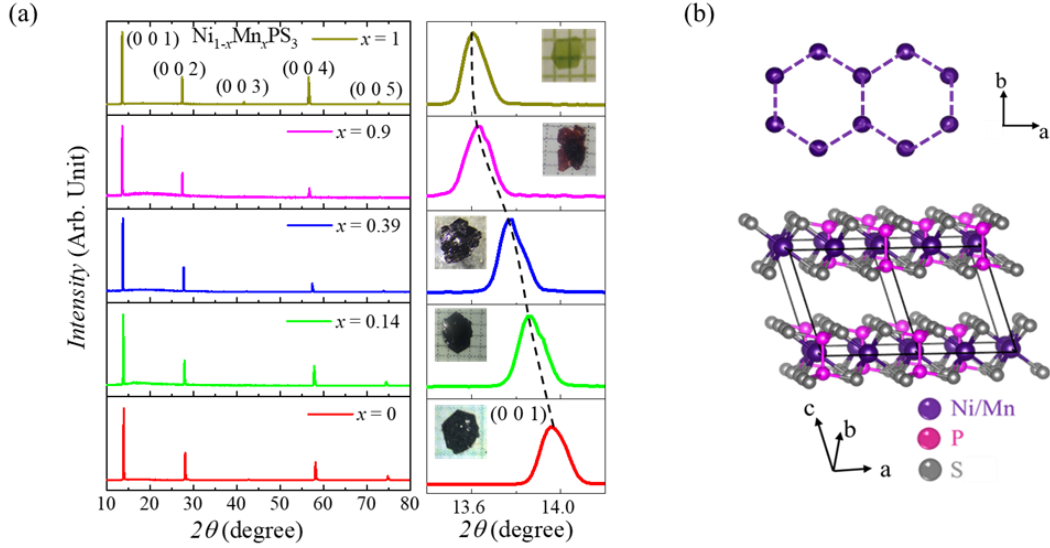


Figure 3.1: (a) Single-crystal x-ray-diffraction pattern for $\text{Ni}_{1-x}\text{Mn}_x\text{PS}_3$ showing the $(00L)$ reflections. Right panels show (001) diffraction peak. Inset: Optical microscope images of the single crystals. (b) Crystal structure of MPS_3 ($M = \text{Ni/Mn}$).

3.3 Results and Discussion

In Figure 3.2 we present the magnetic property characterizations for pristine MnPS_3 and NiPS_3 . For MnPS_3 , below the Néel temperature $T_N \sim 78$ K, a spin-flop (SF) transition can be observed in the isothermal magnetization measured under out-of-plane magnetic field ($H \perp ab$) [Figure 3.2(a)] but is absent under in-plane field ($H // ab$) [Figure 3.2(b)], which is consistent with the previous reports [10,44,60,106,118]. Although the SF transition is largely explored in both bulk and atomically thin MnPS_3 , it has not been *directly* discovered in other members of this family except FePS_3 , in which a metamagnetic transition occurs at very high field ($\mu_0 H > 35$ T) [119]. Here we report the first discovery of SF transition in NiPS_3 . Unlike in MnPS_3 in which the SF transition occurs when $H \perp ab$, the metamagnetic transition in NiPS_3 takes place with in-

plane field, which is characterized by a clear upturn in magnetization above a critical spin-flop field $\mu_0 H_{\text{SF}} \approx 6$ T below the Néel temperature $T_N \approx 155$ K, as shown in Figures 3.2(d) and 3.2(e). The need for relatively high magnetic field could be the reason that prevented the discovery of SF transition in earlier studies [31,120]. On the other hand, the recent magneto-photoluminescence experiment implies a spin re-orientation in bulk NiPS₃ under a much higher in-plane magnetic field of 15 T [104]. Such a high critical field, which is 2.5 times higher than that in our magnetization measurements, might be attributed to the nature of photoluminescence as an indirect probe.

In MnPS₃ and NiPS₃, the SF transition occurring under different field directions is in line with their magnetic structures: The Mn moments in MnPS₃ are aligned along out-of-plane direction [44,53], while the Ni moments in NiPS₃ mostly lie within the plane [31,103,120], as shown in the insets of Figures 3.2(b) and 3.2(c), respectively. In collinear AFM systems, a magnetic field along the easy axis exceeding a critical spin-flop field H_{SF} forces the magnetic moments to rotate [121,122]. In such a SF state, the moments re-orient themselves to a canted configuration perpendicular to the field direction, resulting in a net moment along the easy axis [121,122]. Therefore, the SF transition behaves differently in MnPS₃ and NiPS₃, as illustrated in Figs. 3.2(g) and 3.2(h). Furthermore, because the in-plane projection of Ni moments in NiPS₃ forms a collinear AFM structure along the a -axis [Figure 3.2(c), lower inset], the SF transition is expected to show in-plane anisotropy. To examine this, we measured magnetization with the magnetic field applied along or perpendicular to the hexagonal edges of a NiPS₃ single crystal, as shown in Figure 3.2(e). Indeed, magnetization and SF transition are found to be dependent on in-plane field-orientations.

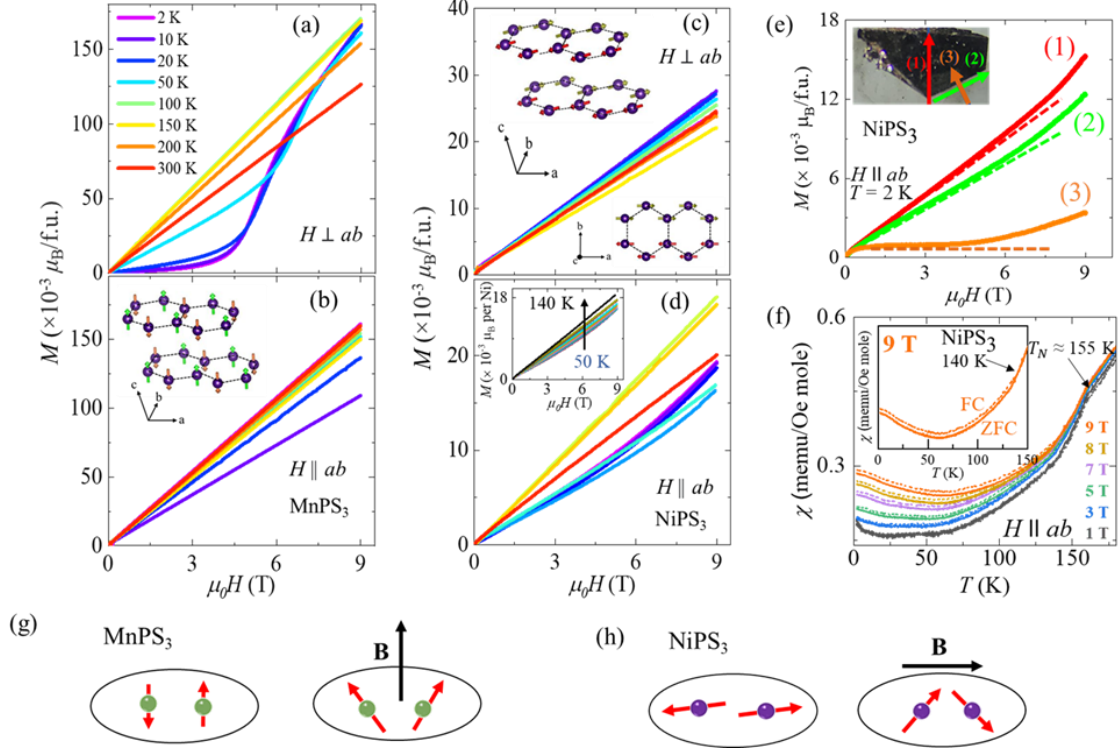


Figure 3.2: Field induced spin flop transitions in pristine MnPS₃ and NiPS₃. (a-b) Isothermal magnetization of MnPS₃ at different temperatures under (a) $H \perp ab$ and (b) $H \parallel ab$. Inset in (b): magnetic structure of MnPS₃. (c-d) Isothermal magnetization of NiPS₃ at different temperatures under (a) $H \perp ab$ and (d) $H \parallel ab$. Upper inset in (c): 3D view of magnetic structure of NiPS₃. Lower inset in (c): Top view of magnetic structure of NiPS₃. Inset in (d): Isothermal magnetization at 50 – 140 K measured with $H \parallel ab$. The same color code is used to indicate temperatures for (a-d). (e) Isothermal magnetization at 2 K under $H \parallel ab$ with different in-plane field orientations. Inset: Optical microscope image of NiPS₃ single crystal with arrows pointing the applied field direction. (f) Temperature dependence of susceptibility of NiPS₃ measure with 1, 3, 5, 7, 8, and 9 T fields, measured with $H \parallel ab$. Inset: Temperature dependence of susceptibility at 9 T under $H \parallel ab$. The solid and dotted lines represent zero-field cooled (ZFC) and field-cooled (FC) data, respectively.

The scenario of SF transition in NiPS₃ is also supported by the temperature dependence of magnetic susceptibility. As shown in Figure 3.2(f), susceptibility measured with in-plane field (χ_{\parallel}) displays a low temperature upturn, which becomes more significant at higher fields ($\mu_0 H > 5$ T). A similar low temperature upturn has been observed in MnPS₃ [60]. In addition, the zero-field cooling (ZFC, solid lines) and field cooling (FC, dashed lines) data display weak but clear

irreversibility above 5 T, which also becomes more visible at higher fields. The development of low temperature upturn and irreversibility can be understood in terms of the ferromagnetic component from the uncompensated canted moments along the easy axis in the SF state, as illustrated in Figure 3.2(h). This irreversibility disappears at 140 K when applying 9 T field, coinciding well with the temperature above which the SF transition vanishes as seen in the isothermal magnetization [Figure 3.2(d), inset]. Such 140 K “disappearing temperature” is lower than the magnetic ordering temperature $T_N \approx 155$ K, which can be attributed to the fact that a greater field is needed for SF transition at higher temperatures, particularly when approaching T_N . H_{SF} enhancement upon increasing temperature is widely seen in other SF systems [10,123–127], which can be interpreted using the molecular field theory [122,127]: In a weakly anisotropic antiferromagnet, spin-flop field H_{SF} can be estimated by $(H_{SF})^2 = 2K/(\chi_{\perp} - \chi_{\parallel})$, where K is the anisotropy constant, χ_{\perp} and χ_{\parallel} are the perpendicular and parallel susceptibilities, respectively [53,122,127,128]. Generally, in AFM systems the difference between χ_{\perp} and χ_{\parallel} reduces more quickly than the magnetic anisotropy constant K upon increasing temperature, leading to enhanced H_{SF} [127].

The distinct SF transitions in NiPS₃ and MnPS₃ due to their different magnetic structures [Figures 3.2(g) and 3.2(h)] motivate us to further study the “mixed” compounds Ni_{1-x}Mn_xPS₃. As shown in Figure 3.3, the magnetism is highly tunable with Ni-Mn substitution. Under both in-plane [$H \parallel ab$, Figure 3.3(a)] and out-of-plane [$H \perp ab$, Figure 3.3(b)] magnetic fields, the magnetization exhibits a systematic enhancement with increasing Mn content x , which is consistent with the much larger magnetization of the pristine MnPS₃ than that of NiPS₃ [Figures 3.2(a-d)] and can be ascribed to greater magnetic moment of Mn²⁺ than Ni²⁺. Interestingly, we found that the SF transitions are extremely sensitive to Ni-Mn substitution. The SF transition in

NiPS₃ under in-plane field disappears with 5% Mn substitution (*i.e.*, $x = 0.05$ in Ni_{1-x}Mn_xPS₃). Similarly, under out-of-plane field, H_{SF} in MnPS₃ is reduced by half with 5% Ni substitution (*i.e.*, $x = 0.95$) and disappears upon 10% substitution ($x = 0.9$).

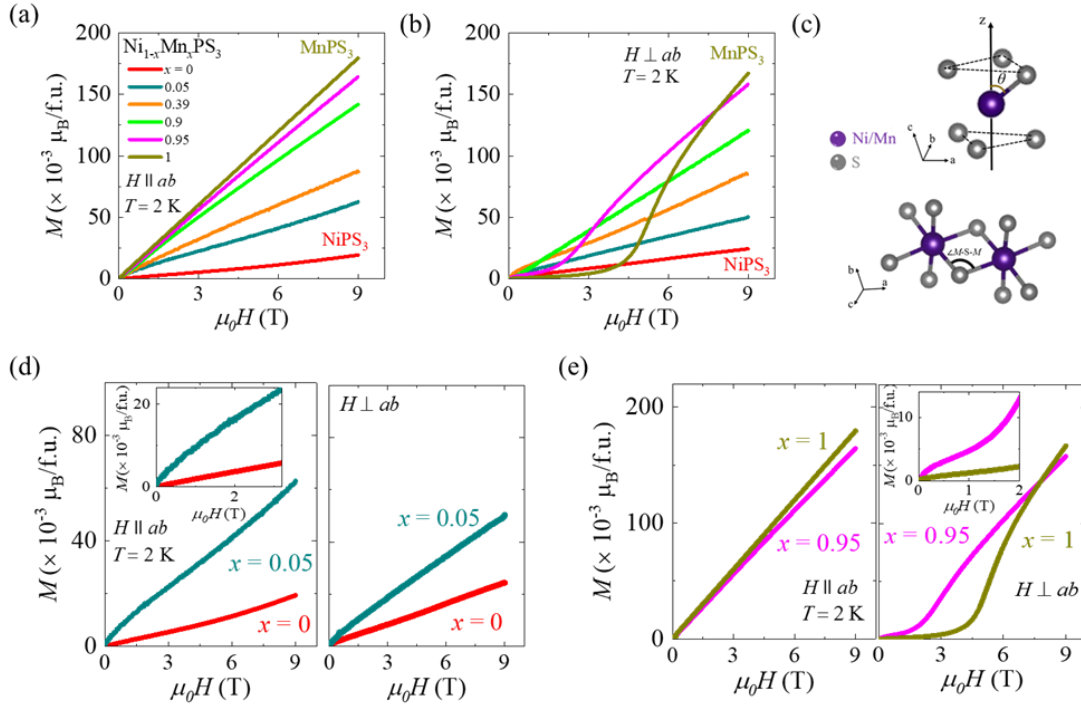


Figure 3.3: (a-b) Isothermal magnetization of Ni_{1-x}Mn_xPS₃ samples ($0 \leq x \leq 1$) at $T = 2$ K under (a) $H \parallel ab$ and (b) $H \perp ab$. The same color code is used to indicate temperatures for (a) and (b). (c) Trigonal distortion in MPS₃ compounds. z -axis is the trigonal axis. (d) Isothermal magnetization of Ni_{1-x}Mn_xPS₃ ($x = 0$ and 0.05) at $T = 2$ K under $H \parallel ab$ (Left panel) and $H \perp ab$ (Right panel). Inset: zoom in of the low-field magnetization. (e) Isothermal magnetization of Ni_{1-x}Mn_xPS₃ ($x = 0.95$ and 1) at $T = 2$ K under $H \parallel ab$ (Left panel) and $H \perp ab$ (Right panel). Inset: zoom in of the low-field magnetization.

Further insights can be gained from the careful comparison between the isothermal magnetizations. In Figure 3.3(d) we show isothermal magnetization $M(H)$ of NiPS₃ (*i.e.*, $x = 0$) and 5% Mn-substituted (*i.e.*, $x = 0.05$) samples, reproduced from Figures 3.3(a) and 3.3(b). With Mn substitution, in addition to the enhancement of magnetization and the absence of SF transition as mentioned above, another interesting behavior is the sublinear field dependence at

low fields. Such nonlinear $M(H)$ is more pronounced under in-plane field [Inset, Figure 3.3(d)], *i.e.*, the magnetic field direction that SF transition occurs for NiPS₃. Similarly, at the MnPS₃ side, 5% Ni-substitution ($x = 0.95$) also introduces remarkable low field nonlinearity in $M(H)$ under out-of-plane field, as shown in the inset of Figure 3.3(e). Such nonlinearity has been verified with multiple samples and careful removal of background signal from the sample holder. The observed low field sublinear $M(H)$ in lightly substituted compounds is in sharp contrast with the linear $M(H)$ in pristine NiPS₃ and MnPS₃, implying the development of ferromagnetic component with substitution. Such behavior has also been observed in Zn-substituted MnPS₃. The previous study [53] on Zn substitution for Mn in MnPS₃ suggests the breakdown of long-range magnetic order due to non-magnetic impurities in local substituted regions, which leads to “weakly bound” Mn moments. The polarization of these Mn moments causes the low-field nonlinear $M(H)$. Another study [52] also propose that for MnPS₃ in which the dipolar anisotropy dominates, the local dipole field is along the out-of-plane direction. As the consequence, when Mn-magnetism is diluted by Zn substitution, the absence of the magnetic moment of one Mn site would affect the closest Mn in the neighboring layers and cause their magnetic moments to be canted, leading to an average staggered magnetic moment in a larger scale [52]. Similarly, the nonlinear $M(H)$ at low fields in our Ni_{1-x}Mn_xPS₃ samples can likely be attributed to the polarization of canted moment originating from substitution. This scenario is further supported by the temperature dependence of susceptibility measurements. As shown in Figure 3.4(a), consistent with the nonlinear $M(H)$ seen under $H||ab$ in the $x = 0.05$ sample [Figure 3.3(d), inset], the in-plane susceptibility ($\chi_{||}$) displays a clear upturn at low temperatures that suggests the development of a ferromagnetic component due to moment canting. Likewise, close to the MnPS₃ side, for $x = 0.95$ sample in which the nonlinear $M(H)$ is significant [Figure 3.3(e), inset],

a susceptibility upturn is also seen, as shown in Figure 3.4(c). The upturn becomes more obvious with increasing the Ni content to 10% ($x = 0.9$), as shown in Figure 3.4(b).

The tunable SF transition and the presence of a ferromagnetic component by Ni-Mn substitution is expected because of the distinct magnetic structures in NiPS₃ and MnPS₃. However, the observed high sensitivity to light substitution is surprising. For example, only 5% Ni substitution can substantially reduce H_{SF} by half in MnPS₃, which is much less than the amount of Zn needed (~20%) to reduce H_{SF} by the same amount [53,60]. The H_{SF} suppression by non-magnetic Zn substitution has been ascribed to the reduction of magnetic anisotropy with magnetic dilution [53]. The Ni-Mn substitution in our Ni_{1-x}Mn_xPS₃, however, induces magnetic impurities. Hence, it is necessary to consider magnetic interaction to understand the observed sensitive doping dependence in Ni_{1-x}Mn_xPS₃. In MPX_3 compounds, magnetism has been found to be related to a structural distortion [23,80–83]. As illustrated in Figure 3.3(c), every metal atom M in MPX_3 is located at the center of an octahedron formed by six X atoms. Such MX_6 octahedra, however, possess a trigonal distortion that is characterized by the angle θ between the trigonal axis (perpendicular to the ab -plane) and the M -S bond. Therefore, magnetism in MPX_3 can be described by an isotropic Heisenberg Hamiltonian with additional single-ion anisotropy due to the combined effect of crystal field and spin-orbit splitting: $H = -2 \sum J S_i S_j + D S_{iz}^2$, where J and D are the exchange and crystal field parameters, respectively [39]. The relative strength of J and D leads to various magnetic structures in MPX_3 , so the trigonal distortion plays critical role in determining the nature of magnetic interactions in MPX_3 [39,41]. In NiPS₃ and MnPS₃, θ has been found to be 51.05° and 51.67°, respectively [41]. Compared with $\theta \approx 54.75^\circ$ for the undistorted octahedra, the greater trigonal distortion in NiPS₃ leads to much stronger single-ion anisotropy (0.3 meV) than that of MnPS₃ (0.0086 meV), as revealed by inelastic scattering

measurements [33,40,41]. This causes the Ni moments to be aligned within the basal plane perpendicular to the trigonal axis, with a small out-of-plane component likely due to weak dipolar anisotropy, as shown in the insets of Figure 3.2(c) [34,39,45]. In contrast, the effect of crystal field and spin-orbit splitting is found to be negligible for the high spin ground state of Mn^{2+} in $MnPS_3$ [39], so the magnetism of the less distorted $MnPS_3$ is governed by the dipolar anisotropy that leads to out-of-plane moment direction with small tilt towards a -axis [33,44,45], as shown in the inset of Fig. 2b. Therefore, the tuning of trigonal distortion by Ni-Mn substitution would significantly affect the magnetic isotropy and further efficiently modify the SF transitions. A similar mechanism has also been proposed for the suppression of H_{SF} in $MnPS_3$ under pressure [45].

In addition to magnetic anisotropy, magnetic exchange interaction may also play an important role. The magnetism in MPX_3 is mainly mediated through superexchange interaction, thereby affected by the $M-X-M$ bonding angle [39,40]. Additionally, the d -electron occupancy of M is important in determining the sign and the nature of the superexchange [39–41]. The $3d$ orbitals of M^{2+} ion consist of high energy e_g and low energy t_{2g} groups, and their occupancies determine the strength of the exchange interactions [41,129]. This has recently been demonstrated by the inelastic neutron scattering measurements which reveals reduced exchange interactions in $CoPS_3$ as compared to $NiPS_3$ due to distinct occupancy of t_{2g} orbital [41]. A similar scenario should also occur in $Ni_{1-x}Mn_xPS_3$, in which the Ni-Mn substitution modifies the magnetic exchange. Indeed, the magnitudes of all the exchanges, except the weakest second nearest-neighbor interaction (J_2), are found to systematically increase with decreasing spin on M^{2+} ion and increasing $M-S-M$ bond angles from $MnPS_3$ to $NiPS_3$ [40,41,129].

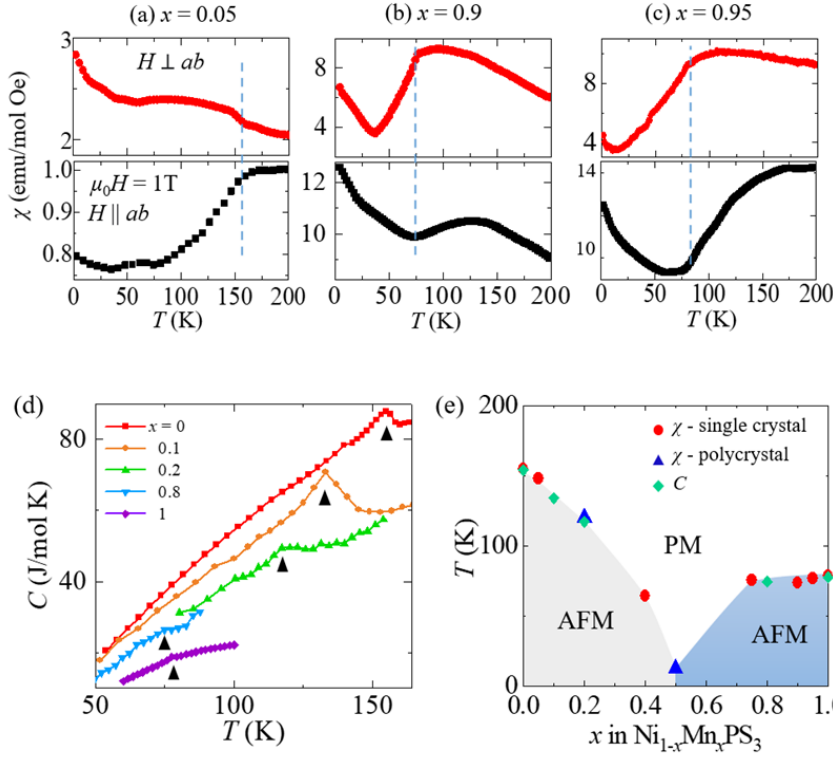


Figure 3.4: (a-c) Temperature dependence of out-of-plane ($H \perp ab$, red, upper panels) and in-plane ($H \parallel ab$, black, lower panels) susceptibilities of (a) $\text{Ni}_{0.95}\text{Mn}_{0.05}\text{PS}_3$, (b) $\text{Ni}_{0.1}\text{Mn}_{0.9}\text{PS}_3$, and (c) $\text{Ni}_{0.05}\text{Mn}_{0.95}\text{PS}_3$ samples. The dashed lines denote T_N . (d) Temperature dependence of heat capacity of $\text{Ni}_{1-x}\text{Mn}_x\text{PS}_3$ samples with $x = 0, 0.1, 0.2, 0.8$ and 1 . The black triangles denote T_N . Data are shifted for clarity. (e) Magnetic phase diagram of $\text{Ni}_{1-x}\text{Mn}_x\text{PS}_3$ ($0 \leq x \leq 1$). The transition temperatures are determined by susceptibility measurements on single- (χ -single crystal) and poly-crystals (χ -polycrystal), and heat capacity (C).

Among the magnetic anisotropy and magnetic exchange interactions, the former may govern the SF transitions in $\text{Ni}_{1-x}\text{Mn}_x\text{PS}_3$. The magnetic ordering temperature is related to the strength of the magnetic interaction. We have extracted T_N for $\text{Ni}_{1-x}\text{Mn}_x\text{PS}_3$ from magnetic susceptibility and heat capacity measurements, as summarized in Figure 3.4(e). For both NiPS_3 and MnPS_3 , T_N decreases with substitution until reaching a minimum value of ~ 12 K in $x = 0.5$ sample. A similar trend has also been observed in other mixed MPX_3 systems such as $\text{Mn}_{1-x}\text{Zn}_x\text{PS}_3$ [60], $\text{Mn}_{1-x}\text{Fe}_x\text{PS}_3$ [56], and $\text{Mn}_{1-x}\text{Fe}_x\text{PSe}_3$ [61]. Several mechanisms [60] [56] [61] have

been proposed for the suppression of T_N , such as the attenuation of the magnetic interaction due to disordered arrangements of the mixed metals ions with dissimilar ionic radius and outer shell electrons, and magnetic frustration among the 3d metal ions in the magnetic sites owing to competition between two different AFM structures. The strong variation of T_N in heavily substituted $\text{Ni}_{1-x}\text{Mn}_x\text{PS}_3$ samples may also share similar scenarios. However, for lightly substituted samples with x close to 0 or 1, T_N only changes slightly as compared to the parent compounds NiPS_3 and MnPS_3 . It is quite interesting to find that the light Ni-Mn substitution only weakly alters the magnetic ordering temperature but drastically suppresses the SF transitions. This suggests that the efficient suppression of the SF transition with light magnetic substitution in $\text{Ni}_{1-x}\text{Mn}_x\text{PS}_3$ can be attributed to the tuning of single ion isotropy rather than exchange interaction.

3.4 Conclusion

In conclusion, we have demonstrated very efficient tuning of the SF transition by light Ni-Mn substitution, which is likely attributed to single ion isotropy tuned by trigonal distortion. Such strong sensitivity suggests that magnetic substitutions can be an effective technique to control magnetism in MPX_3 vdW magnetic materials, leading to a deeper understanding of low dimensional magnetism and providing insight into strategies for future magnetic device development.

Chapter 4: Field-induced ferromagnetism in Cr-substituted antiferromagnetic van der Waals material NiPS₃

Recently, tuning magnetism in layered magnetic materials has intensified for both fundamental research and practical applications. Tunable magnetism has been widely studied in AFM metal thiophosphates MPX_3 compounds. Metal M substitution has become an important strategy to tune their AFM properties. In this work, we performed Cr substitution in NiPS₃ and characterized their magnetic properties. Our study reveals field-induced AFM to ferromagnetic (FM) transition in Cr-substituted NiPS₃, which is likely due to suppression of magnetic anisotropy upon Cr substitution. Such rise of FM state provides a promising material candidate to investigate 2D magnetism for future device applications. This chapter is based on the manuscript under preparation.

4.1 Introduction

Tuning magnetism in two-dimensional (2D) magnetic materials provide deep understanding of the underlying magnetic interactions as well as broaden their scope for potential applications in next-generation devices [6–24,47–50,130]. The magnetic properties in layered magnetic materials have been found to be efficiently tunable with doping [37,51–80]. Introducing guest atoms in van der Waals (vdW) magnets can control the spin orientation which leads to novel magnetic phenomenon arising from 2D magnetism.

Extensive efforts such as substitutions of metal [51–66] and chalcogen [37,72–75], and inter-layer intercalation [78–80] have been put to tune the AFM ground state in MPX_3 (M = transition metal ions, X = chalcogen ions) [51–66,74,75,78–80]. Various AFM spin configurations can be obtained through M and X substitutions. Recently, ferromagnetism has been predicted in metal-substituted MPX_3 [85]. However, metal substitutions in MPX_3 [51–66]

are unable to achieve ferromagnetic (FM) phases. In fact, establishing FM interactions through traditional approach of isovalent metal substitution is challenging in MPX_3 [131]. Doping charge carriers might be an effective route to drive AFM to ferromagnetic (FM) transition in MPX_3 [30,85]. The charge carriers have been doped via inter-layer intercalation [78,80,88], but ferromagnetism still remains elusive. Only transition to ferrimagnetic (FIM) state has been successful in intercalated MPX_3 [78,80,88].

The pursuit of ferromagnetism in MPX_3 is still going on, and recent theoretical works have predicted the topological nontrivial phases in ferromagnetic MPX_3 [90,91]. In addition, stabilizing ferromagnetism in MPX_3 would make them more accessible to study 2D magnetism because FM states are more detectable at the nanometer scale using techniques such as magneto-optical Kerr effect microscopy [6,7], polar reflective magnetic circular dichroism (RMCD) [132] and x-ray magnetic dichroism (XMCD) [133]. These measurement techniques could be challenging to probe AFM ordering because of the absence of net magnetization. So, the rise of FM states in MPX_3 would provide a rare platform for investigating the interplay between magnetism and band topology in 2D.

Substituting metals such as Mn [62,64], Fe [63,66], Mg [134] and Cd [135] in $NiPS_3$ have resulted in tunable AFM properties, but ferromagnetism is still lacking. In this work, we have performed light Cr doping in $NiPS_3$. Our work reveals field-induced transition to FM phase upon inclusion of small amount of Cr, which has never been observed before in $NiPS_3$. Such ferromagnetism is likely due to lowering of magnetic anisotropy due to Cr substitution that enables the magnetic field to easily polarize the moments. Our study provides a novel platform to study 2D magnetism in MPX_3 and develop magnetic materials-based nanodevices.

4.2 Experiment

The $\text{Ni}_{1-x}\text{Cr}_x\text{PS}_3$ ($0 \leq x \leq 0.09$) single crystals used in this work were synthesized by a chemical vapor transport method using I_2 as the transport agent. Elemental powders with desired ratios were sealed in a quartz tube and heated in a two-zone furnace with a temperature gradient from 750 to 550 °C for a week. The elemental compositions and crystal structures of the obtained crystals were examined by energy-dispersive x-ray spectroscopy (EDS) and x-ray diffraction (XRD), respectively. Magnetization measurements were performed in a physical property measurement system (PPMS, Quantum Design).

4.3 Results and discussion

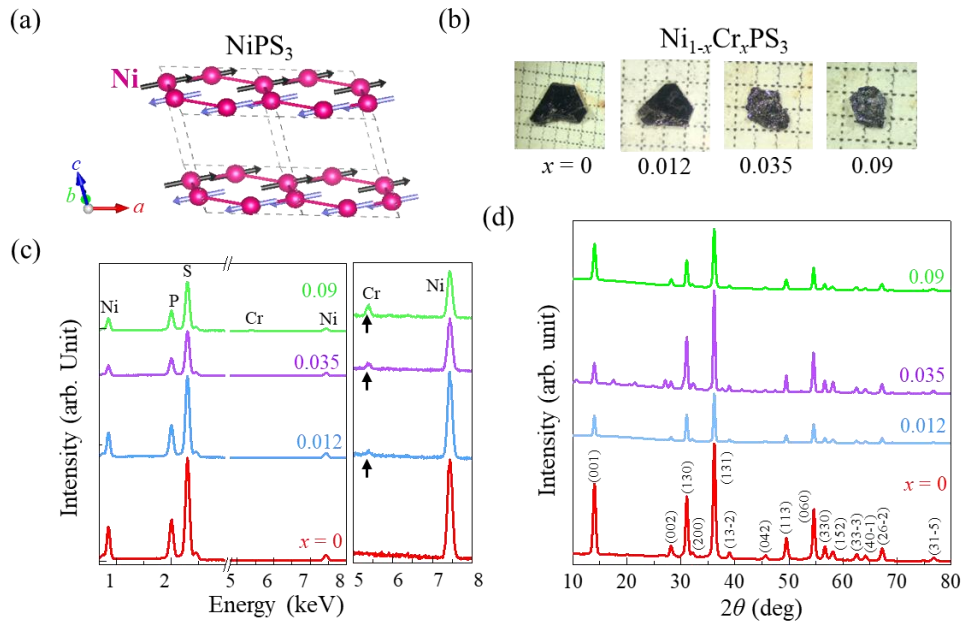


Figure 4.1: (a) Magnetic structure of NiPS_3 . (b) Optical microscope images of $\text{Ni}_{1-x}\text{Cr}_x\text{PS}_3$ single crystals. (c) Energy dispersive x-ray spectroscopy (EDS) spectra for $\text{Ni}_{1-x}\text{Cr}_x\text{PS}_3$ samples. (d) Powder x-ray-diffraction pattern for $\text{Ni}_{1-x}\text{Cr}_x\text{PS}_3$ samples.

NiPS₃ exhibits zig-zag AFM structure with magnetic moments lying mostly along the *ab*-plane as shown in Figure 1(a) [31]. Within the *ab*-plane, the Ni²⁺ moments form a bi-collinear AFM order consisting of ferromagnetic (FM) chains along the *a*-axis [66]. The AFM interactions among these chains have been found to be robust in NiPS₃. A high in-plane magnetic field of $B > 6$ T is required to trigger the metamagnetic spin-flop (SF) transition that leads to canted configuration of two AFM sublattices [64]. Further increasing the magnetic field up to $B = 14$ T is insufficient to fully polarize the moments [136], suggesting the strong AFM interaction in NiPS₃. The spin orientation in NiPS₃ can be modified through metal substitution [62–64,66], but the magnetic ordering still remains AFM. So far only the evidence of ferrimagnetism due to inter-layer intercalation has been observed in NiPS₃ [78–80]. This implies that the novel magnetic states are not easily accessible in NiPS₃.

The situation is different in layered Cr-based AFM materials such as CuCrP₂S₆ [137,138], CrPS₄ [139], CrCl₃ [140], and CrSBr [141], which exhibit AFM to FM transition conveniently under magnetic field. In these materials, the oxidation state of Cr is +3 with $3d^3$ electronic configuration. In this case, the lower t_{2g} level is half filled that leads to a quenched orbital moment for Cr³⁺ ion [142]. So, the spin-orbit (SOC) which is a key source of magnetocrystalline anisotropy is weak for Cr³⁺ ion resulting in a smaller single ion anisotropy. Such a smaller magnetic anisotropy has been attributed to FM polarization of the moments at relatively lower field in Cr-based AFM materials [140]. Given such behavior has been frequently observed in Cr-based antiferromagnets, incorporating Cr in *MPX*₃ lattice may facilitate similar AFM to FM transition. However, the study of Cr-based *MPX*₃ materials is still rare. Only CrPSe₃ [143], CuCrP₂S₆ [137,138], and AgCrP₂S₆ [144,145] have been experimentally realized, but no report for CrPS₃ yet. As mentioned above, Cr ion exhibits +3 valence state in most of the

Cr-based antiferromagnets, while metal ions in MPX_3 have M^{+2} state. This suggests that stabilizing Cr ions in MPX_3 could be challenging. So, a new method of replacing M^{+2} by $(M^{+1})_{0.5}(M^{+3})_{0.5}$ has been adopted to accommodate Cr^{+3} with M^{+1} ($M = Cu$ or Ag) ion in MPX_3 , which resulted in quaternary compounds such as $CuCrP_2S_6$ [137,138] and $AgCrP_2S_6$ [144,145].

The Cr substitution in MPX_3 is indeed difficult as compared to other metal ion substitutions. Like other metal-substituted $NiPS_3$ [62–64,66,134,135], we performed direct Cr substitution in $NiPS_3$ using CVT technique. Complete substitutions of Mn [62,64] and Fe [63,66] in $NiPS_3$ have been successful through CVT. However, using similar growth methods we were only able to introduce about 10% Cr in $NiPS_3$ despite of Cr amount in the source. As shown in Figure 1(b), we obtained good Cr-substituted $NiPS_3$ ($Ni_{1-x}Cr_xPS_3$) single crystals with compositions $x = 0, 0.012, 0.035$ and 0.09 . The successful Cr substitution has been confirmed by composition analysis using EDS. Given such a low amount of Cr, we have been careful in elemental analysis. The final compositions were determined after confirming homogeneous elemental phase in multiple locations of the crystals. As shown in EDS spectra for $x = 0$ to 0.09 in Figure 1(c), with increasing Cr content the relative intensity for Cr element enhances at the expense of Ni intensity [Black arrow in Right panel of Figure 1(c)], indicating successful Cr substitution in $NiPS_3$.

When metal ions are substituted in MPX_3 , the crystal structure remains same [51–66] but the lattice parameters change if two metal ions are of different size. Here, the crystal lattice for $NiPS_3$ remains intact up to 9% Cr doping as demonstrated by the similar XRD spectra without peak shift for $x = 0-0.09$ samples [Figure 1(d)]. The unchanged crystal lattice is reasonable in case of such light doping, considering the fact that $NiPSe_3$ and $CrPSe_3$ have identical crystal

structure and similar lattice parameters [143]. Furthermore, the XRD spectra reveals no impurity peaks, suggesting the lack of impurity phases like CrPS₄, Cr₂S₃, etc. in Cr-doped samples.

On slight increment of Cr from 9% to 11%, we found large vacancy ($\approx 25\%$) on metal sites resulting in final composition of Ni_{0.64}Cr_{0.11}PS₃. Similar metal vacancy is observed in V-based MPX₃ such as V_{0.78}PS₃ [146] and V_{0.9}PS₃ [116], which has been ascribed to the presence of mixed valence states V²⁺ and V³⁺ on the V sites. This implies that Cr ion in the compositions without vacancy i.e., up to $x = 0.09$ must have +2 valence state. In fact, +2 valence for Cr (i.e., Cr²⁺) has been confirmed in CrPSe₃ [143]. Nevertheless, mixed valence states i.e., Cr²⁺ and Cr³⁺ could also exist in Ni_{0.64}Cr_{0.11}PS₃ given the fact that +3 valence for Cr is commonly seen in many layered magnets [137–141]. Such a large vacancy due to mixed valence could be the reason for unsuccessful Cr substitution higher than 11%. Substituting more Cr into the system might enhance the metal vacancy, which could destabilize the crystal lattice.

Since the presence of vacancies on metal sites will affect the magnetic correlation within the metal plane, we mainly focused on magnetic properties of Cr-substituted samples without vacancy i.e., up to $x = 0.09$. To investigate the effects of Cr substitution on magnetic properties, we measured the field dependence of magnetization $M(B)$ for Ni_{1-x}Cr_xPS₃ ($x = 0-0.09$) samples under the in-plane [$B//ab$, Figure 2(a)] and out of plane [$B\perp ab$, Figure 2(b)] magnetic fields at $T = 2$ K. As shown in Figures 2(a and b), the magnetism is found to be highly tunable with Ni-Cr substitution. Under both $B//ab$ and $B\perp ab$ magnetic fields, the magnetization exhibits a systematic enhancement with increasing Cr content x , which is consistent with the greater magnetic moment for high spin state of Cr²⁺ ($S = 2$) than Ni²⁺ ($S = 1$) [143]. No saturation of magnetization has been observed in pristine NiPS₃ ($x = 0$) up to $B = 9$ T field, consistent with a previous report [64]. Similar lack of saturation is also seen in isothermal magnetization $M(B)$ of samples up to $x =$

0.035 [Figures 2(a and b)]. On further increment of Cr amount to 9% ($x = 0.09$), we found the field-induced saturation of magnetization above a saturation field $B_{\text{sat}} \approx 8$ T along both in-plane and out-of-plane directions at $T = 2$ K [Black arrows in Figures 2(a and b)]. Such magnetization behavior can be attributed to ferromagnetic polarization of moments along the field direction. Furthermore, the B_{sat} is found to be suppressed with increasing temperature, and finally the saturation behavior vanishes when $T > 30$ K [Figures 2(c and d)]. The disappearance of magnetization saturation above $T = 30$ K is consistent with the AFM to paramagnetic (PM) transition above ordering temperature $T_N \approx 32$ K as seen in the temperature dependent susceptibility (χ) for $x = 0.09$ [Figure 2(e), Black triangle] and more precisely defined as the peak position in $d\chi/dT$ [Inset, Figure 2(e)]. The reduction of B_{sat} can be ascribed to additional thermal energy upon heating, which will facilitate the saturation of moments.

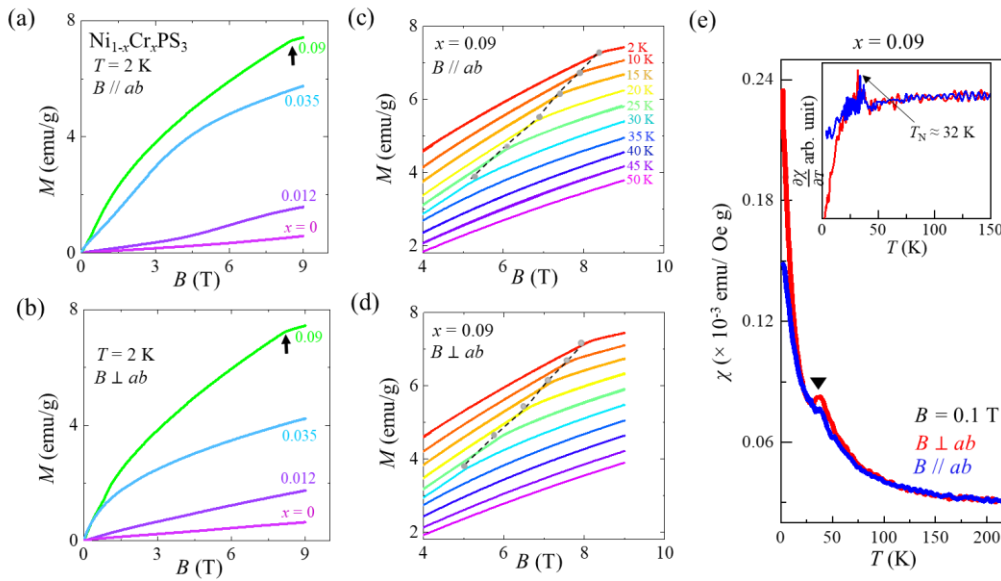


Figure 4.2: (a-b) Isothermal magnetization of $\text{Ni}_{1-x}\text{Cr}_x\text{PS}_3$ at $T = 2$ K under (a) $B \parallel ab$ and (b) $B \perp ab$. (c-d) Isothermal magnetization of $x = 0.09$ sample at different temperatures under (c) $B \parallel ab$ and (d) $B \perp ab$. The dashed lines denote B_{sat} . (e) Temperature dependence of susceptibility (χ) at $B = 0.1$ T under $B \parallel ab$ (Blue) and $B \perp ab$ (Red). The black triangles denote T_N . Inset: Temperature dependence of derivative $d\chi/dT$.

As seen in Cr-based AFM materials with low magnetic anisotropy [137–141], the moments polarize under magnetic field high enough to overcome the magnetic anisotropic energy. The saturation of magnetization in $x = 0.09$ Cr-substituted sample at $B_{\text{sat}} \approx 8$ T, which is not seen in NiPS_3 ($x = 0$), implies weaker magnetic anisotropy as compared to pristine NiPS_3 . The tuning of magnetic anisotropy in MPX_3 can be understood by the evolution of SF transition [45,53,64,74]. As seen in Figure 3(a), a metamagnetic transition takes place in pristine NiPS_3 ($x = 0$) with an in-plane field, which is characterized by a clear upturn (shown by blue arrows) in isothermal magnetizations $M(B)$ at $T = 2$ K. Such metamagnetic transition under an in-plane field in NiPS_3 has recently been attributed to SF transition [64], which is consistent with the nearly in-plane alignment for Ni moments [31]. The SF transition in NiPS_3 has been significantly modified upon Cr substitution. With increasing Cr content x , the SF transition is strongly suppressed, as manifested by the less-obvious magnetization upturn and reduced SF field (B_{SF}). In addition, the SF transition is observed only for $B \parallel ab$ field (Blue arrow) in $x = 0$ -0.035 samples while it appears under both in-plane (Blue arrow) and out of plane (Red arrow) magnetizations in $x = 0.09$ sample.

The B_{SF} suppression is observed in MnPS_3 when Mn is substituted by Zn [53] and Ni [64]. In MnPS_3 , 20% Zn substitution is needed to reduce B_{SF} by half whereas only 5% Ni substitution is sufficient to decrease B_{SF} by the same amount [53]. The reduction of B_{SF} by non-magnetic Zn substitution has been ascribed to the weakening of magnetic anisotropy with magnetic dilution [53]. Similarly, the modification of magnetic anisotropy is also attributed to decreasing B_{SF} in Ni-substituted MnPS_3 [64]. Such tunable SF transition in MnPS_3 can be understood in terms of its weakly anisotropic magnetism with negligible single-ion anisotropy (0.0086 meV) [147]. Now, with much stronger single-ion anisotropy (0.3 meV) for NiPS_3 [40],

the moment reorientation must be more difficult than MnPS_3 . This can be explained by higher B_{SF} for NiPS_3 as compared to MnPS_3 [64]. In fact, the B_{SF} in MPS_3 increases with enhancing magnetic anisotropy in the order $\text{MnPS}_3 < \text{NiPS}_3 < \text{FePS}_3$ [44,64,119]. Therefore, tuning SF transition in NiPS_3 could be more difficult than MnPS_3 . Surprisingly, the SF transition in NiPS_3 is found to be highly sensitive to light Cr substitution. The B_{SF} exhibits monotonic decline with the addition of Cr in NiPS_3 [Figure 3(b)]. For $B \parallel ab$ field, the B_{SF} is substantially reduced from $B_{\text{SF}} \approx 8.2$ T (for $x = 0$) to $B_{\text{SF}} \approx 0.6$ T (for $x = 0.09$) at $T = 2$ K. The appearance of SF transition at $B_{\text{SF}} \approx 0.6$ T for $x = 0.09$ is consistent with low-field metamagnetic SF transition (below $B < 1$ T) widely seen in weakly anisotropic layered Cr-based AFM materials [137–141]. Such suppression of B_{SF} in Cr-substituted NiPS_3 indicates reduced magnetic anisotropy. This is suggestive of more controllable moment orientation in NiPS_3 upon Cr substitution, which will favor the moments to rotate and eventually flip towards field direction as seen in $x = 0.09$ sample.

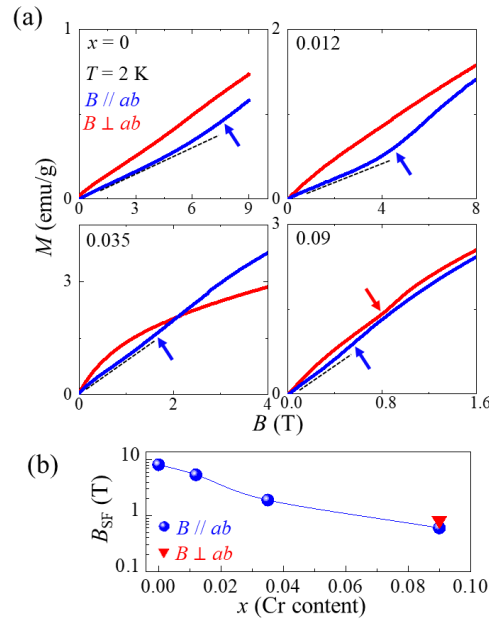


Figure 4.3: (a) Isothermal magnetization of $\text{Ni}_{1-x}\text{Cr}_x\text{PS}_3$ at $T = 2$ K under $B \parallel ab$ (Blue) and $B \perp ab$ (Red) reproduced from Figure 4.2 (a and b). The blue and red arrows show spin-flop field (B_{SF}) under $B \parallel ab$ and $B \perp ab$, respectively. The dashed lines guide to eye. (b) Doping dependence of B_{SF} .

In MPX_3 , the moment orientation is related to the strength of single-ion anisotropy. For example, the negligible single-ion anisotropy in $MnPS_3$ [147] leads to the out of plane moment direction with small tilt towards a -axis [44,45,147]. Whereas with relatively higher single-ion anisotropy in $NiPS_3$ [40], the magnetic moments are confined within the ab -plane [31]. Similarly, with lowering magnetic anisotropy upon Cr substitution in $NiPS_3$, we can expect rotation of moments from the in-plane towards out of plane direction. The moment reorientation with Cr substitution is illustrated in the schematic depicted in Figure 4. As Cr content x is increased, the magnetic moments start to rotate away from the basal plane. Though moments reorientation occurs for $x = 0.012$ and 0.035 samples, they still lie closer to the ab -plane because these samples exhibit SF transition only for $B \parallel ab$ field [Figure 3(a)]. Further increasing the Cr

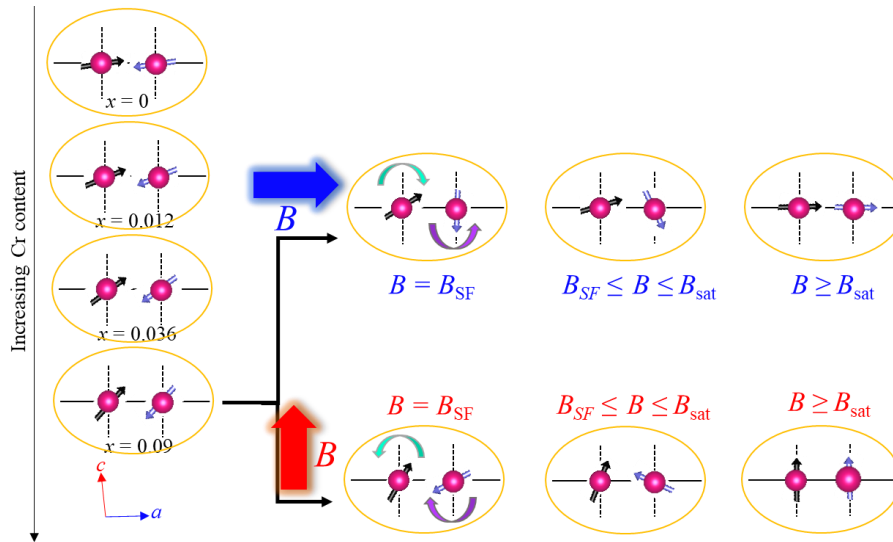


Figure 4.4: Conceptual schematic of moment reorientation in $NiPS_3$ with Cr substitution up to $x = 0.09$ in $Ni_{1-x}Cr_xPS_3$. For $x = 0.09$ sample, the evolution of moment orientation under in-plane and out of plane magnetic fields are demonstrated.

content will enhance the moment canting towards the out of plane direction. This can be seen in $x = 0.09$ sample for which weak but clear metamagnetic transitions appear under both in-plane (Blue arrow) and out of plane (Red arrow) fields [Figure 3(a)]. The SF transition for both $B \parallel ab$

and $B_{\perp ab}$ fields is different than that of Cr-based AFM materials [137–141], where the SF transition is observed only for magnetic field component parallel to their easy axis. Such distinct SF behavior can be attributed to canted configuration for magnetic moments. As seen in Figure 3(a), the B_{SF} along in-plane direction is slightly lower than that of out of plane direction. This suggests that the moments for $x = 0.09$ sample are canted slightly more towards the in-plane than out of plane direction. With such canted AFM ordering in $x = 0.09$, both $B_{\parallel ab}$ and $B_{\perp ab}$ fields can induce moment reorientation to SF phase at $B = B_{SF}$ as shown in Figure 4. Further increasing the magnetic field ($B_{SF} \leq B \leq B_{sat}$) will gradually rotate the canted moments and eventually flip them towards the field direction when $B \geq B_{sat}$.

4.4 Conclusion

In conclusion, we have studied the magnetic properties of previously unreported Cr-substituted NiPS₃. We found that Cr substitution leads to AFM to FM transition in NiPS₃, which is likely attributed to reduction of magnetic anisotropy. Our work provides a novel material choice in MPX_3 family to study 2D magnetism and design nanodevices based on magnetic materials for spintronics applications.

Chapter 5: Controlling magnetic exchange and anisotropy by nonmagnetic ligand substitution in layered MPX_3 ($M = \text{Ni}, \text{Mn}; X = \text{S}, \text{Se}$)

Recent discoveries in two-dimensional (2D) magnetism have intensified the investigation of van der Waals (vdW) magnetic materials and further improved our ability to tune their magnetic properties. Tunable magnetism has been widely studied in antiferromagnetic metal thiophosphates MPX_3 . Substitution of metal ions M has been adopted as an important technique to engineer the magnetism in MPX_3 . In this work, we have studied the previously unexplored chalcogen X substitutions in MPX_3 ($M = \text{Mn}/\text{Ni}; X = \text{S}/\text{Se}$). We synthesized the single crystals of $\text{MnPS}_{3-x}\text{Se}_x$ ($0 \leq x \leq 3$) and $\text{NiPS}_{3-x}\text{Se}_x$ ($0 \leq x \leq 1.3$) and investigated the systematic evolution of the magnetism with varying x . Our study reveals the effective tuning of magnetic interactions and anisotropies in both MnPS_3 and NiPS_3 upon Se substitution. Such efficient engineering of magnetism provides a suitable platform to understand low-dimensional magnetism and develop future magnetic devices. This chapter is based on our published work in *PHYSICAL REVIEW RESEARCH* 4, 023256 (2022) (<https://doi.org/10.1103/PhysRevResearch.4.023256>) [74].

5.1 Introduction

The recently discovered two-dimensional (2D) magnetic materials have attracted intensive attention because of the possible new phenomena arising from 2D magnetism and the promising potential for spintronic applications [6–11]. The integration of 2D magnets in nanodevices and heterostructures has further fueled the investigation of their magnetic and electronic properties, thus offering a fertile platform to design next-generation devices [12–24]. Such developments in 2D magnetism have motivated the search for novel magnetic van der Waals (vdW) materials to explore the low-dimensional magnetism in real materials.

One interesting class of magnetic vdW materials is AFM MPX_3 (M = transition metal ions, X = chalcogen ions), in which the transition metal ions carry localized magnetic moments in a layered honeycomb lattice [28,93–95]. Their magnetic properties are strongly influenced by the transition metal M . The magnetic exchange and anisotropy are found to vary with the choice of M [28,31–36,39,44,46,60,62,64,106,107,118,119,148]. Such tuning of magnetism by altering M has led to the study of a series of polymetallic “mixed” MPX_3 compounds such as $Ni_{1-x}Mn_xPS_3$, $Mn_xFe_{1-x}PS_3$, $Fe_{1-x}Ni_xPS_3$, $Mn_{1-x}Zn_xPS_3$, $Ni_{1-x}Co_xPS_3$ and $Mn_{1-x}Fe_xPSe_3$ [51–66]. Tunable magnetism arising from the interplay between competing magnetic interactions, magnetic anisotropy, and spin fluctuations has been observed in these mixed compounds [51–65], providing promising candidates to explore novel phenomena originating from 2D magnetism.

Compared with the metal substitution in the M site [51–66], chalcogen substitution in the X site leaves the magnetic ions intact, hence offering a relatively clean approach to modify the magnetic exchange interactions. The effectiveness of substituting non-magnetic ligand atoms to engineer the magnetism in vdW magnets has been demonstrated recently [76,77]. For example, in chromium halide, varying the ratio of halides is found to effectively control the ordering temperature and magnetic anisotropy [76]. Furthermore, the competing spin-orbit coupling strength of Cr and halides leads to a new frustrated regime and modified interlayer coupling in $CrCl_{3-x}Br_xI_y$ [77]. However, the chalcogen-substitution effects on magnetism remain elusive in MPX_3 , with only a few syntheses and structural characterization works have been reported [149–152].

In this work, we conducted a systematic study on the magnetic properties of $MnPS_{3-x}Se_x$ and $NiPS_{3-x}Se_x$ ($0 \leq x \leq 3$). We found very different doping dependencies for Néel temperature

(T_N) in those two material systems, likely due to the difference in their dominant exchange interactions i.e, direct $M-M$ interaction in $MnPS_3$ whereas superexchange $M-X-M$ interaction in $NiPS_3$. Furthermore, chalcogen substitution also effectively controls the magnetic anisotropy, which is manifested by the efficient tuning of the magnetic easy axis and spin flop (SF) transition. Such tunable magnetism achieved by non-magnetic substitutions offers a useful technique to engineer low-dimensional magnetism and provides further insights for the development of magnetic materials-based nanodevices.

5.2 Experiment

The $MnPS_{3-x}Se_x$ and $NiPS_{3-x}Se_x$ single crystals used in this work were synthesized by a chemical vapor transport method using I_2 as the transport agent. Elemental powders with desired ratios were sealed in a quartz tube and heated in a two-zone furnace for a week. The $MnPS_{3-x}Se_x$ single crystals were grown with a temperature gradient from 650 to 600 °C, whereas 750 to 550 °C was used for $NiPS_{3-x}Se_x$ growth. The polycrystalline $NiPS_{3-x}Se_x$ samples used in this work were grown using a self-flux method at 750 °C. The as-grown polycrystalline samples were annealed at 750 °C for 4 days to minimize the possible impurity phase. Such annealing process is necessary to obtain a pure phase for characterizing magnetic properties. The elemental compositions and crystal structures of the obtained crystals were examined by energy-dispersive x-ray spectroscopy (EDS) and x-ray diffraction (XRD), respectively. Magnetization measurements were performed in a physical property measurement system (PPMS, Quantum Design).

The calculations were performed by Magdalena Birowska (University of Warsaw, Poland) and Carmine Autieri (Polish Academy of Sciences, Poland; Consiglio Nazionale delle Ricerche CNR-SPIN, Italy) in the framework of the DFT+U [153] approach as implemented in VASP

software [154,155]. The effective on-site Coulomb exchange parameters were set to $U = 5$ eV and $U = 6$ eV for $3d$ states of Mn and Ni atoms, respectively. A cutoff of 400 eV was chosen for the plane-wave basis set and a \mathbf{k} -mesh of $10 \times 6 \times 2$ and $10 \times 6 \times 9$ was taken to sample the first Brillouin zone on Γ -centered symmetry reduced Monkhorst-Pack mesh for monolayer and bulk systems, respectively. The denser \mathbf{k} -mesh grids equal to $15 \times 9 \times 13$ was taken with spin-orbit coupling (SOC) included. The standard exchange-correlation functionals neglect the non-local nature of dispersive forces, which are crucial for layered materials and adsorption molecules on the surfaces [156–158]. Thus, the semi-empirical Grimme method was applied [159]. The lattice parameters have been fixed to the experimental ones. The positions of the atoms were relaxed until the maximal force per atom was less than 10^{-3} eV/Å. The noncollinear magnetism and SOC were included in our calculations.

5.3 Results and discussion

In each layer of MPX_3 , the transition metals M are surrounded by P_2X_6 clusters as shown in Figure 5.1(a). So, the chalcogen substitution in the X site would modify the local environment of M^{2+} within honeycomb layers. Our extensive crystal growth efforts have resulted in sizable single crystals of $MnPS_{3-x}Se_x$ with x up to 3 (i.e., full replacement of S by Se). As shown in Figure 5.1(b), these crystals are relatively transparent, showing a gradual color change from green ($x = 0$) to wine red ($x = 3$), which indicates the variation of the optical gap. On the other hand, for $NiPS_{3-x}Se_x$, good single crystals can only be obtained for x up to 1.3 [Figure 5.1(c)]. Such difficulty in growing single crystals for Se-rich samples could be the reason for the very limited studies on $NiPSe_3$ [38] as compared to $NiPS_3$. The successful substitution in both $MnPS_{3-x}Se_x$ and $NiPS_{3-x}Se_x$ is demonstrated by the composition analyses using EDS. Furthermore, As shown in Figures 5.1(b) and 5.1(c), the $(00L)$ XRD peaks show systematic low-angle shift with

increasing the Se content, consistent with the elongation of c -axis when smaller S is replaced by larger Se.

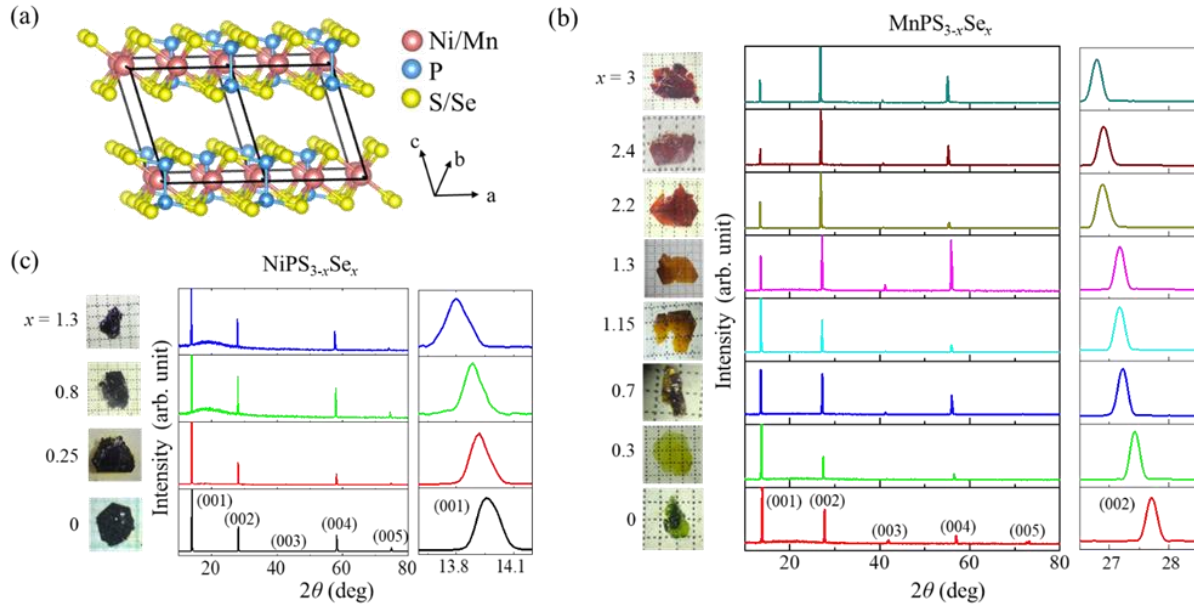


Figure 5.1: (a) Crystal structure of MPX_3 ($M = \text{Mn/Ni}$; $X = \text{S/Se}$). (b) Optical microscope images of the as-grown single crystals and Single-crystal x-ray-diffraction pattern of $\text{MnPS}_{3-x}\text{Se}_x$ ($0 \leq x \leq 3$) showing the $(00L)$ reflections. Right panels show (002) diffraction peak. (c) Optical microscope images of the as-grown single crystals and Single-crystal x-ray-diffraction pattern of $\text{NiPS}_{3-x}\text{Se}_x$ ($0 \leq x \leq 1.3$) showing the $(00L)$ reflections. Right panels show (001) diffraction peak. The value of Se content x for each sample is determined by EDS.

To investigate the effects of Se substitution on magnetic properties, we measured the temperature dependence of molar susceptibility (χ) for $\text{MnPS}_{3-x}\text{Se}_x$ and $\text{NiPS}_{3-x}\text{Se}_x$ under the out of plane ($H \perp ab$) (red color) and in-plane ($H // ab$) (blue color) magnetic fields [Figures 5.2(a) and 5.3(a)]. To obtain the precise transition temperature for each sample, we used the peak position of the derivative $d\chi/dT$ to define T_N [Figures 5.2(b) and 5.3(b)], which has also been widely used in previous studies [62,63,66,120]. As shown in Figures 5.2(a) and 5.3(a), the out-of-plane (χ_{\perp}) and in-plane (χ_{\parallel}) susceptibility for both $\text{MnPS}_{3-x}\text{Se}_x$ and $\text{NiPS}_{3-x}\text{Se}_x$ overlap in the paramagnetic (PM) state but start to deviate below T_N (denoted by black triangles). In earlier studies, both substantial [39,62,66,160] and the lack [31,63,106,118,120] of magnetic anisotropy

in the PM state have been reported. It has also been pointed out that the sample holder may contribute to the observed magnetic anisotropy, especially for the NiPS₃ samples whose magnetization is relatively weak [31]. Therefore, we have been very careful in the magnetization measurements, for which we used the same quartz sample holder for both χ_{\perp} and χ_{\parallel} measurements. For Se-rich NiPS_{3-x}Se_x ($x = 2$ and 3) [Figure 5.3(a)], T_N is obtained from the measurements on polycrystalline samples so that χ_{\perp} and χ_{\parallel} cannot be obtained. The extracted T_N for the end compounds ($x = 0$ or 3) MnPS₃, MnPSe₃, NiPS₃, and NiPSe₃ are 78.5, 74, 155, and 212 K, respectively, consistent with the previous studies [28,31–33,36,38,61,72,73].

Substituting S by Se leads to systematic variations of T_N in both material systems. Such T_N evolution is completely different from that caused by metal substitutions in MnPS₃ and NiPS₃ [56,60,62,64]. In polymetallic mixed compounds such as Ni_{1-x}Mn_xPS₃ [62,64], Mn_xFe_{1-x}PS₃ [56], and Mn_{1-x}Zn_xPS₃ [60], T_N is drastically reduced by substituting magnetic or non-magnetic metal ions, reaching minimum around $x = 0.5$. However, chalcogen substitution only slightly reduces T_N in MnPS_{3-x}Se_x, from 78.5 K for MnPS₃ to 74 K for MnPSe₃ [Figures 5.2(a) and 5.2(c)]. For NiPS_{3-x}Se_x, Se substitution causes T_N to increase monotonically [Figures 5.3(a) and 5.3(c)], which is distinct from the sharp decrease in metal substituted NiPS₃ [62,64]. As will be discussed below, the observed evolutions of T_N with chalcogen substitutions in these two material systems can be understood in terms of the anion-mediated superexchange interactions in addition to the direct M - M exchange. The distinct doping dependences of T_N in those compounds can be attributed to their different magnetic interactions [40,41].

In MPX_3 compounds, substituting S by larger Se expands the in-plane lattice [129,152] and leads to the attenuation of the direct M - M interaction within the metal ion plane [59,65]. In MnPS₃, the neighboring Mn moments are found to be antiparallel and normal to the basal

plane [44,53,162] with an AFM propagation vector $\mathbf{k} = [000]$ [162], as illustrated in Figure 5.2(d). The magnetism in this compound is known to be governed by the Mn-Mn direct exchange interaction [38,40,41]. Therefore, the systematic suppression of T_N by Se substitution in $\text{MnPS}_{3-x}\text{Se}_x$ can be attributed to the weakened direct exchange interaction between the nearest-neighbor Mn ions, due to the elongated Mn-Mn bond. Indeed, weaker Mn-Mn exchange in MnPS_3 in comparison to MnPS_3 has been theoretically proposed [38] and experimentally demonstrated by neutron scattering experiment [72].

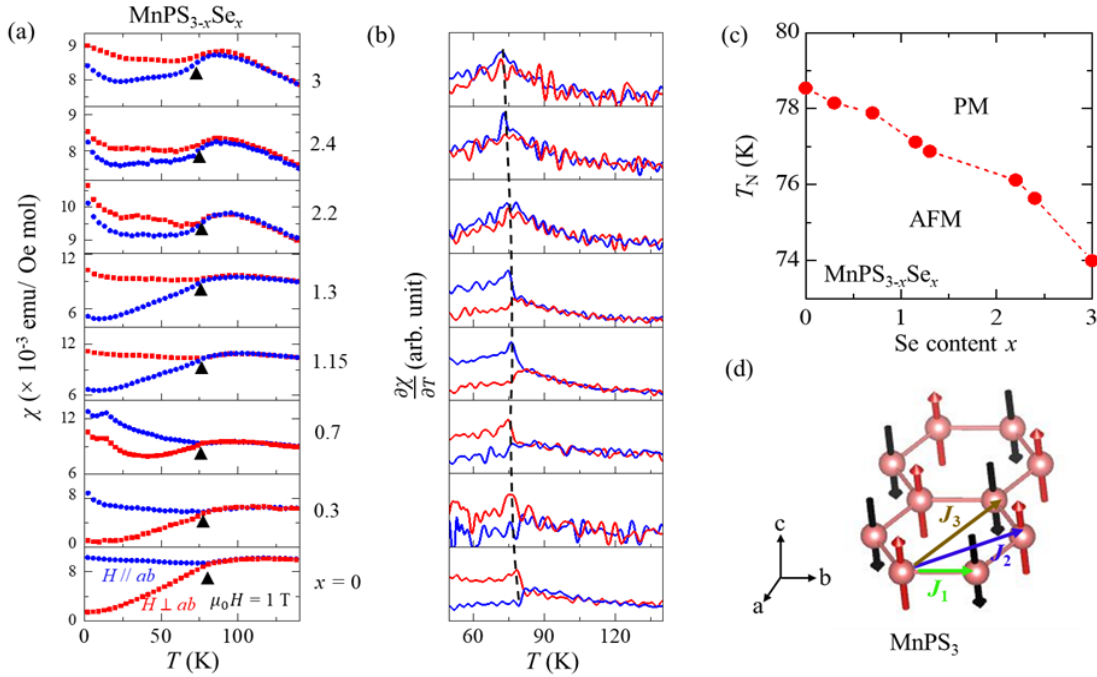


Figure 5.2: (a) Temperature dependence of out-of-plane ($H \perp ab$, red) and in-plane ($H \parallel ab$, blue) molar susceptibility (χ) of $\text{MnPS}_{3-x}\text{Se}_x$ ($0 \leq x \leq 3$) samples. The black triangles denote T_N . (b) Temperature dependence of derivative $d\chi/dT$ of $\text{MnPS}_{3-x}\text{Se}_x$ samples. The dashed lines denote T_N . (c) Doping dependence of Néel temperature (T_N) for $\text{MnPS}_{3-x}\text{Se}_x$. (d) Magnetic structure of pristine MnPS_3 showing nearest-neighbor (J_1), second nearest-neighbor (J_2), and third nearest-neighbor (J_3) interactions.

To clarify the evolution of magnetic exchange interactions (J) upon chalcogen substitutions, we performed the DFT calculations. In order to evaluate the Néel temperatures of bulk MnPS_3 , MnPSe_3 , NiPS_3 and NiPSe_3 structures, we first examine the various magnetic ordering such as antiferromagnetic ones: Néel (AFM-N), zigzag (AFM-z), stripy (AFM-s), and ferromagnetic (FM) one, as reported in another work [163]. We consider the in-plane and out-of-plane directions of the spins, following the previous report [164]. Namely, we consider the Heisenberg Hamiltonian with a single ion anisotropy A :

$$H = E_0 - \frac{1}{2} \sum_{ij} J_{ij} \bar{S}_i \bar{S}_j - \frac{1}{2} \sum_{ij} \lambda_{ij} S_i^z S_j^z - A \sum_i (S_i^z)^2 \quad (1)$$

where $\frac{1}{2}$ accounts for the double-counting, E_0 denotes the energy of the nonmagnetic system, S_i is a spin magnetic moment of the atomic site i . J_{ij} and λ_{ij} are the isotropic and anisotropic exchange couplings between the atomic site i and j , respectively. The off-diagonal isotropic exchange terms have been neglected. The details of these calculations along with derived equations are presented in Appendix. Here, we consider the magnetic exchanges in the monolayer systems up to the third nearest neighbors, neglecting the exchange coupling from adjacent layers. Finally, the Néel temperature has been evaluated in the mean-field approach [40], which takes the following form

$$T_N^{Mn} = S(S+1) (-3J_1 - 6J_2 - 3J_3) / (3k_B) \quad (2)$$

$$T_N^{Ni} = S(S+1) (J_1 - 2J_2 - 3J_3) / (3k_B) \quad (3)$$

for the Mn and Ni compounds, respectively. The difference between equations (2) and (3) is attributed to the different magnetic order of these two compounds. Note that the different sign of J_1 in the equations (2) and (3) produces a different dependence of the T_N from J_1 . Where spin S is equal to $5/2$ and 1 for Mn and Ni, respectively and k_B is the Boltzmann constant. Similar

expressions have been obtained in an earlier work [40]. The results are collected in Table 5 and are in excellent agreement with previous studies [40,41,131]. Note that the Néel temperatures obtained here are overestimated, which is a well-known fact for the systems which exhibit strong critical fluctuations. Although, these critical values are overestimated as expected from the mean-field approximation, the change between the Se and S systems reflects qualitatively the change of the critical temperatures whenever the S atoms are substituted by Se. As shown in Table 5, the calculated nearest-neighbor interaction (J_1) and third nearest-neighbor interaction (J_3) are reduced upon replacing Se for S in MnPX_3 , suggesting the suppression of in-plane exchange interaction on Se substitution, which is in line with the neutron scattering experiment [72]. Note, that for both MnPSe_3 and NiPSe_3 the bond angle between the M-S-M atoms is closer to 90° in comparison to their corresponding Sulphur structures, see Table 5, pointing to the enhancement of the nearest neighbor FM superexchange according to Goodenough-Kanamori-Anderson rules [42,43]. Here, we did not comment on the changes in the second nearest-neighbor interaction (J_2) because it is negligible in both Mn and Ni systems as reported in Table 5. Such attenuation of in-plane magnetic interactions can explain the experimental observation of declining T_N with Se substitution in $\text{MnPS}_{3-x}\text{Se}_x$.

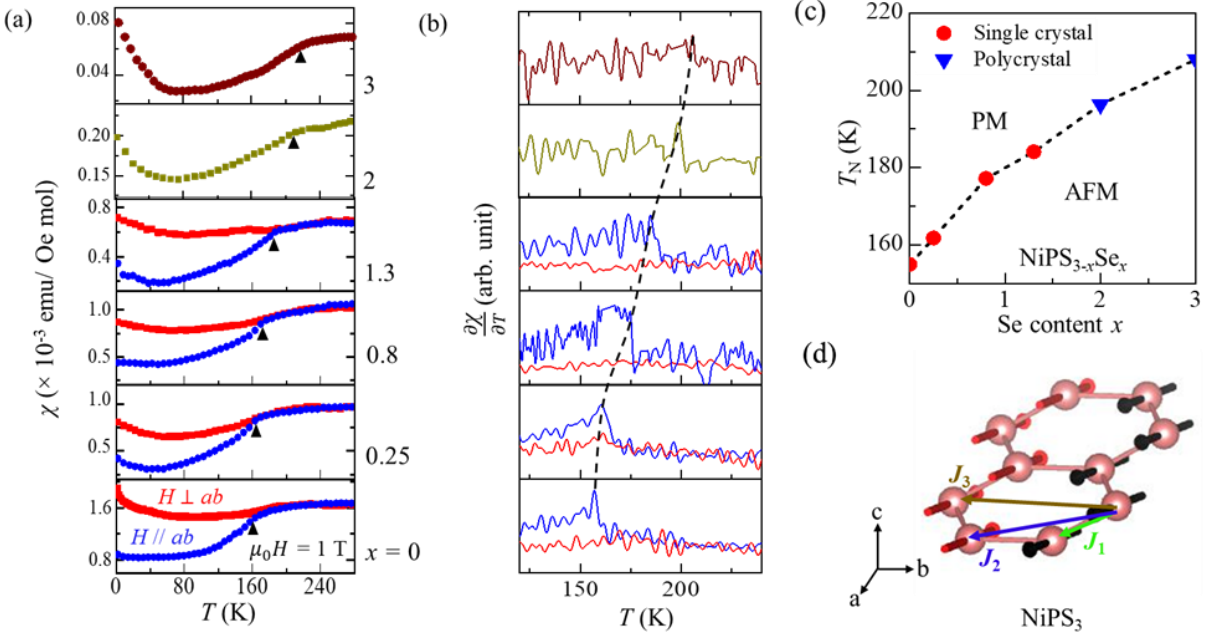


Figure 5.3: (a) Temperature dependence of out-of-plane ($H \perp ab$, red) and in-plane ($H \parallel ab$, blue) molar susceptibility (χ) of $\text{NiPS}_{3-x}\text{Se}_x$ ($0 \leq x \leq 3$) samples. The dark yellow and wine color data represent $x = 2$ and 3 polycrystals samples, respectively. The black triangles denote T_N . (b) Temperature dependence of derivative $d\chi/dT$ of $\text{NiPS}_{3-x}\text{Se}_x$ samples. The dashed lines denote T_N . (c) Doping dependence of Néel temperature (T_N) of $\text{NiPS}_{3-x}\text{Se}_x$. (d) Magnetic structure of pristine NiPS_3 showing nearest-neighbor (J_1), second nearest-neighbor (J_2), and third nearest-neighbor (J_3) interactions.

The situation is different in Se-substituted NiPS_3 . Earlier neutron scattering experiments [38,40] have demonstrated that the magnetic interactions in NiPS_3 occur only through a superexchange pathway. The direct exchange among the metal ions, however, does not exist because of the filled t_{2g} orbitals for Ni^{2+} [38,40]. Therefore, though direct exchange usually significantly influences J_1 in magnetic materials, J_1 in NiPS_3 is superexchange in nature [40,41] and weakly dependent on the Ni-Ni distance [161]. The observed systematic increase of T_N in Se substituted NiPS_3 should be ascribed to the enhanced superexchange interactions. Substituting the non-magnetic ligand atoms is known to effectively tune superexchange in various materials [76,161,165–167]. In general, replacing a smaller ligand with a larger one usually leads

to enhanced superexchange interaction because of the stronger orbital overlap due to greater atom orbitals [76,161]. This can be seen in our DFT calculation, which demonstrates stronger superexchange J_1 and J_3 for NiPSe₃ in comparison to NiPS₃ (Table 5). The result of the calculation depicts the FM and AFM nature of J_1 and J_3 respectively in the Ni system, which is consistent with the reported magnetic structure of NiPS₃ [31] shown in Fig. 3(d). The J_1 of both Mn and Ni systems become more ferromagnetic, but this has a different effect on the two systems due to the different magnetic order as we can see from equations (2) and (3). Although both FM J_1 and AFM J_3 are enhanced upon Se substitution, the larger magnitude of J_3 (almost 4 times) than J_1 explains the stronger AFM interaction in NiPSe₃ than NiPS₃ proposed in an earlier study [38]. This also agrees well with the systematic increase of T_N with Se substitution in NiPS_{3-x}Se_x. Similar T_N enhancement by substituting with larger ligand atoms has also been observed in many other compounds whose magnetic interactions are mainly mediated by superexchange couplings, such as CrCl_{3-x}Br_x [76] and CuCr_{1.5}Sb_{0.5}S_{4-x}Se_x [165].

Table 5: The exchange couplings J_i , the strength of a single ion anisotropy A and M - X - M bond angle using DFT calculations assuming the experimental lattice parameters. Positive (negative) values of J_i and A indicate the FM (AFM) couplings and out-of-plane (in-plane) direction of spins, respectively. The critical temperature is evaluated in mean-field approach.

Structure	J_1 (meV)	J_2 (meV)	J_3 (meV)	λ_1 (meV)	λ_2 (meV)	λ_3 (meV)	A (meV)	T_N (K)	$\sphericalangle M$ - X - M ($^\circ$)
MnPS ₃ ($a = 6.07 \text{ \AA}$, $b = 10.55 \text{ \AA}$)	-1.22	-0.06	-0.43	-4×10^{-5}	-4×10^{-5}	7×10^{-5}	-0.005	181	83.29
MnPSe ₃ ($a = b = 6.32 \text{ \AA}$)	-1.07	-0.06	-0.24	-3×10^{-3}	-4×10^{-3}	-2×10^{-3}	-0.037	145	83.34
NiPS ₃ ($a = 5.81 \text{ \AA}$, $b = 10.07 \text{ \AA}$)	3.53	0.33	-14.06	8×10^{-4}	-8×10^{-4}	2×10^{-3}	-0.108	349	85.13
NiPSe ₃ ($a = 6.15 \text{ \AA}$, $b = 10.66 \text{ \AA}$)	4.53	-0.13	-16.11	-5×10^{-3}	-3×10^{-2}	9×10^{-3}	0.271	411	86.40

Though the elongation of the Ni bonds may not strongly affect exchange interactions in $\text{NiPS}_{3-x}\text{Se}_x$ as mentioned above, it may still mediate the in-plane magnetic interactions. The magnetic structure of NiPS_3 has a propagation vector $\mathbf{k} = [010]$ [31], where the Ni moments lie mostly within the basal plane and form a bi-collinear AFM order consisting of ferromagnetic (FM) chains along the a -axis within the Ni layer as shown in Figure 5.3(d) [25,72,73]. Therefore, the expansion of the in-plane lattice would weaken the intra-chain FM couplings, which may favor the overall AFM interactions of the sample.

Though the different Se substitution-dependent ordering temperatures in $\text{MnPS}_{3-x}\text{Se}_x$ and $\text{NiPS}_{3-x}\text{Se}_x$ can be understood in terms of the mediation of magnetic exchange interactions, the very different effectiveness of tuning T_N by substitution remains. As shown in Figures 5.2(c) and 5.3(c), T_N slightly decreases only by 6% from 78.5 K for MnPS_3 to 74 K in MnPSe_3 , but increases remarkably in $\text{NiPS}_{3-x}\text{Se}_x$, from 155 K for NiPS_3 to 212 K in NiPSe_3 . Such stronger composition dependence in $\text{NiPS}_{3-x}\text{Se}_x$ in contrast to $\text{MnPS}_{3-x}\text{Se}_x$ can be attributed to the larger magnitudes of exchange couplings J_i for Ni structures in comparison to their Mn counterparts (Table 5). Moreover, as suggested by the previous neutron scattering experiment [60], MnPSe_3 shows stronger interlayer exchange interaction J_c than MnPS_3 which may stabilize the magnetic order, so the enhanced J_c with Se substitution may also offset the decrease of T_N driven by reduced intra-layer exchange interaction, leading to the observed weak composition dependence in $\text{MnPS}_{3-x}\text{Se}_x$.

It is worthwhile to compare the distinct effects between chalcogen and metal substitutions in MPX_3 compounds. For polymetallic MPX_3 compounds in which the magnetic M is substituted by other magnetic or non-magnetic metal elements, a remarkable reduction in T_N has been observed [56,60–62,64], which has been ascribed to the suppression of magnetic interactions by

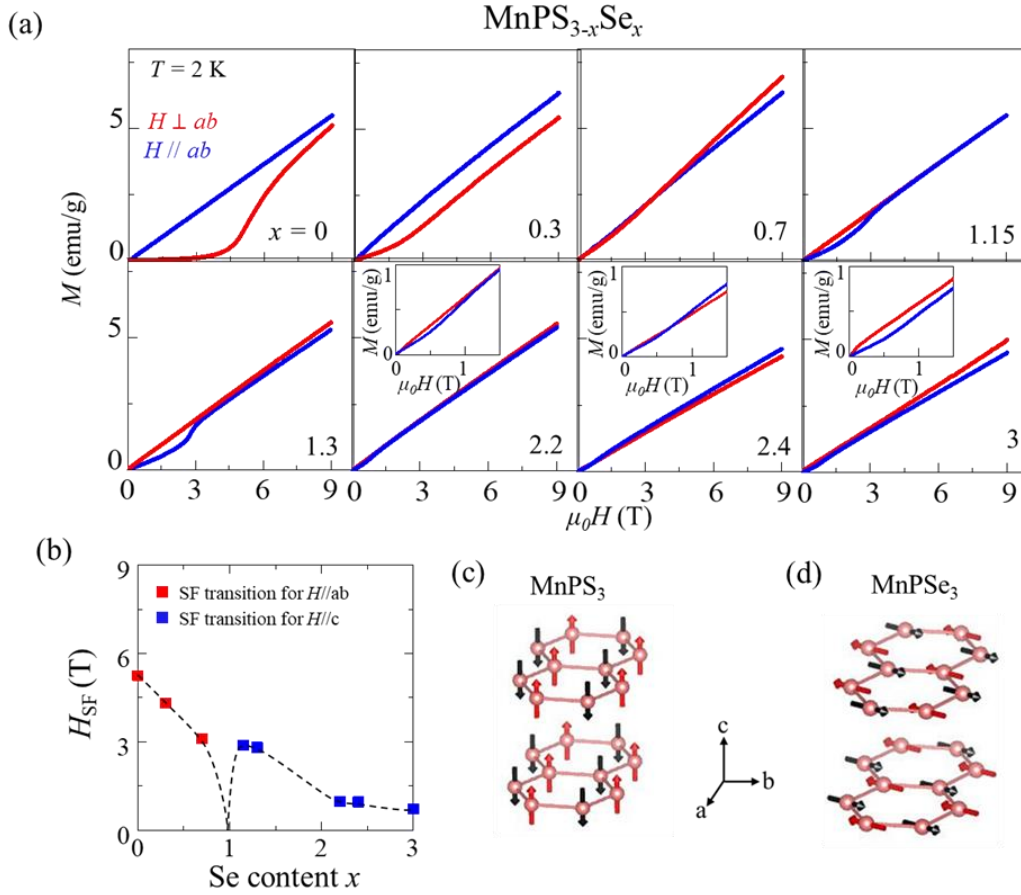


Figure 5.4: (a) Field dependence of magnetization of $\text{MnPS}_{3-x}\text{Se}_x$ samples ($0 \leq x \leq 3$) at $T = 2$ K for out-of-plane ($H \perp ab$, red) and in-plane ($H \parallel ab$, blue) fields. Inset: Low-field magnetizations (b) Doping dependence of Spin-flop field (H_{SF}) of $\text{MnPS}_{3-x}\text{Se}_x$. (c) Magnetic structure of pristine MnPS_3 . (d) Magnetic structure of pristine MnPSe_3 .

random distributions of mixed metal ions, as well as the magnetic frustrations when substituting with magnetic metal elements. Indeed, recent DFT calculation has revealed frustrations among Ni and Mn atoms in $\text{Ni}_{0.75}\text{Mn}_{0.25}\text{PS}_3$ resulting from the competing Néel and zig-zag AFM configurations [131]. The slight suppression in T_N in chalcogen-substituted MPX_3 may imply weaker frustrations compared to the case of metal ion substitutions. This is also consistent with the crystal structures of MPX_3 compounds in which the chalcogen atoms are located away from the magnetic layers [Figure 5.1(a)]. Therefore, substituting chalcogen layers mainly modifies the

environment above and below the magnetic layers, rather than inducing strong magnetic impurities and magnetic dilutions for magnetic [56,62,64] and non-magnetic [53,60] metal-ion substitutions respectively. Hence the chalcogen substitutions could be a better approach to modify magnetism without strongly destabilizing the magnetic orderings in MPX_3 .

Metal-ion substitutions in $NiPS_3$ and $MnPS_3$ have also been found to be effective in tuning magnetic anisotropies [37,39,50,52]. For example, varying the Ni:Mn ratio in $Ni_{1-x}Mn_xPS_3$ can re-orientate the magnetic easy axes from nearly within the ab -plane to along the c -axis [62,64]. In $NiPS_3$, Fe substitution can trigger a crossover from XY to Ising anisotropy [63,66]. Moreover, the magnetic anisotropy in $MnPS_3$ can be reduced with magnetic dilution by substituting non-magnetic Zn [53,60]. In this work, we further studied the evolution of magnetic anisotropy with chalcogen substitutions. Figure 5.4(a) presents the isothermal field-dependent magnetization $M(H)$ at 2K for $MnPS_{3-x}Se_x$ ($0 \leq x \leq 3$) measured under out-of-plane ($H \perp ab$) and in-plane ($H // ab$) magnetic fields. The evolution of magnetic anisotropy can be extracted from the low field (i.e., below the critical field of spin-flop transition) magnetization. The low field magnetic susceptibility is smaller with $H \perp ab$ in Se-less samples. Increasing Se content x gradually reduces anisotropy, and eventually leads the low field out-of-plane magnetization to surpass the in-plane one for $x > 0.7$. Such observation is expected since the two end compounds $MnPS_3$ and $MnPSe_3$ have different easy axis [37,44,53,61,72,73]. As shown in Figures 5.4(c) and 5.4(d), the Mn moments in $MnPS_3$ are aligned along the out-of-plane direction [44,53], whereas they mostly lie within the basal plane with an AFM propagation vector of $\mathbf{k} = [000]$ for $MnPSe_3$ [37,61,72,73]. However, the exact in-plane directions of the moments are unclear or arbitrary based on the neutron scattering experiments on powder samples [50,70,85]. In Figure 5.4(d) we depict a magnetic structure based on a recent neutron scattering

study [72]. The rotation of the easy axis with Se substitution is also supported by the temperature dependent susceptibility below T_N [Figure 5.2(a)], in which χ_{\perp} is smaller than χ_{\parallel} for samples with x up to 0.7 but larger for samples with more Se.

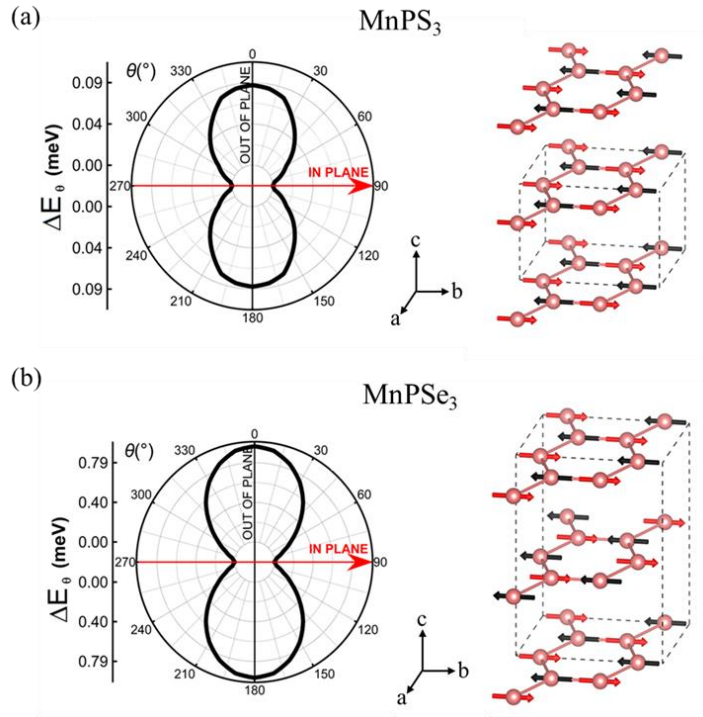


Figure 5.5: (a) Left: Energy difference between the particular direction of the spins and the magnetic ground state for MnPS_3 system including the SOC and neglecting the magnetic dipolar interactions within the DFT studies. The latter is crucial for the proper arrangement of the spins for this system. The θ angle indicates the rotation angle from out-of-plane to in-plane position. Right: Schematic arrangement of the Mn spins in MnPS_3 structure. The theoretical studies predict the easy plane of magnetization in contradiction to the experimental results. (b) Left: Energy difference between the particular direction of the spins and the magnetic ground state for MnPSe_3 system. Right: Schematic arrangements of the Mn spins. Note, that the magnetic ordering within the layer exhibits AFM-Néel type of order, whereas the adjacent layers have antiferromagnetically aligned spins (reversed AFM-N). The easy plane of magnetization is predicted for this system.

The moment orientations in MPX_3 compounds are resulting from the competition between the dipolar and single-ion anisotropy, which favor an out-of-plane and an in-plane moment orientation, respectively. The single-ion anisotropy arises from the combined effects of

the trigonal distortion of MX_6 octahedra and spin-orbit coupling (SOC) [39,64]. In $MnPS_3$, the trigonal distortion and spin-orbit splitting are negligible, so its magnetism is mainly governed by the dipolar anisotropy which results in an out-of-plane moment orientation [39]. Substituting S with Se does not significantly modify trigonal distortion [72], but it causes increased ligand SOC contribution which may enhance single-ion anisotropy [73], leading to the observed moment rotation and the switching of magnetic anisotropy when $x > 0.7$. This is supported by our DFT calculation, which shows the enhancement of single-ion anisotropy (A) in $MnPSe_3$ by almost one order of magnitude as compared to $MnPS_3$ (Table 5). Although the SOC which is responsible for magnetocrystalline anisotropy is accounted in our calculations, the magnetic dipolar interactions are not included in our results. Note that the very recent study has reported a newly developed exchange-correlation functional [168] which accounts for the magnetic dipole-dipole interactions. Considering the $MnPS_3$ system, the inclusion of the SOC causes the spins to lie within the basal plane [Figure 5.5(a)]. This result is obviously in contradiction to the experimental result [Figure 5.4(c)], due to the lack of the inclusion of the magnetic dipolar anisotropy in our calculations, which might align the spins to the out-of-plane direction. In addition to enhanced A , it is also plausible that long-range magnetic dipolar interactions are weakened in $MnPSe_3$ than $MnPS_3$, due to the longer lattice parameters for the Se than S compounds. Thus, the dominant A in Se-rich compounds can be ascribed to the switching of anisotropy from out-of-plane to in-plane direction. Furthermore, unlike $MnPS_3$ whose interlayer magnetic exchange interaction J_c is negligible, a recent neutron scattering experiment has revealed considerable J_c when S is replaced by Se [60], which is not accounted in our theoretical results, and will be studied elsewhere. More theoretical efforts are needed to clarify the possible coupling between J_c enhancement and moment rotation.

Tuning moment orientations in MPX_3 modifies the SF transition [45,53,64]. $MnPS_3$ displays a SF transition when the magnetic field is applied along the out-of-plane direction, which is characterized by a drastic magnetization upturn at the SF transition field (H_{SF}) [Figure 5.4(a)] [10,44,60,62,64,106,118]. Substituting Mn with Ni is found to strongly suppress the SF transition [62,64]. H_{SF} is suppressed by half with only 5% Ni substitution, and disappears for 10% substitution, which is likely due to the reorientation of the magnetic moments when single ion anisotropy is modulated by enhanced lattice trigonal distortion upon substitution [64]. Moreover, though not as efficient as magnetic Ni substitution, the non-magnetic Zn-substitution also reduces H_{SF} , which has been ascribed to the weakening of magnetic anisotropy with magnetic dilution [53]. In this work, modification of the SF transition with Se substitution has also been observed. As shown in Figure 5.4(a), at $T = 2$ K and for $H \perp ab$, the SF transition is gradually suppressed, as manifested by the less-obvious magnetization upturn and reduced H_{SF} . When Se content x is increased beyond 0.7, the observation is inverted. Magnetization displays linear field dependence when $H \perp ab$ but an upturn starts to appear under $H // ab$. Such spin flop transition occurs around ~ 2.9 T in the $x = 1.2$ sample, which remains strong for Se content up to $x = 1.3$ and is gradually suppressed with further increasing the Se content. For the end compound $MnPSe_3$ ($x = 3$), a small upturn around $\mu_0 H = 0.7$ T can be seen in the in-plane magnetization [Figure 5.4(a), inset].

In Figure 5.4(b) we summarize the variation of H_{SF} with Se content for both out-of-plane and in-plane field, from which the two types of SF transitions under $H \perp ab$ and $H // ab$ can be clearly seen. Generally, a SF transition in an AFM compound is characterized by the moment re-orientation that is driven by the magnetic field component parallel to the magnetic easy axis. The change of the moment orientation can be attributed to the enhanced single-ion anisotropy upon

Se substitution as discussed above, which usually favors the in-plane moment orientation. Therefore, in MnPS_3 whose easy axis is out-of-plane, the SF transition is characterized by Mn moment rotation toward the ab -plane under $H \perp ab$ [44,64]. The corresponding H_{SF} is suppressed by Se substitution, because the easy axis in the substituted samples already rotates away from the out-of-plane direction.

One interesting observation is that the switching of the easy axis occurring closer to MnPS_3 side i.e., between $x = 0.7$ and 1.2 [Figures 5.4(a) and (b)], which implies the magnetism in MnPS_3 is softer than MnPSe_3 . This is also consistent with our theoretical calculations. The energy difference between the in-plane and out-of-plane directions of the spins is of the order of a few hundredths of meV in MnPS_3 [Figure 5.5(a), Left panel] and can be considered negligible ($A = -0.005$ meV, Table 5), as reported in earlier works [39–41]. On the other hand, the energy difference in MnPSe_3 [Figure 5.5(b), Left panel] is one order of magnitude greater than in the case of MnPS_3 , which is reflected in the enhancement of the monocrystalline anisotropy ($A = -0.037$ meV, Table 5).

Another interesting feature is that the magnetic ordering temperature does not change remarkably [Figure 5.2(c)] when H_{SF} is drastically suppressed above $x = 0.7$ [Figure 5.4(c)]. Similar observations have also been reported for Ni-substituted MnPS_3 , in which the 10% Ni substitution can fully suppress the SF transition but leaves the ordering temperature essentially unchanged [64]. Such distinct composition dependences for H_{SF} and T_{N} have been attributed to the dominant role of the single ion anisotropy rather than the magnetic exchange in modulating SF transition [64], which may also be applicable for $\text{MnPS}_{3-x}\text{Se}_x$ studied in this work.

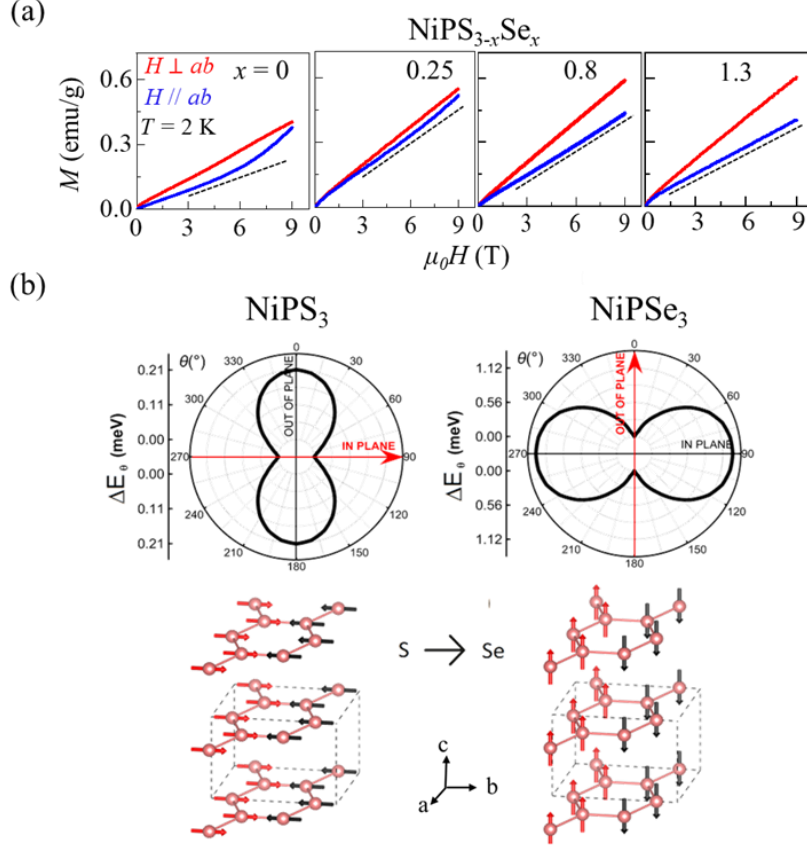


Figure 5.6: (a) Field dependence of magnetization of $\text{NiPS}_{3-x}\text{Se}_x$ samples ($0 \leq x \leq 1.3$) at $T = 2$ K for out-of-plane ($H \perp ab$, red) and in-plane ($H \parallel ab$, blue) fields. The dashed lines are a guide to the eye. (b) Upper Panels: Energy difference between the particular directions of the spins and the magnetic ground state for NiPS_3 and NiPSe_3 using DFT calculations. The spins of the Ni atoms are collinearly aligned. The θ angle indicates the rotation angle from out-of-plane to in-plane position. The changes in rotation angle within the layer are negligible (negligible difference between the spins oriented in a and b directions). Lower Panels: Schematic pictures of magnetic spins for NiPS_3 and NiPSe_3 . Note that, the NiPS_3 exhibits an easy plane (XY) of magnetization, whereas the NiPSe_3 has an easy axis oriented perpendicular to the layer.

Similarly, the rise of SF transition for $H \parallel ab$ is also in line with the rotation of the easy axis toward the basal plane. For the end compound MnPSe_3 , to the best of our knowledge, the isothermal field dependent magnetization has not been reported, though this material has been known for a long time and extensively studied [37,61,72,73]. The observed weak low-field magnetization upturn is suggestive to a SF transition under in-plane magnetic field which is in

line with the in-plane Mn moment orientation [Figure 5.4(d)]. If the SF transition is real, the small $\mu_0 H_{\text{SF}} \approx 1$ T would be the lowest SF field reported so far in MPX_3 family [10,44,60,64,106,118,119]. Such lower H_{SF} in MnPSe_3 might be attributed to the distinct moment re-orientation during the SF transition. For example, the moment may rotate within the basal plane so that H_{SF} is lower, unlike MnPS_3 whose larger H_{SF} may be related to the higher field required to overcome the anisotropy difference between its easy axis and the basal plane. Similar SF mechanism has also been proposed in another Mn system [169].

Now we turn our discussion to $\text{NiPS}_{3-x}\text{Se}_x$. As shown in Figure 5.6(a), consistent with the earlier magnetization studies [62,64], a metamagnetic spin flop transition under an in-plane field of ~ 6 T can be seen in isothermal magnetization measurements. Such observation also agrees with the nearly in-plane orientation for Ni moments [31] due to strong single-ion anisotropy in NiPS_3 [40,41]. Se substitution leads the SF transition to occur at a higher in-plane field of around 8 T for $x = 0.3$. Further increasing Se content leads to essentially linear field-dependent magnetization for both $H//ab$ and $H \perp ab$ up to 9 T. The increased H_{SF} with Se substitution in NiPS_3 is in sharp contrast to observation in $\text{MnPS}_{3-x}\text{Se}_x$ [Figure 5.4(b)]. Unlike the $\text{MnPS}_{3-x}\text{Se}_x$ system for which the magnetic structure for end compounds MnPS_3 [44,53] and MnPSe_3 [37,61,72,73] have been well understood, the lack of the established magnetic structure for NiPSe_3 makes it difficult to clarify how Ni moment orientation may play a role in the observed substitution dependence of H_{SF} in $\text{NiPS}_{3-x}\text{Se}_x$. Our DFT calculation has demonstrated the out-of-plane moment orientation for NiPSe_3 [Figure 5.6(b)]. This agrees well with the possible higher H_{SF} required for Se-rich samples, in a manner similar to $\text{MnPS}_{3-x}\text{Se}_x$, where SF transition occurs at higher H_{SF} for compounds ($x = 0-0.7$) with the easy axis along an out-of-plane direction. In addition to the orientation of the easy axis, the stronger exchange interaction

in Se-substituted NiPS₃ may be another possible factor that affects the H_{SF} . The spin-flop field at low temperatures can be approximately expressed as $H_{SF} \approx \sqrt{2H_E H_A}$ where H_E and H_A are effective exchange and magnetic anisotropy fields, respectively [169]. Since Se substitution enhances the exchange interactions as discussed earlier, increased H_{SF} is expected. To better clarify the mechanism for the evolution of SF transition in NiPS_{3-x}Se_x, future neutron scattering experiments even on polycrystalline samples, magnetization measurements under high magnetic field, and theoretical efforts would be helpful.

5.4 Conclusion

In conclusion, we studied the magnetic properties of previously unreported Se-substituted MnPS₃ and NiPS₃. We found distinct tuning of T_N in MnPS_{3-x}Se_x and NiPS_{3-x}Se_x, likely attributed to different exchange interactions in pristine MnPS₃ and NiPS₃. In addition, magnetic anisotropy is also efficiently modulated with S-Se substitutions. Our findings provide a suitable platform for a deeper understanding of low-dimensional magnetism and potential spintronics applications.

5.5 Appendix: Theoretical exchange couplings

The exchange parameters derived from the Heisenberg Hamiltonian (1):

$$E_{FM}^x = E_0 - \frac{1}{2}(3J_1S^2 + 6J_2S^2 + 3J_3S^2)$$

$$E_{Neel}^x = E_0 - \frac{1}{2}(-3J_1S^2 + 6J_2S^2 - 3J_3S^2)$$

$$E_{zigzag}^x = E_0 - \frac{1}{2}(J_1S^2 - 2J_2S^2 - 3J_3S^2)$$

$$E_{stripy}^x = E_0 - \frac{1}{2}(-J_1S^2 - 2J_2S^2 + 3J_3S^2)$$

$$E_{FM}^Z - E_{FM}^x = \frac{-1}{2}(3\lambda_1 S^2 + 6\lambda_2 S^2 + 3\lambda_3 S^2) - AS^2$$

$$E_{Neel}^Z - E_{Neel}^x = \frac{-1}{2}(-3\lambda_1 S^2 + 6\lambda_2 S^2 - 3\lambda_3 S^2) - AS^2$$

$$E_{zigzag}^Z - E_{zigzag}^x = \frac{-1}{2}(\lambda_1 S^2 - 2\lambda_2 S^2 - 3\lambda_3 S^2) - AS^2$$

$$E_{stripy}^Z - E_{stripy}^x = \frac{-1}{2}(-\lambda_1 S^2 - 2\lambda_2 S^2 + 3\lambda_3 S^2) - AS^2$$

$$J_1 = \frac{1}{4S^2}(-E_{zigzag}^x + E_{stripy}^x - E_{FM}^x + E_{Neel}^x)$$

$$J_2 = \frac{1}{8S^2}(E_{zigzag}^x + E_{stripy}^x - E_{FM}^x - E_{Neel}^x)$$

$$J_3 = \frac{1}{12S^2}(3E_{zigzag}^x - 3E_{stripy}^x - E_{FM}^x + E_{Neel}^x)$$

$$\lambda_1 = \frac{1}{4S^2}(-\Delta E_{zigzag} + \Delta E_{stripy} - \Delta E_{FM} + \Delta E_{Neel})$$

$$\lambda_2 = \frac{1}{8S^2}(\Delta E_{zigzag} + \Delta E_{stripy} - \Delta E_{FM} - \Delta E_{Neel})$$

$$\lambda_3 = \frac{1}{12S^2}(3\Delta E_{zigzag} - 3\Delta E_{stripy} - \Delta E_{FM} + \Delta E_{Neel})$$

$$A = \frac{1}{8S^2}(3\Delta E_{zigzag} + 3\Delta E_{stripy} + \Delta E_{FM} + \Delta E_{Neel})$$

$$\Delta E = E^Z - E^x$$

Note, that the equations for l_3 and J_3 are different than obtained in [164].

Chapter 6: Understanding and tuning magnetism in layered Ising-type antiferromagnet FePSe₃ for potential 2D magnets

Recent discoveries in two-dimensional (2D) magnetism have intensified the investigation of layered magnetic materials. Among various magnetic systems, Ising-type magnets have become one of the important material platforms to explore 2D magnetism because of their strong magnetic anisotropy. Here, we have studied an Ising-type antiferromagnet FePSe₃. We performed S and Mn substitutions in FePSe₃ and characterized their magnetic properties. Our study reveals distinct evolution of magnetic anisotropy and interactions in S and Mn-substituted FePSe₃. This provides a better understanding of an Ising-type magnetism and offers tunable material systems for potential 2D magnets. This chapter is based on the manuscript under preparation.

6.1 Introduction

Recently, two-dimensional (2D) magnetic materials have been widely studied to understand magnetism in atomically thin limit and utilize them for practical applications [6–24,47–50,130]. However, realizing 2D magnets is often challenging because of the limited material choices and experimental tools to probe magnetic properties at the nanometer scale. So, searching for new magnetic van der Waals (vdW) materials and tuning their magnetic properties have become the major research direction in the field of 2D magnetism.

For that reason, the AFM MPX_3 (M = transition metal ions, X = chalcogen ions) materials have been intensively investigated from bulk to monolayer form [10,28,31–37,39,44,46–50,60,62,64,106,107,118,119,148]. Their magnetic anisotropy and exchange are found to be strongly tunable with the choice of M and X [28,31–36,39,44,46,60,62,64,106,107,118,119,148]. This has motivated numerous efforts to tune their

magnetic properties such as substitutions of M [51–66] and X [37,72–75], and inter-layer intercalation [78–80]. This tunable platform has offered a large material pool for exploring 2D magnetism. However, only limited MPX_3 materials such as $NiPS_3$ [49], $MnPS_3$ [10,47], $FePS_3$ [48] and $MnPSe_3$ [24] have been found to exhibit magnetism in 2D limit. In fact, only $FePS_3$ [48] and $MnPSe_3$ [24] demonstrate long-range magnetic ordering down to monolayer, otherwise magnetism is stable up to bilayer in $NiPS_3$ [49] and $MnPS_3$ [10,47]. The persistence of magnetism in monolayer $FePS_3$ [48] and $MnPSe_3$ [50] have been ascribed to their highly anisotropic Ising-type and XY -type antiferromagnetism, respectively. This suggests that magnetic anisotropy is fundamental in assuring magnetic stability in 2D, especially in single layers.

According to the Mermin-Wagner theorem [170], the long-range magnetic ordering is prohibited in 2D systems because of the strong thermal fluctuations. This can be counteracted by a large magnetic anisotropy that leads to the stable magnetic order in 2D. In that case, an Ising-type magnetic system would be of particular interest. Indeed, majority of 2D magnets that are stable up to single layer such as $FePS_3$ [48], CrI_3 [6], $CrBr_3$ [64], VI_3 [65] and Fe_3GeTe_2 [8] exhibit Ising-type magnetic order. Thus, studying new Ising-type magnetic materials and further tuning their magnetic properties would be significant in understanding 2D magnetism and providing novel functionality to 2D magnets.

Given this motivation, we have investigated an Ising-type antiferromagnet $FePSe_3$ [37]. We have successfully engineered the magnetic properties of $FePSe_3$ through chalcogen and metal substitutions. We found distinct effects of S and Mn substitutions in $FePSe_3$ and achieved the strategies to manipulate its magnetic anisotropy and exchange. Our work provides a better understanding of Ising-type magnetism, which will be helpful to study other Ising-type systems as well as magnetic phenomenon in 2D.

6.2 Experiment

The $\text{FePSe}_{3-x}\text{S}_x$ ($0 \leq x \leq 3$) and $\text{Fe}_{1-x}\text{Mn}_x\text{PSe}_3$ ($0 \leq x \leq 1$) single crystals used in this work were synthesized by a chemical vapor transport method using I_2 as the transport agent. Elemental powders with desired ratios were sealed in a quartz tube and heated in a two-zone furnace with a temperature gradient from 750 to 550 °C for a week. The elemental compositions and crystal structures of the obtained crystals were examined by energy-dispersive x-ray spectroscopy (EDS) and x-ray diffraction (XRD), respectively. Magnetization measurements were performed in a physical property measurement system (PPMS, Quantum Design).

6.3 Results and discussion

FePSe_3 shares similar Ising-type magnetic anisotropy with FePS_3 where the Fe moments are aligned along the out-of-plane direction [Figure 6.1(a)] [37,46], but it has been relatively less-explored than FePS_3 [37,61]. The origin of Ising-type anisotropy in FePSe_3 has not been clearly explained, but the combination of strong trigonal distortion of FeS_6 octahedra and spin-orbit coupling (SOC) for high-spin state Fe^{2+} (d^6) have been attributed to highly anisotropic Ising-type magnetism in FePS_3 [39]. Now with enhanced SOC after replacing Se for S, similar reasons can be ascribed for Ising-type anisotropy in FePSe_3 . Even stronger anisotropy can be expected for FePSe_3 in comparison to FePS_3 given the fact that the magnetic anisotropy can be enhanced with Se substitution in MPS_3 [74,172]. This implies that the Ising-type anisotropy could be manipulated by mixing S and Se in FePX_3 ($X = \text{S}$ or Se). Such chalcogen substitution has already proved to be an effective approach to tune the magnetism with less interference from unwanted frustrations in comparison to metal substitutions [74]. Despite inevitable frustration created upon magnetic metal substitution, it is also an important technique to control the magnetic properties in MPX_3 family especially when two parent compounds have different spin

anisotropies for example FePSe_3 and MnPSe_3 . As mentioned above, the Fe moments are pointed along the out-of-plane direction in FePSe_3 [37] whereas MnPSe_3 exhibits XY anisotropy with the Mn moments lying mostly within the basal plane [37,50,72] as shown in Figure 6.1(a). Thus, the S and Mn substitutions could provide different strengths to control magnetism in FePSe_3 .

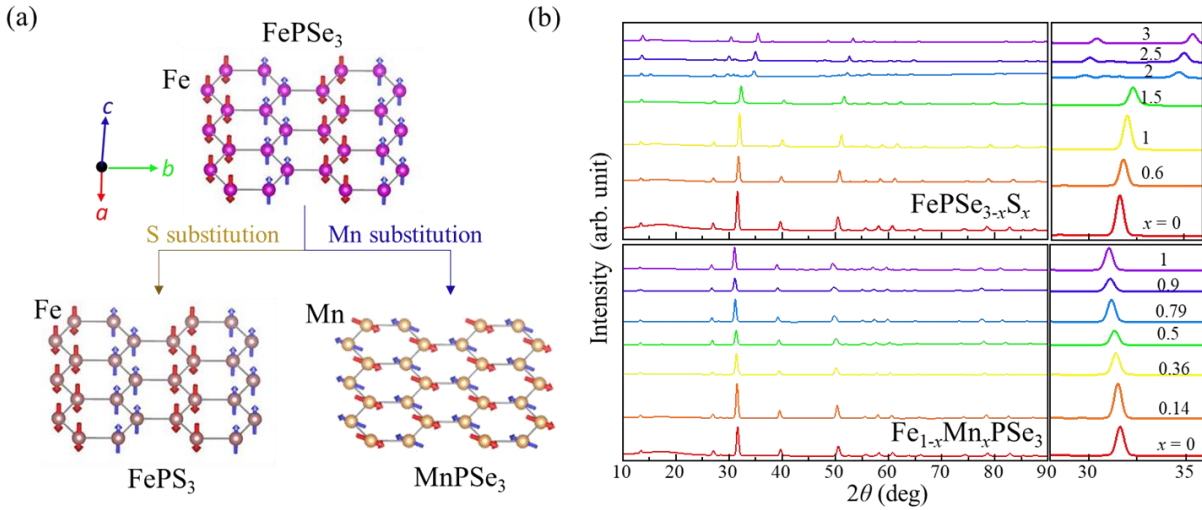


Figure 6.1: (a) Magnetic structures of MPSe_3 ($M = \text{Fe}/\text{Mn}$). (b) Powder x-ray-diffraction pattern of $\text{FePS}_{3-x}\text{Se}_x$ ($0 \leq x \leq 3$) (upper panel) and $\text{Fe}_{1-x}\text{Mn}_x\text{PSe}_3$ ($0 \leq x \leq 1$) (lower panel).

Through extensive crystal growth efforts, we have conducted S and Mn substitutions in FePSe_3 resulting in the sizeable single crystals of $\text{FePSe}_{3-x}\text{S}_x$ ($0 \leq x \leq 3$) and $\text{Fe}_{1-x}\text{Mn}_x\text{PSe}_3$ ($0 \leq x \leq 1$) in the whole compositional range. So far, the magnetic properties of S-substituted FePSe_3 have not been studied, but the polycrystals $\text{Fe}_{1-x}\text{Mn}_x\text{PSe}_3$ have been investigated [61]. Here, we have focused on single crystalline $\text{Fe}_{1-x}\text{Mn}_x\text{PSe}_3$ ($0 \leq x \leq 1$) which is usually purer than polycrystals and convenient to measure directional dependence of the magnetization. The successful S and Mn substitutions in FePSe_3 were demonstrated by composition analysis using EDS. These substitutions are further confirmed by the evolution of the crystal lattices. It has been reported that the crystal structure for FePSe_3 (Rhombohedral; $R\bar{3}$ space group) is different than that of FePS_3 (Monoclinic; $C2/m$ space group) but same as MnPSe_3 [61]. Here, we have

obtained distinct XRD spectra for Se-rich and S-rich samples in $\text{FePSe}_{3-x}\text{S}_x$ whereas $\text{Fe}_{1-x}\text{Mn}_x\text{PSe}_3$ samples display similar XRD spectra in the entire composition range as shown in Figure 6.1(b). In $\text{FePSe}_{3-x}\text{S}_x$, two sets of XRD spectra have been obtained below and above $x = 1.5$, implying crystal structure transition near that composition which is in line with the reported crystal structure characterization [152]. The structure transition has been confirmed by crystal structure refinement using powder XRD on $\text{FePSe}_{3-x}\text{S}_x$ ($0 \leq x \leq 3$) samples, which was done by Prof. Jian Wang (Wichita state university, USA) and will be shown later in Figure 6.4(b). Whereas the similar XRD spectra obtained for $\text{Fe}_{1-x}\text{Mn}_x\text{PSe}_3$ indicates unchanged crystal structure, consistent with an earlier study [61]. Nevertheless, the $\text{Fe}_{1-x}\text{Mn}_x\text{PSe}_3$ XRD peaks exhibit systematic low-angle shift with increasing Mn content [Figure 6.1(b)] suggestive of expanding crystal lattice due to incorporation of larger Mn atoms, which is already reported in previous study [61].

Although the metal [51–66] and chalcogen-substituted [37,72–75] MPX_3 demonstrate tunable magnetism, their studies in 2D still remain elusive. Here, we have investigated the magnetic properties of $\text{FePSe}_{3-x}\text{S}_x$ and $\text{Fe}_{1-x}\text{Mn}_x\text{PSe}_3$ material series to understand how they can be utilized as potential 2D magnets. For this, we have measured the temperature dependence of susceptibility (χ) under the out-of-plane ($B \perp ab$) (Solid line) and in-plane ($B // ab$) (Dashed line) magnetic fields of $B = 0.1$ T [Figure 6.2(a)]. As shown in Fig. 2(a) for pristine FePSe_3 ($x = 0$) and FePS_3 ($x = 3$), the temperature dependence of out-of-plane (χ_{\perp}) and in-plane (χ_{\parallel}) susceptibility exhibit significant anisotropy below and above magnetic transition temperature (T_N) (denoted by black triangles in Figure 6.2), consistent with previous reports [39,48,66] and can be ascribed to their highly anisotropic Ising-type magnetism. The anisotropic susceptibility remains unaffected after chalcogen substitutions as shown in Figure 6.2(a), suggesting the Ising-

type magnetic order in the entire composition range in $\text{FePSe}_{3-x}\text{S}_x$. This is in stark contrast to $\text{MnPS}_{3-x}\text{Se}_x$ and $\text{NiPS}_{3-x}\text{Se}_x$ where the anisotropy is observed only below T_N [74], which can be understood in terms of their relatively weaker magnetic anisotropy [31,32,39]. Similar to $\text{FePSe}_{3-x}\text{S}_x$, a clear anisotropy between χ_{\perp} and χ_{\parallel} in AFM and paramagnetic (PM) regions is also observed in $x = 0$ (pristine FePSe_3) and 0.36 Mn-substituted FePSe_3 samples [Fig. 2(b)] but starts to suppress with increasing Mn content and ultimately leads to magnetic anisotropy only below T_N for higher Mn-doped samples ($x = 0.5$ to 1). This is suggestive of varying magnetic anisotropy with Mn substitution, which is in line with relatively weaker XY -type anisotropy for pristine MnPSe_3 in comparison to FePSe_3 [37,50,61,72]. These results indicate that S substitution has weaker effect on magnetic anisotropy whereas it is tunable with Mn substitution in FePSe_3 .

Tuning magnetic anisotropy in MPX_3 can effectively change the moment direction [39,64,74]. So, the lack of strong modification of magnetic anisotropy implies the unchanged magnetic easy axis in $\text{FePSe}_{3-x}\text{S}_x$. In fact, the susceptibility for all $\text{FePSe}_{3-x}\text{S}_x$ samples display similar temperature dependence: χ_{\perp} decreases sharply below T_N in contrast to weakly temperature dependent χ_{\parallel} [Figure 6.2(a)]. This behavior indicates the out-of-plane moment orientation for all $\text{FePSe}_{3-x}\text{S}_x$ samples, consistent with the reported magnetic structures of pristine FePSe_3 [37] and FePS_3 [46] that remain intact with chalcogen substitution. This is distinct than the strong tuning of spin anisotropies in chalcogen-substituted $\text{MnPSe}_{3-x}\text{S}_x$ and $\text{NiPSe}_{3-x}\text{S}_x$ [74]. Such different behavior upon chalcogen substitution can be attributed to their different sources for magnetic anisotropy. In Mn and Ni systems, the orbital angular momentum (L) is quenched for Mn^{2+} and Ni^{2+} because of their half and fully filled t_{2g} orbitals respectively that lead to the negligible SOC for the magnetic atoms [39]. Now with minimum contribution from Mn^{2+} and Ni^{2+} , the modification of magnetic anisotropy in $\text{MnPSe}_{3-x}\text{S}_x$ and $\text{NiPSe}_{3-x}\text{S}_x$ is mainly

determined by varying SOC due to non-magnetic ligands substitution [73,172]. On the other hand, the strong SOC for Fe^{2+} leads to much higher single-ion anisotropy (A) for FePS_3 ($A \approx 2.66$ meV) than MnPS_3 ($A \approx 0.0086$ meV) and NiPS_3 ($A \approx 0.3$ meV) [40,46]. This means the dominant contribution to the magnetic anisotropy in FePS_3 arises from the Fe^{2+} SOC, so the chalcogen substitution has less effect on the anisotropy in $\text{FePSe}_{3-x}\text{S}_x$.

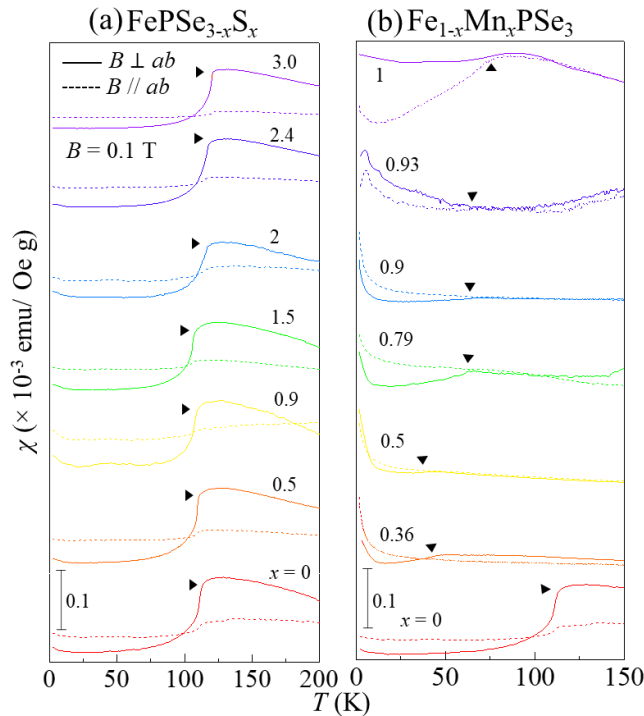


Figure 6.2: (a) Temperature dependence of out-of-plane ($B \perp ab$, solid line) and in-plane ($B \parallel ab$, dashed line) susceptibility (χ) of (a) $\text{FePSe}_{3-x}\text{S}_x$ ($0 \leq x \leq 3$) and (b) $\text{Fe}_{1-x}\text{Mn}_x\text{PSe}_3$ ($0 \leq x \leq 1$) samples. The black triangles denote Néel temperature (T_N).

The magnetic easy axis also remains intact after Mn substitution as high as 90% ($x = 0.9$ sample). For all Mn-substituted samples up to $x = 0.9$ [Figure 6.2(b)], the temperature dependent susceptibility below T_N exhibits smaller χ_{\perp} than χ_{\parallel} that is indicative of out-of-plane easy axis. When the amount of Mn is further increased, χ_{\perp} surpasses χ_{\parallel} below T_N as seen in $x = 0.93$ and 1 samples. This indicates the switching of easy axis towards the in-plane direction, consistent with

the magnetic structure of pristine MnPSe_3 [37,72]. Similar result has been observed in Ni-substituted FePS_3 , where 90% Ni substitution is unable to modify the easy axis of FePS_3 [63,173]. Such robust magnetism in Fe-based MPX_3 is associated with their highly anisotropic Ising-type magnetic order. When two ions with different anisotropies are mixed, a strongly anisotropic ion dictates the ion with weaker anisotropy forcing them to behave like the highly anisotropic parent compound [173]. For example the magnetic moments start to rotate towards ab -plane in MnPS_3 after substituting just 5% Ni^{2+} which has stronger single-ion anisotropy than Mn^{2+} [64].

Despite Mn substitution (up to 90%) is unable to completely switch the easy axis along the ab -plane, it is still capable to drive spin reorientation in FePSe_3 . This is illustrated by the low-temperature upturn in susceptibility starting from $x = 0.14$ sample [Figure 6.2(b)] which is not seen upon chalcogen substitution [Figure 6.2(a)]. Similar upturn in susceptibility as a result of spin reorientation has been observed in pristine [174,175] and Ni-substituted MnPS_3 [64]. The rise in the low-temperature susceptibility becomes stronger on increasing the Mn substitution [Figure 6.2(b)], suggesting the enhanced spin reorientation away from the out-of-plane direction. Now, the easy axis has started to rotate towards the basal plane, when 93% Fe is replaced by Mn ($x = 0.93$ sample) the easy axis starts to switch along the in-plane direction. The moment rotation in Mn-substituted FePSe_3 is consistent with tuning of its magnetic anisotropy as discussed earlier and can be explained by different spin anisotropies for pristine MnPSe_3 and FePSe_3 [37,50,72] [Figure 6.1(a)].

The spin reorientation with Mn substitution is also supported by the field dependent magnetization under the out-of-plane ($B \perp ab$) (Red color) and in-plane ($B // ab$) (Blue color) magnetic fields at $T = 2$ K. As seen in Figure 6.3(b), the higher Mn-substituted samples $x = 0.79$

and 0.9 exhibit clear metamagnetic transitions under an out-of-plane field in isothermal magnetization measurement. Such metamagnetic transition has been attributed to spin-flop (SF) transition in MPX_3 materials [44,62,64]. Generally, a SF transition in an AFM compound is characterized by the moment reorientation that is driven by the magnetic field component parallel to the magnetic easy axis. The metamagnetic transition is absent in samples below $x = 0.79$ including pristine $FePSe_3$ ($x = 0$). The linear magnetization in pristine $FePSe_3$ is understandable given its highly anisotropic magnetism that might require a strong magnetic field to force moment reorientation. This could be a reason that a metamagnetic transition in $FePS_3$ occurs at very high field ($B > 35T$) [119] as compared to $MnPS_3$ [44,64] and $NiPS_3$ [64]. Similar linear field-dependent magnetization is observed for all $FePSe_{3-x}S_x$ samples when $B \perp ab$ and $B // ab$ [Figure 6.3(a)], which is consistent with their highly anisotropic nature as discussed earlier. Thus, the metamagnetic transition in $x = 0.79$ and 0.9 Mn-substituted samples suggest the spin reorientation due to reduced magnetic anisotropy induced by Mn substitution. The modification of anisotropy has led to moment rotation from out-of-plane to in-plane direction in Ni [64] and Se-substituted [74] $MnPS_3$. Now, since pristine $MnPSe_3$ exhibits in-plane moment orientation, similar rotation of moments towards the ab -plane is reasonable to take place in Mn-substituted $FePSe_3$. In fact, it has been proposed that the pristine $FePS_3$ undergoes spin canting towards a -axis when field is applied along its easy axis [176], which could be facilitated when Mn is substituted for Fe. Now, the easy axis already rotates towards the basal plane, it is understandable that the higher Mn-substituted samples $x = 0.79$ and 0.9 exhibit the field-induced metamagnetic transition at relatively lower $B \perp ab$ magnetic field in a manner similar to Ni [64] and Se-substituted [74] $MnPS_3$. When the moments start to align along the in-plane direction for $x = 0.93$ as suggested by the temperature-dependent susceptibility measurements in Fig. 2(b), the

metamagnetic transition is seen only for $B//ab$ field ($B \approx 1.5$ T). Finally, the metamagnetic transition appears at even lower $B//ab$ field ($B \approx 0.5$ T) [Figure 6.3(b)] after complete switching of easy axis towards the ab -plane in MnPSe_3 .

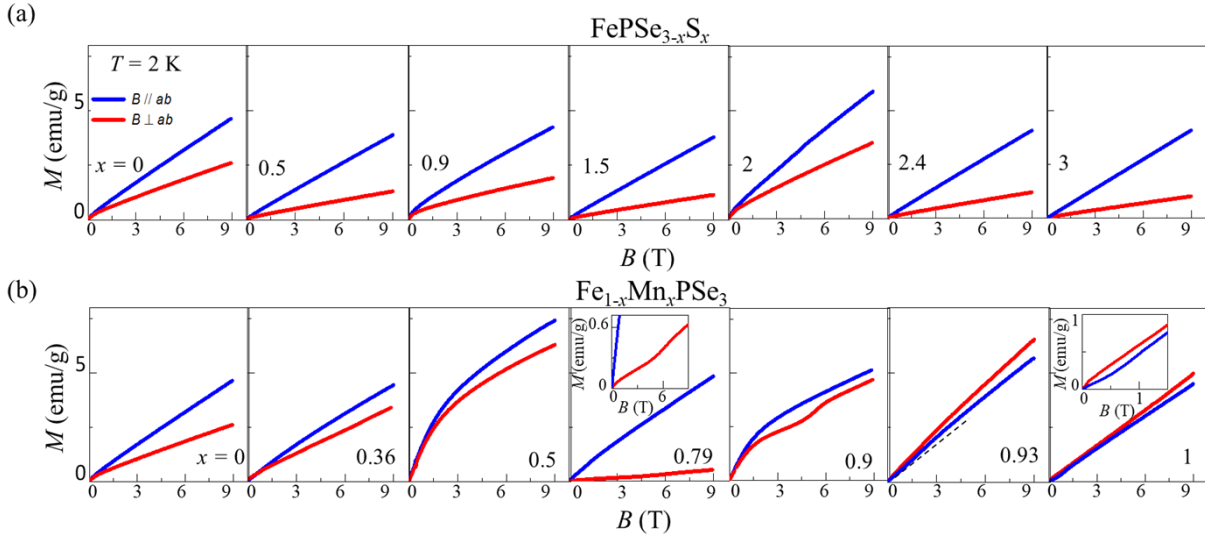


Figure 6.3: Field dependence of magnetization of (a) $\text{FePS}_{3-x}\text{S}_x$ ($0 \leq x \leq 3$) (b) $\text{Fe}_{1-x}\text{Mn}_x\text{PSe}_3$ ($0 \leq x \leq 1$) samples at $T = 2$ K for out-of-plane ($B \perp ab$, solid line) and in-plane ($B // ab$, dashed line) fields. Inset: Low-field magnetizations.

Though our results demonstrate the tuning of the moment orientation upon Mn substitution, the magnetic anisotropy in FePSe_3 still appears to be strongly immune towards doping. We can conclude that the Ising-type magnetism in FePSe_3 has a strong tendency to maintain its magnetic order. Such robust magnetism is essential to realize 2D magnets and explains the reason for most of the 2D magnets [6,8,48,132,171] belonging to Ising-type system. We observed the strong anisotropy in $\text{FePSe}_{3-x}\text{S}_x$ materials that make them suitable candidates to explore 2D magnetism in a mixed system. On the other hand, the magnetic anisotropy is found to be reduced with Mn substitution that may be detrimental to stabilize magnetic ordering in 2D. However, the neutron scattering experiments demonstrate substantial anisotropy in $\text{Fe}_{1-x}\text{Mn}_x\text{PSe}_3$

samples [61] that might be the reason for the existence of magnetic order in monolayer MnPSe₃ [50]. This implies that Fe_{1-x}Mn_xPSe₃ compounds could also be potential candidates for 2D magnets.

In Fe_{1-x}Mn_xPSe₃, there is one possible challenge that could prevent the persistence of magnetism in 2D limit. When two magnetic metal atoms are mixed, a strong frustration arises in the system. Such frustration would weaken the magnetic correlation within the magnetic plane. In addition to the strong thermal fluctuation the presence of magnetic frustration in Fe_{1-x}Mn_xPSe₃ may hinder the magnetic ordering in 2D. The frustration is minimized upon ligand substitution because they mainly modify the local environment around *M* atoms without touching the magnetic layers [74]. Such lack of frustration can be understood in terms of the systematic variations of T_N in chalcogen-substituted MnPS₃ and NiPS₃ [74]. Otherwise the T_N would drastically reduce with substitution reaching minimum around $x = 0.5$ composition as in the case of polymetallic compounds [56,60,62,64]. So, the role of the frustration can be clarified by the composition dependence of the magnetic transition temperature (T_N).

To obtain the precise transition temperature, we calculated the derivative $d\chi/dT$ for susceptibility data shown in Figure 6.2 and used their peak position to define T_N [Figure 6.4(a)], which has also been widely used in previous studies [62,63,66,74,120]. The extracted T_N for the end compounds FePSe₃, FePS₃, and MnPSe₃ are 111.1, 120.1, and 73.4 K, respectively, consistent with the reported results [37,46,61,74,107]. As shown in Figures 6.4(a and b), both FePSe_{3-x}S_x and Fe_{1-x}Mn_xPSe₃ samples exhibit similar non-monotonic composition dependent T_N . As expected frustration for Fe_{1-x}Mn_xPSe₃, the T_N is minimized when $x = 0.5$, consistent with an earlier study on powder Fe_{1-x}Mn_xPSe₃ [61]. Despite similar composition dependence of T_N , the suppression of T_N in S-substituted FePSe₃ is much smaller ($\approx 4.7\%$ after 50% S-Se substitution)

in comparison to Mn substitution ($\approx 67.2\%$ for 50% Fe-Mn substitution). So, the non-monotonic change of T_N in $\text{FePSe}_{3-x}\text{S}_x$ may not be due to frustration as in the cases of $\text{MnPSe}_{3-x}\text{S}_x$ and $\text{NiPSe}_{3-x}\text{S}_x$ [74]. This is understandable because of the fact that frustration did not significantly affect the magnetic interactions in MnPS_3 and NiPS_3 [74], so it is less likely to be functional in $\text{FePSe}_{3-x}\text{S}_x$ due to their strong magnetic anisotropy which makes them more immune towards frustration.

According to neutron scattering experiments, the overall magnetic interactions in Mn and Ni systems are governed by nearest-neighbor (J_1) and third nearest-neighbor (J_3) exchanges in MnPS_3 and NiPS_3 , respectively [40]. The neutron scattering measurement has revealed dominant J_1 in FePS_3 [46]. However, the magnetic exchange parameters for FePSe_3 have not been precisely determined yet [37]. In addition, the J_1 and J_3 are ferromagnetic and antiferromagnetic respectively [46] for FePS_3 as shown in Figure 6.4(d), which are mediated through direct and superexchange pathways respectively [40,46]. This implies that the magnetic interaction in FePS_3 is stabilized by the competition between FM J_1 and AFM J_3 . The superexchange J_3 is suppressed with increasing x in $\text{FePSe}_{3-x}\text{S}_x$ because of the weaker orbital overlap due smaller atom orbital for S [74]. This suggests lower T_N for FePS_3 as compared to FePSe_3 , but in fact FePS_3 has higher T_N than FePSe_3 [46,61]. This implies that the direct J_1 which depends on the nearest neighbor Fe-Fe distance plays a major role in non-monotonic evolution of T_N in $\text{FePSe}_{3-x}\text{S}_x$. Indeed, we have obtained the non-linear composition dependence of Fe-Fe distance through structure refinement using powder XRD for $\text{FePSe}_{3-x}\text{S}_x$ [Figure 6.4(b)], suggesting non-monotonic modification of J_1 which can explain the observed composition dependence of T_N in $\text{FePSe}_{3-x}\text{S}_x$. Thus, $\text{FePSe}_{3-x}\text{S}_x$ exhibit tunable magnetic exchange with chalcogen substitution but

maintain the strong anisotropy. On the other hand, despite frustration in the system the magnetic anisotropy can be modulated with metal substitution in $\text{Fe}_{1-x}\text{Mn}_x\text{PSe}_3$.

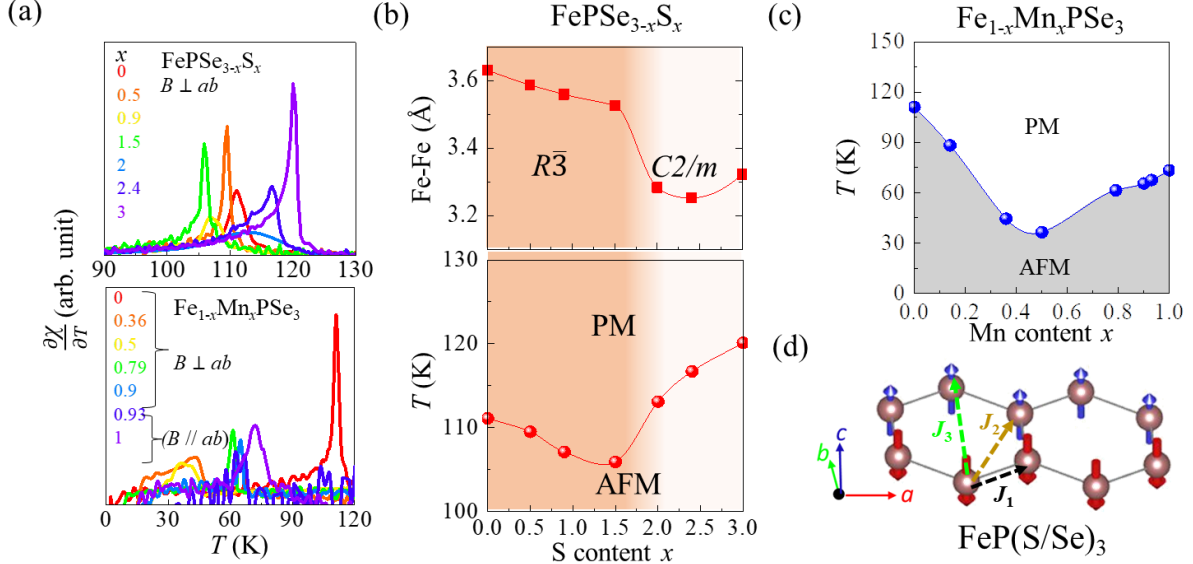


Figure 6.4: (a) Temperature dependence of derivative $d\chi/dT$ of $\text{FePS}_{3-x}\text{Se}_x$ ($0 \leq x \leq 3$) (upper panel) and $\text{Fe}_{1-x}\text{Mn}_x\text{PSe}_3$ ($0 \leq x \leq 1$) (lower panel) samples. (b) Doping dependence of Fe-Fe distance (upper panel) and Néel temperature (T_N) (lower panel) for $\text{FePS}_{3-x}\text{Se}_x$. (c) Doping dependence of T_N for $\text{Fe}_{1-x}\text{Mn}_x\text{PSe}_3$. (d) Magnetic structure of pristine FeP(S/Se)_3 showing nearest-neighbor (J_1), second nearest-neighbor (J_2), and third nearest-neighbor (J_3) interactions.

6.4 Conclusion

In conclusion, we have studied the magnetic properties of $\text{FePS}_{3-x}\text{S}_x$ and $\text{Fe}_{1-x}\text{Mn}_x\text{PSe}_3$. We found robust magnetic anisotropy in pristine FePSe_3 that can be attributed to its Ising-type magnetism, which can be manipulated through Mn substitution. In addition, they exhibit similar non-monotonic composition dependence of T_N , arising due to tunable magnetic exchange and frustration in S and Mn-substituted FePSe_3 , respectively. Our study provides a deeper understanding of an Ising-type magnetic system, which will offer important strategies to discover novel 2D magnets and further clarify magnetic phenomenon in 2D.

Chapter 7: Emergence of possible ferrimagnetism in Li-intercalated NiPS₃

Intercalation has become a powerful approach to tune the intrinsic properties and introduce novel phenomena in layered materials. Intercalating van der Waals (vdW) magnetic materials is a promising route to engineer the low-dimensional magnetism. Recently, metal thiophosphates, MPX_3 , has been widely studied because their magnetic orders are highly tunable and persist down to the two-dimensional (2D) limit. In this work, we used electrochemical technique to intercalate Li into NiPS₃ single crystals and found the emergence of ferrimagnetism at low temperature in Li-intercalated NiPS₃. Such tuning of magnetic properties highlights the effectiveness of intercalation, providing a novel strategy to manipulate the magnetism in vdW magnets. This chapter is based on our published work in JOURNAL OF PHYSICS: CONDENSED MATTER 34, 434002 (2022) (<https://doi.org/10.1088/1361-648X/ac8a81>) [80].

7.1 Introduction

Intercalation of guest species into layered materials has been established as an effective technique to modulate their magnetic [78,86–89,177–182], electronic [98,99,183–188] and optical properties [183,186]. Recently, investigation of vdW magnetic materials and further tuning their magnetic properties have intensified for both fundamental research and practical applications [18–23].

Tunable magnetism has been intensively studied in AFM MPX_3 (M = transition metal, X = chalcogen S, Se) compounds which exhibit diverse AFM states with distinct magnetic exchanges and anisotropies depending on the choice of transition metal M [28,31–36,39,44,46,60,62,64,106,107,118,119] and chalcogen X [37,72,73]. Substituting M in MPX_3 has been widely adopted as an important technique to modify magnetism [51–66]. A series of polymetallic “mixed” MPX_3 compounds such as Ni_{1-x}Mn_xPS₃, Mn_xFe_{1-x}PS₃, Fe_{1-x}Ni_xPS₃, Mn₁₋

$x\text{Zn}_x\text{PS}_3$, $\text{Ni}_{1-x}\text{Co}_x\text{PS}_3$ and $\text{Mn}_{1-x}\text{Fe}_x\text{PSe}_3$ have been found to be efficient in tailoring the magnetism of parent compounds [51–66]. Furthermore, substituting S with Se has also been found to be effective in tuning magnetism [37,72–74]. These doping studies are all based on the direct mixing of dopants and source materials during synthesis such as flux and chemical vapor transport (CVT). In addition to substitution, the layered structure of MPX_3 allows for another doping strategy: the inter-layer intercalation of guest ions. A few intercalation works in MPX_3 has been reported, which demonstrates successful tuning of their magnetism [78,86–89,180–182].

Among MPX_3 materials, tuning the magnetic properties through intercalation have been focused on NiPS_3 [86–89], which may be due to its high reactivity towards intercalation as compared to other MPX_3 materials [89]. The reduction in magnetic susceptibility has been observed in Li-intercalated NiPS_3 , while no noticeable changes in FePS_3 , FePSe_3 and MnPSe_3 [89]. In addition, various organic-ion intercalations have been found to induce AFM-to-ferrimagnetic (FIM) [78,86,88] or ferromagnetic (FM) [87] transitions in NiPS_3 . These are in sharp contrast to that of metal- or chalcogen-substituted NiPS_3 [58,62–66,74] which features no such transitions. These differences might be attributed to different consequences of substitution and intercalation: substitution plays a role mainly in altering magnetic anisotropy and exchange interactions. Intercalation, however, might lead to carrier doping which is predicted to drive AFM-to-FM transitions [30,85]. Thus, intercalation could be a promising route to achieve various magnetic phases in MPX_3 that are not accessible by substitution.

In this work, we performed electrochemical intercalation of lithium (Li) into NiPS_3 single crystals, Li_xNiPS_3 ($0 \leq x \leq 0.4$), and studied their magnetic properties. We found the emergence of FIM state at low temperature arising from the uncompensated moments due to Li

intercalation. Such variation in magnetic properties provides a novel tunable platform that could be useful for understanding low-dimensional magnetism as well as future technological applications.

7.2 Experiment

The NiPS₃ single crystals used in this work were synthesized by a CVT method using I₂ as the transport agent. Elemental powders with desired ratios were sealed in a quartz tube and heated in a two-zone furnace with a temperature gradient from 750 to 550 °C for a week. The electrochemical intercalations of Li into NiPS₃ single crystals were performed in a two-electrode battery system using electrochemical workstation (Battery testing system 8.0, Neware). The crystal structures of the obtained crystals were examined by x-ray diffraction (XRD). Magnetization and heat capacity measurements were performed in a physical property measurement system (PPMS, Quantum Design).

7.3 Results and discussion

Earlier experimental [62,64] and theoretical [175] studies revealed the magnetic frustrations in metal-substituted NiPS₃ due to mixed magnetic elements in the lattice leading to a remarkable reduction in T_N . The insertion of guest ions into inter-layer spaces leaves the host layers relatively clean. So, intercalation could be an alternative route to modify the magnetism without touching the magnetic layers. Previous intercalations of Li [89], cobaltocene [87], and 1,10-phenanthroline [86] in NiPS₃ have successfully modified its magnetic properties. In those studies, the intercalation was performed by immersing host materials in solutions containing intercalant. Compared with such a wet chemical process, electrochemical intercalation is more controllable [176] and can provide quantitative information. First, the intercalation is driven by electrical force so a much greater amount of intercalant might be possible. Additionally, the

process is facilitated by the applied external electric field or potential. Therefore, the doped charges and hence the amount of intercalant can be quantitatively controlled by the amplitude of current and the intercalation time. And finally, the complete process can be monitored by measuring the voltage and current, from which the intercalation to sample internal and electrochemical plating on sample surface can be distinguished. Recently, electrochemical technique has been used to intercalate organic-ions such as tetrabutylammonium (TBA^+) [78] and tetraheptyl ammonium (THA^+) [88] in NiPS_3 . These electrochemical intercalations have demonstrated dramatic tuning of magnetic properties in NiPS_3 [78,88].

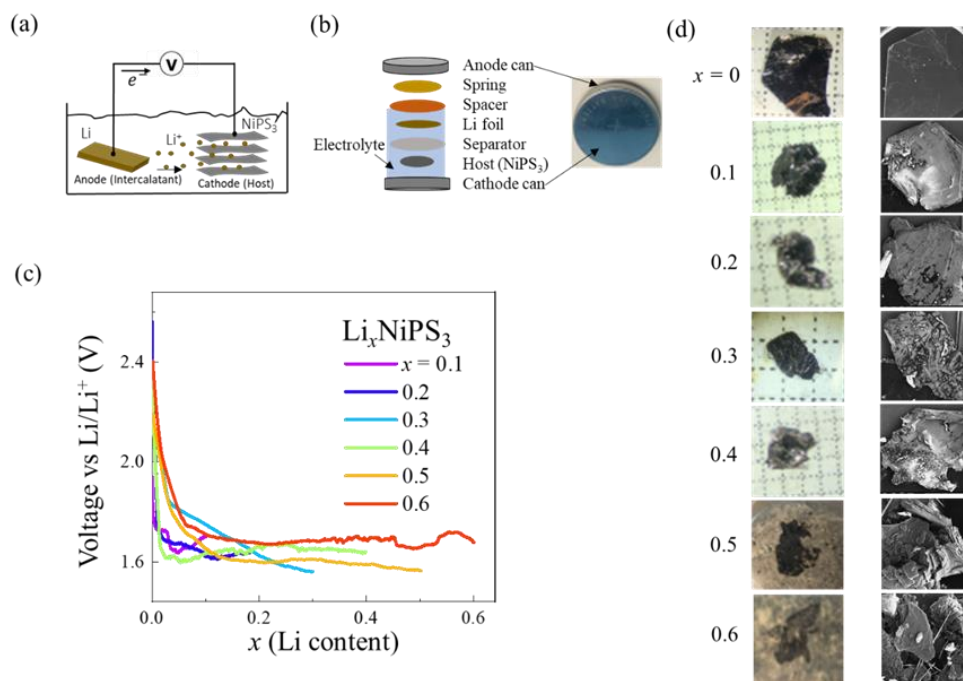


Figure 7.1: (a) Conceptual schematic of electrochemical intercalation process. (b) Schematic of a coin cell used for electrochemical intercalation (Left image). Optical image of an electrochemical coin cell used for intercalation (Right image). (c) Discharge curves showing cell voltage (voltage vs Li/Li^+) as a function of Li content (x) for Li_xNiPS_3 ($0.1 \leq x \leq 0.6$) single crystals. (d) Optical microscope (Left panel) and scanning electron microscope (SEM) (Right panel) images of the pristine and intercalated single crystals.

Given its effectiveness, we used electrochemical intercalation method in this work to insert Li into NiPS₃ single crystals. Li intercalation in NiPS₃ has already been performed using electrochemical [177–179] and wet chemical [89] techniques, on which enhanced conductivity and reflectivity, potential use as battery cathodes, etc., were observed. While these pioneer studies have demonstrated successful Li intercalation in NiPS₃, the effect of intercalated Li on the magnetic properties is not clear. In this work, we performed extensive Li intercalation studies on NiPS₃ to investigate the systematic variation of magnetism with Li content. Figure 7.1(a) shows the conceptual schematic of electrochemical intercalation process and Figure 7.1(b) shows the actual experimental setup. The setup consists of a two-electrode system, where the host NiPS₃ single crystal and a Li metal were fixed on cathode (working electrode) and anode (counter and reference electrode), respectively. Both electrodes were immersed in an electrolyte containing a solution of Lithium bis-trifluoromethanesulfonimide (LiTFSI) salt in Dimethoxyethane (DME) and Dioxolane (DOL) (1:1 ratio) solvents. Compared to wet chemical method, electrochemical intercalation uses electrical force to facilitate the intercalation process through externally applied current or potential, therefore it is more controllable as described above. In our experiment, Li intercalation was driven by discharging the cell with a constant current of 20 μ A. Similar current was used to intercalate TBA⁺ ions [78]. During the discharging process, lithium is oxidized into lithium cation (Li⁺) and electron at anode. The electron flows from anode to cathode through the external circuit. For each such electron, a Li⁺ cation is intercalated to host NiPS₃ through the electrolyte to maintain the charge neutrality, as shown in Figure 7.1(a). Thus, the Li concentration in the host can be controlled by controlling the total amount of charge (i.e., integral current over time) transferred from anode (Li) to cathode (NiPS₃ host). The degree of lithiation x (number of Li atoms intercalated per mole of NiPS₃) used in this

paper was calculated using, $x = (ItM)/(eN_A m)$, where I , t , M , e , N_A , and m are discharge current, time of intercalation, molar mass of NiPS₃, electron charge, Avogadro's constant, and mass of the host NiPS₃ single crystal, respectively. The variation of electrochemical potential with respect to Li/Li⁺ during the intercalation was recorded, and the resulting discharge curves showing cell voltage (voltage vs Li/Li⁺) as a function of Li content (x) in Li _{x} NiPS₃ ($0.1 \leq x \leq 0.6$) single crystals are presented in Figure 7.1(c). The initial cell voltage (≈ 2 - 2.5 V) for all the samples is close to the previous Li intercalations [177–179]. However, the discharge curves obtained for our samples are different than the reported results [177,178]: In earlier studies, the shape of discharge curve for Li _{x} NiPS₃ is found to be dependent on the applied current and electrolyte [178,179]. Such discrepancy may be attributed to different current, and the electrolyte used in our experiment.

To minimize possible extrinsic factors, in each intercalation experiment, we used a single piece of NiPS₃ crystal with similar mass and size. The self-diffusion rate of intercalated Li⁺ ions in NiPS₃ is also found to be low (10^{-13} - 10^{-14} cm²s⁻¹), and both homogeneous and inhomogeneous distribution of Li⁺ ions have been predicted for $0 < x < 0.5$ compositions in Li _{x} NiPS₃ [67]. To facilitate efficient Li diffusion and homogeneous intercalation, the coin cells were heated at 50°C throughout the process. We have also been careful to avoid excessive heating of the battery at elevated temperatures. How Li intercalates to host material, such as random distribution in vdw gaps, or form a certain pattern suggested in a previous study [67], are important to gain a deep understanding of the correlation between structure and properties of Li _{x} NiPS₃. Unfortunately, the distribution of Li cannot be probed by the commonly used x-ray-based techniques such as x-ray crystallography and Energy dispersive X-ray Spectroscopy (EDS). Although direct observations of composition homogeneity and Li distributions are not available, as will be discussed below,

we do observe a systematic evolution of the magnetic properties with increasing the nominal Li dopant amount.

After the completion of intercalation, the discharged cells were opened inside a glovebox. The intercalated samples [Figure 7.1(d)] were cleaned to remove the electrolyte from the sample surface. Despite previous studies showing higher amount of Li intercalation (up to $x = 3.6$) in NiPS₃ [179], we found the single crystals broken into small pieces and degraded for relatively low Li concentration ($x \approx 0.5$) as shown in Figure 7.1(d), which has been verified in multiple trials. In our experiments, intercalation of Li up to $x > 0.4$ led a large fraction of the crystal to convert into amorphous form, which was difficult to isolate from the coin cell for further characterizations. The progressive amorphization of NiPS₃ crystals upon Li intercalation is indeed possible [180]. Therefore, we performed magnetization and heat capacity measurements for samples whose crystallinity remains good, i.e., up to $x = 0.4$. Although powdered samples of Li-intercalated NiPS₃ have been found to be highly air sensitive [180], our Li-intercalated single crystals ($x \leq 0.4$) were stable in air and we were able to obtain reproducible results on samples after long time (weeks) of air exposure. Similar sample stability has also been observed in organic-ion intercalated NiPS₃ crystals [78].

The quality of the Li-intercalated crystals is checked by XRD. Unlike the recent organic-ion intercalation study which reports completely different XRD spectra from the pristine NiPS₃ [78,88], in our Li-intercalated samples the sharp (00L) XRD peaks corresponding to pristine NiPS₃ are probed in $x = 0.1 - 0.4$ samples, but greatly suppressed in the $x = 0.4$ sample and eventually barely observable for $x = 0.5$ and 0.6 . This suggests the retention of the host lattice for $x \leq 0.4$ without the formation of any hybrid superlattice seen in organic-ion intercalation [78]. Tiny additional peaks were detected in $x = 0.3$ and 0.4 as denoted by asterisk in Figure 7.2(a),

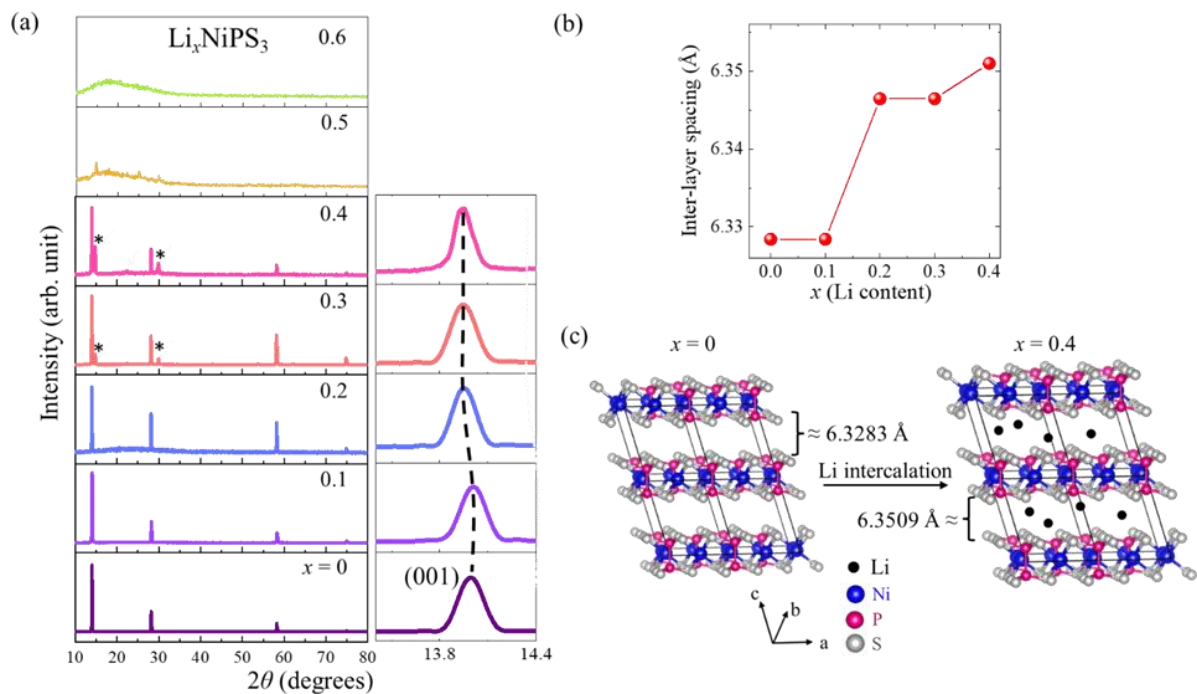


Figure 7.2: (a) Single-crystal x-ray-diffraction pattern of Li_xNiPS_3 ($0 \leq x \leq 0.6$) showing the (00L) reflections. Right panels show (001) diffraction peak. (b) Evolution of inter-layer distance with Li content (x). (c) Schematic of the expanding inter-layer spacing upon Li intercalation.

likely due to the formation of Li_3PS_4 due to the partial degradation at the sample edges [181]. Such degradation eventually resulted in complete destruction upon increasing the Li concentration beyond $x = 0.4$. Furthermore, our XRD results also confirm the successful Li intercalation. The (00L) peaks display systematic low angle shift with increasing Li amount up to $x = 0.4$, indicating increased inter-layer spacing with Li intercalation as summarized in Figure 7.2(b). Such expansion of inter-layer spacing is expected when Li enters the vdW gap, as illustrated in Figure 7.2(c). The small expansion ($\approx 0.36\%$ for $x = 0.4$) is in line with the previous Li intercalations in NiPS_3 [89,177], but in stark contrast to organic-ion intercalations [78,88]. Such a small change in lattice after light Li intercalation has also been observed in other

materials like MoS₂ [182], (V_{1-x}Ti_x)S₂ [183], etc. and can be understood in terms of the occupation of smaller Li⁺ ions in the octahedral sites in the vdW gap of NiPS₃ [89,177,180,184].

The organic-ion intercalations have been found to induce ferrimagnetic (FIM) state at low temperatures in NiPS₃ [78,88]. These FIM states are characterized by hysteresis loops in isothermal field dependence of magnetization [$M(H)$] measurements at low temperature [78,88]. To investigate the effects of Li intercalation, we also measured the $M(H)$ for Li_{*x*}NiPS₃ ($x = 0-0.4$) under in-plane ($H//ab$) (blue color) and out-of-plane ($H\perp ab$) (red color) magnetic fields (Figure 7.3). In this work, we have used the same crystals for XRD, magnetization and heat capacity measurements. For pristine NiPS₃ ($x = 0$), the magnetization shows linear field dependence at low fields for both $H//ab$ and $H\perp ab$ but exhibit a clear upturn under $H//ab$ field of ~ 6 T at $T = 2$ K Figure 7.3(a). Such a metamagnetic transition under an in-plane field in NiPS₃ has recently been attributed to a spin flop (SF) transition [64], which has been verified by other experiments such as nuclear magnetic resonance (NMR) [185] and photoluminescence [186]. This SF transition under $H//ab$ agrees well with the nearly in-plane orientation for Ni moments [31]. With the introduction of Li, the SF transition becomes less apparent, which is consistent with the highly sensitive nature of SF transition towards doping in Mn-substituted NiPS₃ [64]. The modification of SF behavior is accompanied by nonlinear $M(H)$ at low fields under both $H//ab$ and $H\perp ab$ Figure 7.3(a). Such nonlinearity has been ascribed to the development of the local ferromagnetic component due to moment canting in Mn-substituted NiPS₃ [64], but the lack of magnetic hysteresis suggests AFM ground state [64]. In Li-intercalated NiPS₃ studied in this work, however, the low field magnetization exhibits clear hysteresis loops Figure 7.3(b). These hysteresis loops are reminiscent of that of the organic-ion intercalated NiPS₃ [78,88], suggesting the emergence of FIM ordering at low temperature after Li intercalation. After removing the

linear magnetization background, we can clearly see the moment saturation for Li-intercalated samples, as shown in Figure 7.3(c). Such hysteresis and moment saturation may also arise due to ferromagnetism (FM), but the magnetization values in the order of $10^{-3}\mu_B$ per Ni atom similar to organic-ion intercalation [78] is much lower than the saturation moment of Ni^{2+} ($\approx 2.82 \mu_B$), implying FIM rather than FM ordering at low temperature [78]. Interestingly, the coercive fields (H_c) for hysteresis loops and saturated moment (μ_{sat}) show non-monotonic evolution with increasing x : both μ_{sat} and H_c are enhanced until they suddenly drop for $x = 0.4$ sample [Figure 7.3(d)], which will be discussed later.

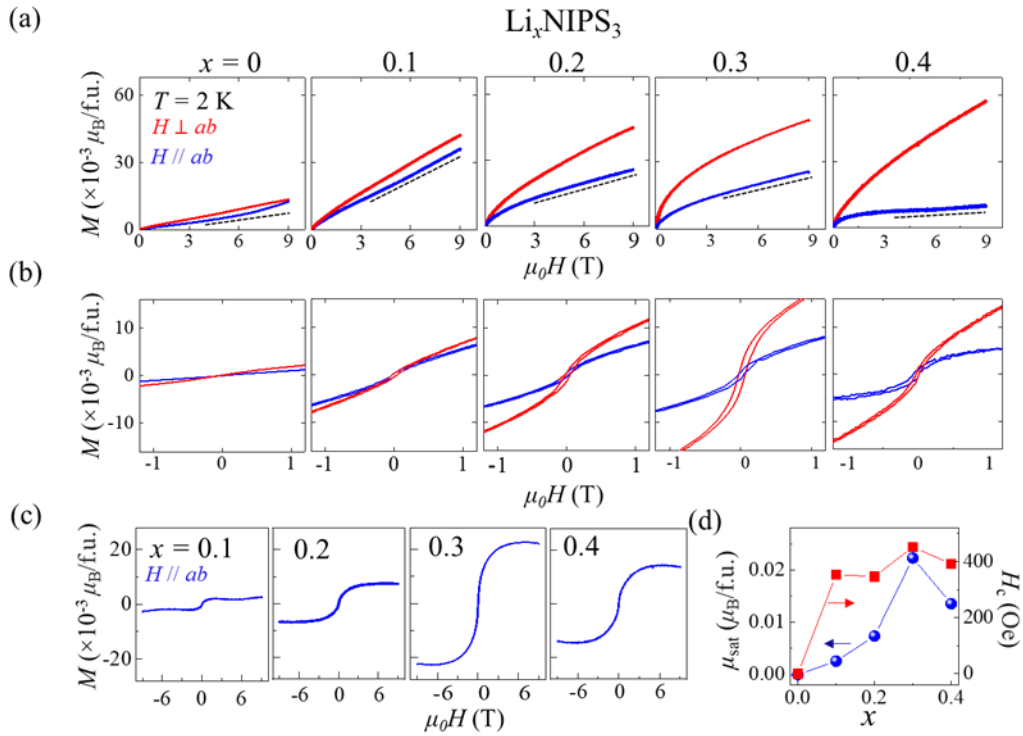


Figure 7.3: (a) Field dependence of magnetization of Li_xNiPS_3 ($0 \leq x \leq 0.4$) at $T = 2 \text{ K}$ for out-of-plane ($H \perp ab$, red) and in-plane ($H \parallel ab$, blue) fields. The dashed lines are guide to eye. (b) Low field magnetization of Li_xNiPS_3 ($0 \leq x \leq 0.4$) at $T = 2 \text{ K}$. (c) Field dependence of magnetization of Li_xNiPS_3 ($0.1 \leq x \leq 0.4$) at $T = 2 \text{ K}$ for in-plane fields after subtraction of linear magnetization background. (d) Evolution of saturation moment (μ_{sat}) (left axis) and coercive fields (H_c) (right axis) with Li content x .

The FIM state is further supported by the temperature dependence of susceptibility (χ) measurement presented in Figure 7.4. For pristine NiPS₃, where Ni moments align within the basal plane [31], the in-plane susceptibility ($\chi_{//}$) drops rapidly while the out-of-plane susceptibility (χ_{\perp}) shows weak T -dependence below $T_N \approx 155$ K, as shown in Figure 7.4(a). T_N is roughly unchanged in Li-intercalated samples ($x = 0.1-0.4$), which is better illustrated in Figure 7.4(b) which displays the zoom in of the data near the magnetic transition temperature. The observed magnetic anisotropy also indicates roughly unchanged magnetic easy axis upon Li intercalation. This is consistent with an earlier NMR study of Li _{x} NiPS₃ [187], which propose the retention of the host's AFM ordering up to $x = 0.5$. The unaltered T_N with Li intercalation has also been observed in the specific heat measurements presented in Figure 7.5(a), which agrees well with the previous Li intercalation study carried out by immersing samples in *n*-butyllithium solution [89]. Such robustness of the ordering temperature can be understood in terms of the exchange interaction mechanism in pristine NiPS₃. The magnetic exchange in NiPS₃ is mainly dominated by the intra-layer interaction, where the inter-layer interaction is found to be negligible in earlier studies because of the large vdW gap [38,40,41]. A relatively large inter-layer ferromagnetic interaction has been revealed by neutron spectroscopy measurement in NiPS₃ single crystal than other MPX₃ compounds [188], but it is still significantly weaker than the dominant intra-layer third neighbor exchange J_3 . So, the overall magnetic interaction is still governed by the intra-layer exchanges. As discussed earlier, Li⁺ ions occupy positions in the vdW gap, so the modification of the intra-layer exchange interaction seems less likely to happen. In addition, the intra-layer magnetic interactions are superexchange in nature mediated through S atoms [38,40,41], which are weakly dependent on the Ni-Ni distance [143]. Though inter-layer intercalations have tiny effects on the in-plane lattice [177,203,204], the superexchange remains

intact even if the in-plane lattice parameters are slightly modified, leading to essentially unchanged magnetic transition temperature.

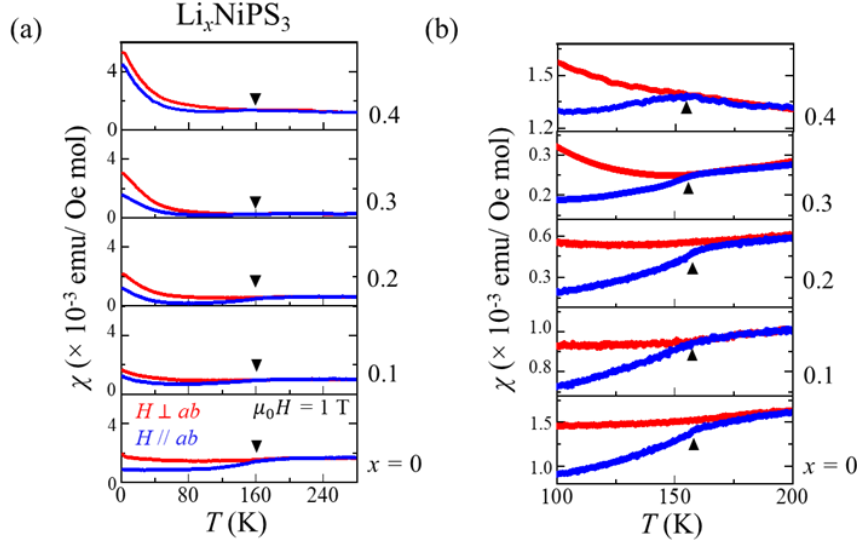


Figure 7.4: (a) Temperature dependence of out-of-plane ($H \perp ab$, red) and in-plane ($H \parallel ab$, blue) molar susceptibility (χ) of Li_xNiPS_3 ($0 \leq x \leq 0.4$) samples. The black triangles denote T_N . (b) Temperature dependence of out-of-plane ($H \perp ab$, red) and in-plane ($H \parallel ab$, blue) molar susceptibility χ of Li_xNiPS_3 ($0 \leq x \leq 0.4$) samples in the temperature range 100-200 K.

The organic-ion intercalated NiPS_3 feature no obvious PM-AFM transition in the vicinity of $T_N \approx 155$ K for pristine NiPS_3 [78,88]. Instead, both χ_{\parallel} and χ_{\perp} undergo sudden increase below $T \approx 100$ K, which together with the magnetic hysteresis loops have been attributed to FIM ordering at low temperature [78,88]. Similar rapid increase in the susceptibility is also seen at $T < 80$ K in our Li-intercalated samples, which becomes more pronounced with increasing degree of lithiation [Figure 7.4(a)]. Such low temperature anomaly in $M(T)$ is also observed in specific heat measurements. As shown in Figure 7.5(b), the low temperature specific heat for pristine NiPS_3 ($x = 0$) does not display any anomaly and follows conventional $C(T) = \gamma T + \beta T^3$, where γT and βT^3 are electronic and phonon specific heat, respectively. Upon increasing Li content (x), the

low temperature specific heat starts to deviate from linear C/T vs T^2 behavior, which is in line with the upturn in $M(T)$ measurements and may be attributed to magnetic contributions.

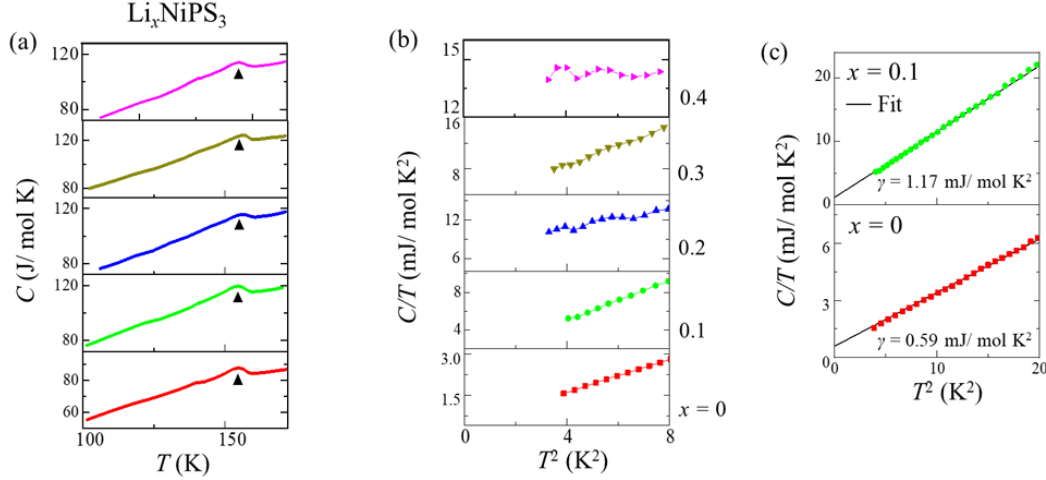


Figure 7.5: (a) Temperature dependence of specific heat capacity of Li_xNiPS_3 ($0 \leq x \leq 0.4$) samples. The black triangles denote T_N . (b) Low temperature specific heat capacity of Li_xNiPS_3 ($0 \leq x \leq 0.4$) samples. (c) C/T vs T^2 data plotted for $x = 0$ and 0.1 samples with linear fits (Black solid lines) to $C/T = \gamma + \beta T^2$.

In an earlier study on chemically intercalated Li_xNiPS_3 using *n*-butyllithium solution, the magnetic susceptibility has been found to reduce with Li intercalation [89]. Such behavior has been ascribed to an impurity phase with substantially lower magnetization [89]. In our electrochemically intercalated Li_xNiPS_3 , however, the value of low temperature molar susceptibility enhances systematically [Figure 7.4(a)], implying minimized impurity phases which is also consistent with the previous NMR study [187] which demonstrates the persistence of host NiPS_3 phase for $x \leq 0.5$. Thus, the magnetic hysteresis in $M(H)$, anomalies in $M(T)$ and $C(T)$ can be attributed to the emergence of FIM correlation at low temperature.

Recently, similar suppression of AFM correlations and the rise of a FM state at low temperature was observed in Co-doped NiPS_3 nanosheets, which is manifested by the magnetic hysteresis loops and remarkable increase of the magnetic susceptibility [65]. Such FM ordering

has been ascribed to the presence of S vacancies in the lattice [65]. However, S vacancies may not be responsible for the emergence of FIM state in our Li-intercalated NiPS₃ because it should affect superexchange interactions and eventually change T_N in a way similar to that of Co-doped NiPS₃ [65], which is inconsistent with the unchanged T_N in our samples (Figure 7.4). Instead, the development of FIM state can be explained based on the magnetic structure of pristine NiPS₃. As shown in Figure 7.6, within the Ni layer, the Ni moments exhibit a zig-zag AFM order consisting of bi-collinear ferromagnetic (FM) chains along the a -axis [31,40,41], resulting in the intra-chain FM and inter-chain AFM correlations. Upon Li intercalation, the total magnetic moments of these two antiferromagnetically coupled zigzag chains $\mu[\text{Ni}(\uparrow)]$ and $\mu[\text{Ni}(\downarrow)]$ become unequal, giving rise to a net magnetic moment (Figure 7.6). The emergence of the net in-plane magnetic moment is supported by the monotonic increase of the μ_{sat} and H_c up to $x = 0.3$ when field is applied within the plane, as shown in Figures 7.3(c) and (d). The $x = 0.4$ sample, however, exhibits an abnormal decrease in both μ_{sat} and H_c . This can be understood in terms of the development of the non-magnetic impurity phase as stated above [Figure 7.2(a)], or the enhancement of superexchange upon carrier doping as will be discussed below. The Li₃PS₄ impurity phase may not play a significant role in mediating the evolution of magnetic properties, because Li₃PS₄ does not display magnetic order nor strong magnetism. Considering the host material is magnetic, Li₃PS₄ should not create a strong magnetic signal to significantly impact the measured magnetic properties. Our susceptibility measurements (Fig. 7.4) reveal systematically increased magnetic susceptibility. Therefore, Li₃PS₄ impurity phase might affect the measured properties via reducing the volume fraction of the Li_{*x*}NiPS₃ in the entire sample, which leads to the reduced coercive field and saturation moment. In addition, the reduction of μ_{sat} and H_c may also be caused by the re-emergence of AFM ordering due to the enhancement of superexchange

interaction up on carrier doping as seen in organic-ion intercalated NiPS₃ [88]. This is also supported by our specific heat measurements. The deviation of the low temperature specific heat from the $C/T \propto T^2$ dependence [Figure 7.5(b)] implies magnetic contributions, which is less likely to be caused by nonmagnetic Li₃PS₄.

A few mechanisms have been proposed for such uncompensation between two oppositely aligned Ni chains. A previous study of organic-ion intercalation in NiPS₃ [78] has demonstrated the reduction of high spin Ni²⁺ in octahedral (*O_h*) sites to low spin Ni⁰ state followed by its displacement to tetrahedral (*T_d*) sites. Such reductive displacement of Ni²⁺ ions has been ascribed to the development of FIM component at low temperature. Similar displacement of Ni²⁺ ions from *O_h* to *T_d* sites has been shown in earlier *x*-ray absorption [180] and Raman [184] studies of Li-intercalated NiPS₃. Therefore, a similar scenario for FIM state can also be expected in our Li-intercalated samples.

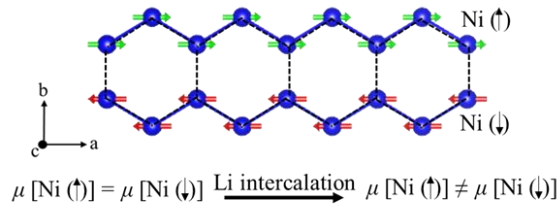


Figure 7.6: In-plane magnetic structure of pristine NiPS₃ showing two antiferromagnetically aligned Ni chains. The total magnetic moments of these chains become unequal upon Li intercalation.

Another organic-ion intercalation study suggests a different mechanism based on the Stoner effect [88]. At an appropriate electron doping level, the density of states (DOS) at Fermi level increases and eventually triggers the inter-chain Stoner splitting of the itinerant electrons. This can result in the higher electron concentration in one Ni chain and lead to net magnetic moment. A previous Raman study of Li_xNiPS₃ has demonstrated electron doping to the host

lattice [184] which is necessary to induce the Stoner effect [88]. In fact, charge carrier doping is found to be more significant in case of Li intercalation than the organic-ion intercalation [78,184]. Therefore, the Stoner effect may play a role in Li-intercalated NiPS₃, which is supported by the enhanced Sommerfeld coefficient (γ) in specific heat measurements [Figure 7.5(c)]. Enhanced γ in specific heat measurements suggests increased DOS near the Fermi level DOS(E_F), which is required to induce the Stoner effect. We did not observe conductivity enhancement, probably because DOS(E_F) is still too low, or due to the presence of other mechanisms such as electronic correlation effects. Furthermore, the net magnetic moment is found to disappear at higher electron doping concentration because of enhanced superexchange between two adjacent Ni chains leading to the revival of AFM ordering [88]. Similar suppression of FIM ordering and rise in the AFM interaction could be the reason behind the reduction of both μ_{sat} and H_c in the highest Li-intercalated sample we have measured i.e., $x = 0.4$ [Figure 7.3(d)]. Although further experimental and theoretical efforts are needed to clarify the non-monotonic evolution of μ_{sat} and H_c , the observed modulation of the magnetic states highlights the ability of intercalation in tuning the magnetism of MPX_3 materials.

7.4 Conclusion

In conclusion, we have demonstrated successful Li intercalation in NiPS₃ single crystals using electrochemical technique and investigated their magnetic properties through magnetization and specific heat measurements. Our study reveals the existence of ferrimagnetism at low temperature resulting from the uncompensated magnetic moments in an intercalated AFM system. Such tuning of the magnetic properties suggests that intercalation can be a novel route to control magnetism in MPX_3 , in addition to the traditional substitution technique.

Chapter 7: Conclusion and Outlook

In this dissertation, we have investigated the magnetic properties of MPX_3 family in different aspects including crystal growth, elemental characterization, structure determination, and magnetism. This dissertation has mainly focused on tuning magnetic properties in MPX_3 materials through various strategies such as substitution of M and X , and interlayer intercalation. Their magnetic properties have been found to be efficiently tunable with these techniques.

We started with single crystal synthesis of MPX_3 compounds using CVT method. We successfully synthesized several metals- and chalcogen-substituted MPX_3 materials such as $Ni_{1-x}Mn_xPS_3$ ($0 \leq x \leq 1$), $Ni_{1-x}Cr_xPS_3$ ($0 \leq x \leq 0.09$), $Fe_{1-x}Mn_xPSe_3$ ($0 \leq x \leq 1$), $MnPS_{3-x}Se_x$ ($0 \leq x \leq 3$), $FePS_{3-x}Se_x$ ($0 \leq x \leq 3$), and $NiPS_{3-x}Se_x$ ($0 \leq x \leq 1.3$). The elemental composition and crystal structure of these compounds were characterized using EDS and XRD, respectively. In addition, the successful metal and chalcogen substitutions were also confirmed using these techniques.

MPX_3 exhibits diverse AFM ordering, in which the transition metal ions M carry localized moments in a layered honeycomb lattice. Their magnetic exchange and anisotropy are strongly dependent on the choice of M , so substituting M can modify their magnetic properties. In $MnPS_3$, the spin-flop (SF) transition has been found to be highly sensitive to Ni substitution. The SF field is significantly suppressed (almost by half) by replacing just 5% Ni for Mn. This is likely attributed to the modification of magnetic anisotropy upon Ni-Mn substitution, which could arise due to large difference in single-ion anisotropies for Mn^{2+} and Ni^{2+} ions. Recently, metal substitution has been predicted to induce AFM to FM transition in MPX_3 . However, traditional isovalent metal substitutions are unable to achieve FM phases. Given such AFM to FM transition has been widely seen in Cr-based layered magnets, we studied previously unexplored Cr-substituted $NiPS_3$. Our work reveals field-induced transition from AFM to FM

state in light ($\approx 9\%$) Cr-substituted NiPS₃. Such behavior can be ascribed to weakening of magnetic anisotropy upon Cr substitution, which will facilitate polarization of moments under magnetic field, as commonly seen in Cr-based layered magnetic materials.

Compared to M substitutions, replacing X ions would provide a relatively clean approach without touching M ions to modulate magnetism. This dissertation has also demonstrated the effective control of magnetic exchange and anisotropy through non-magnetic chalcogen substitution in MPX_3 . Here, we found distinct doping dependencies of the magnetic ordering temperature (T_N) in MnPS_{3-x}Se_x and NiPS_{3-x}Se_x ($0 \leq x \leq 3$). This is likely due to difference in their dominant exchange interactions i.e., direct $M-M$ interaction in MnPS₃ whereas superexchange $M-X-M$ interaction in NiPS₃. Substituting Se for S suppresses direct $M-M$ interaction leading to reduction in T_N in MnPS₃ while it enhances superexchange $M-X-M$ interaction resulting in rise of T_N in NiPS₃. Furthermore, the magnetic axis in MnPS_{3-x}Se_x is switched from out of plane to in-plane direction above $x = 0.7$ but remains intact up to $x = 1.3$ in NiPS_{3-x}Se_x. The situation is different for FePS_{3-x}Se_x, in which (1) the T_N exhibits non-monotonic evolution and (2) the magnetic easy axis remains unchanged with S-Se substitution, which are different than that of MnPS_{3-x}Se_x and NiPS_{3-x}Se_x. The non-monotonic variation of T_N in FePS_{3-x}Se_x could arise due to its more complex exchange mechanism than that of Mn and Ni systems. The lack of modification of easy axis could be attributed to highly anisotropic Ising-type magnetism for parent compounds FePS₃ and FePSe₃, which have strong tendency to maintain their magnetic order. Moreover, we found that the magnetic anisotropy in FePSe₃ can be modified with metal substitution though not as efficiently as in Ni and Mn systems. Substituting more than 90% of Mn for Fe is required to switch easy axis from out of plane towards in-plane direction in FePSe₃.

In addition to M and X substitutions within the layer, the vdW-type structure allows for another doping strategy i.e., intercalation of guest ions into inter-layer spacing. Here, we performed electrochemical intercalation of Li into NiPS_3 . We found the emergence of ferrimagnetism in Li-intercalated NiPS_3 , which is characterized by hysteresis loops in isothermal field dependence of magnetization at low temperature. Such ferrimagnetic state could arise from uncompensated moments between AFM Ni chains due to Li intercalation.

Our work provides various tunable platforms that could be useful to understand low-dimensional magnetism and develop magnetic materials-based nanodevices for future spintronics applications. In addition to bulk AFM properties in MPX_3 , recent studies have demonstrated the persistence of AFM ordering in atomically thin limit. So far, only FePS_3 and MnPSe_3 have been found to exhibit magnetic ordering up to monolayer limit. This has been attributed to the robust Ising-type and XY -type antiferromagnetism for FePS_3 and MnPSe_3 respectively, which can withstand the strong thermal fluctuations in monolayer limit. The studies of 2D magnetism in MPX_3 have been limited to a few pristine compounds. This dissertation provides an opportunity to extend the investigation of 2D magnetism in doped (substituted and intercalated) systems. Such doped compounds offer suitable material systems to explore tunable magnetism in low dimension. This will also help to clarify the evolution of magnetism in 2D limit and broaden their scope for potential applications in future technology.

References

- [1] K. S. Novoselov, A. K. Geim, S. V. Morozov, D. Jiang, Y. Zhang, S. V. Dubonos, I. V. Grigorieva, and A. A. Firsov, *Electric Field Effect in Atomically Thin Carbon Films*, *Science* **306**, 666 (2004).
- [2] W. Han, R. K. Kawakami, M. Gmitra, and J. Fabian, *Graphene Spintronics*, *Nature Nanotech* **9**, 10 (2014).
- [3] B. Li, T. Xing, M. Zhong, L. Huang, N. Lei, J. Zhang, J. Li, and Z. Wei, *A Two-Dimensional Fe-Doped SnS₂ Magnetic Semiconductor*, *Nature Communications* **8**, 1 (2017).
- [4] Z. Guguchia et al., *Magnetism in Semiconducting Molybdenum Dichalcogenides*, *Science Advances* **4**, eaat3672 (2018).
- [5] K.-T. Ko et al., *RKKY Ferromagnetism with Ising-Like Spin States in Intercalated Fe_{1/4}TaS₂*, *Phys. Rev. Lett.* **107**, 247201 (2011).
- [6] B. Huang et al., *Layer-Dependent Ferromagnetism in a van Der Waals Crystal down to the Monolayer Limit*, *Nature* **546**, 7657 (2017).
- [7] C. Gong et al., *Discovery of Intrinsic Ferromagnetism in Two-Dimensional van Der Waals Crystals*, *Nature* **546**, 265 (2017).
- [8] Z. Fei et al., *Two-Dimensional Itinerant Ferromagnetism in Atomically Thin Fe₃GeTe₂*, *Nature Materials* **17**, 9 (2018).
- [9] X. Cai et al., *Atomically Thin CrCl₃: An In-Plane Layered Antiferromagnetic Insulator*, *Nano Lett.* **19**, 3993 (2019).

- [10] G. Long, H. Henck, M. Gibertini, D. Dumcenco, Z. Wang, T. Taniguchi, K. Watanabe, E. Giannini, and A. F. Morpurgo, *Persistence of Magnetism in Atomically Thin MnPS₃ Crystals*, Nano Lett. **20**, 2452 (2020).
- [11] L. Kang et al., *Phase-Controllable Growth of Ultrathin 2D Magnetic FeTe Crystals*, Nature Communications **11**, 1 (2020).
- [12] S. Albarakati et al., *Antisymmetric Magnetoresistance in van Der Waals Fe₃GeTe₂/Graphite/Fe₃GeTe₂ Trilayer Heterostructures*, Science Advances **5**, eaaw0409 (2019).
- [13] S. Jiang, L. Li, Z. Wang, K. F. Mak, and J. Shan, *Controlling Magnetism in 2D CrI₃ by Electrostatic Doping*, Nature Nanotechnology **13**, 7 (2018).
- [14] Z. Wang et al., *Electric-Field Control of Magnetism in a Few-Layered van Der Waals Ferromagnetic Semiconductor*, Nature Nanotechnology **13**, 7 (2018).
- [15] B. Huang et al., *Electrical Control of 2D Magnetism in Bilayer CrI₃*, Nature Nanotechnology **13**, 7 (2018).
- [16] Y. Deng et al., *Gate-Tunable Room-Temperature Ferromagnetism in Two-Dimensional Fe₃GeTe₂*, Nature **563**, 7729 (2018).
- [17] T. Song et al., *Giant Tunneling Magnetoresistance in Spin-Filter van Der Waals Heterostructures*, Science **360**, 1214 (2018).
- [18] Y. Wu et al., *Néel-Type Skyrmion in WTe₂/Fe₃GeTe₂ van Der Waals Heterostructure*, Nature Communications **11**, 1 (2020).
- [19] D. R. Klein et al., *Probing Magnetism in 2D van Der Waals Crystalline Insulators via Electron Tunneling*, Science **360**, 1218 (2018).

- [20] J. Shang, X. Tang, X. Tan, A. Du, T. Liao, S. C. Smith, Y. Gu, C. Li, and L. Kou, *Stacking-Dependent Interlayer Magnetic Coupling in 2D CrI₃/CrGeTe₃ Nanostructures for Spintronics*, ACS Appl. Nano Mater. **3**, 1282 (2020).
- [21] D. Zhong et al., *Van Der Waals Engineering of Ferromagnetic Semiconductor Heterostructures for Spin and Valleytronics*, Science Advances **3**, e1603113 (2017).
- [22] Z. Wang, I. Gutiérrez-Lezama, N. Ubrig, M. Kroner, M. Gibertini, T. Taniguchi, K. Watanabe, A. Imamoğlu, E. Giannini, and A. F. Morpurgo, *Very Large Tunneling Magnetoresistance in Layered Magnetic Semiconductor CrI₃*, Nature Communications **9**, 1 (2018).
- [23] T. Song et al., *Voltage Control of a van Der Waals Spin-Filter Magnetic Tunnel Junction*, Nano Lett. **19**, 915 (2019).
- [24] Y. Wang et al., *Modulation Doping via a Two-Dimensional Atomic Crystalline Acceptor*, Nano Lett. **20**, 8446 (2020).
- [25] K. F. Mak, J. Shan, and D. C. Ralph, *Probing and Controlling Magnetic States in 2D Layered Magnetic Materials*, Nat Rev Phys **1**, 11 (2019).
- [26] S. Wei, X. Liao, C. Wang, J. Li, H. Zhang, Y.-J. Zeng, J. Linghu, H. Jin, and Y. Wei, *Emerging Intrinsic Magnetism in Two-Dimensional Materials: Theory and Applications*, 2D Mater. **8**, 012005 (2020).
- [27] D. Khomskii, *Transition Metal Compounds* (Cambridge University Press, 2014).
- [28] F. Wang et al., *New Frontiers on van Der Waals Layered Metal Phosphorous Trichalcogenides*, Advanced Functional Materials **28**, 1802151 (2018).

- [29] R. Samal, G. Sanyal, B. Chakraborty, and C. S. Rout, *Two-Dimensional Transition Metal Phosphorous Trichalcogenides (MPX₃): A Review on Emerging Trends, Current State and Future Perspectives*, J. Mater. Chem. A **9**, 2560 (2021).
- [30] B. L. Chittari, Y. Park, D. Lee, M. Han, A. H. MacDonald, E. Hwang, and J. Jung, *Electronic and Magnetic Properties of Single-Layer MPX₃ Metal Phosphorous Trichalcogenides*, Phys. Rev. B **94**, 184428 (2016).
- [31] A. R. Wildes, V. Simonet, E. Ressouche, G. J. McIntyre, M. Avdeev, E. Suard, S. A. Kimber, D. Lançon, G. Pepe, and B. Moubaraki, *Magnetic Structure of the Quasi-Two-Dimensional Antiferromagnet NiPS₃*, Physical Review B **92**, 224408 (2015).
- [32] A. R. Wildes, H. M. Rønnow, B. Roessli, M. J. Harris, and K. W. Godfrey, *Static and Dynamic Critical Properties of the Quasi-Two-Dimensional Antiferromagnet MnPS₃*, Phys. Rev. B **74**, 094422 (2006).
- [33] A. R. Wildes, B. Roessli, B. Lebech, and K. W. Godfrey, *Spin Waves and the Critical Behaviour of the Magnetization in MnPS₃*, J. Phys.: Condens. Matter **10**, 6417 (1998).
- [34] A. R. Wildes, V. Simonet, E. Ressouche, R. Ballou, and G. J. McIntyre, *The Magnetic Properties and Structure of the Quasi-Two-Dimensional Antiferromagnet CoPS₃*, J. Phys.: Condens. Matter **29**, 455801 (2017).
- [35] T. Sekine, M. Jouanne, C. Julien, and M. Balkanski, *Light-Scattering Study of Dynamical Behavior of Antiferromagnetic Spins in the Layered Magnetic Semiconductor FePS₃*, Phys. Rev. B **42**, 8382 (1990).
- [36] Y. Takano, N. Arai, A. Arai, Y. Takahashi, K. Takase, and K. Sekizawa, *Magnetic Properties and Specific Heat of MPS₃ (M=Mn, Fe, Zn)*, Journal of Magnetism and Magnetic Materials **272–276**, E593 (2004).

- [37] A. Wiedenmann, J. Rossat-Mignod, A. Louisy, R. Brec, and J. Rouxel, *Neutron Diffraction Study of the Layered Compounds MnPSe₃ and FePSe₃*, Solid State Communications **40**, 1067 (1981).
- [38] G. Le Flem, R. Brec, G. Ouvard, A. Louisy, and P. Segransan, *Magnetic Interactions in the Layer Compounds MPX₃ (M = Mn, Fe, Ni; X = S, Se)*, Journal of Physics and Chemistry of Solids **43**, 455 (1982).
- [39] P. A. Joy and S. Vasudevan, *Magnetism in the Layered Transition-Metal Thiophosphates MPS₃ (M=Mn, Fe, and Ni)*, Phys. Rev. B **46**, 5425 (1992).
- [40] D. Lançon, R. A. Ewings, T. Guidi, F. Formisano, and A. R. Wildes, *Magnetic Exchange Parameters and Anisotropy of the Quasi-Two-Dimensional Antiferromagnet NiPS₃*, Phys. Rev. B **98**, 134414 (2018).
- [41] C. Kim, J. Jeong, P. Park, T. Masuda, S. Asai, S. Itoh, H.-S. Kim, A. Wildes, and J.-G. Park, *Spin Waves in the Two-Dimensional Honeycomb Lattice XXZ-Type van Der Waals Antiferromagnet CoPS₃*, Phys. Rev. B **102**, 184429 (2020).
- [42] J. B. Goodenough, *Theory of the Role of Covalence in the Perovskite-Type Manganites [La,M(II)]MnO₃*, Phys. Rev. **100**, 564 (1955).
- [43] J. Kanamori, *Superexchange Interaction and Symmetry Properties of Electron Orbitals*, Journal of Physics and Chemistry of Solids **10**, 87 (1959).
- [44] D. J. Goossens, A. R. Wildes, C. Ritter, and T. J. Hicks, *Ordering and the Nature of the Spin Flop Phase Transition in MnPS₃*, J. Phys.: Condens. Matter **12**, 1845 (2000).
- [45] D. J. Goossens, *Dipolar Anisotropy in Quasi-2D Honeycomb Antiferromagnet MnPS₃*, Eur. Phys. J. B **78**, 305 (2010).

- [46] D. Lançon, H. C. Walker, E. Ressouche, B. Ouladdiaf, K. C. Rule, G. J. McIntyre, T. J. Hicks, H. M. Rønnow, and A. R. Wildes, *Magnetic Structure and Magnon Dynamics of the Quasi-Two-Dimensional Antiferromagnet FePS₃*, Phys. Rev. B **94**, 214407 (2016).
- [47] K. Kim et al., *Antiferromagnetic Ordering in van Der Waals 2D Magnetic Material MnPS₃ Probed by Raman Spectroscopy*, 2D Mater. **6**, 041001 (2019).
- [48] J.-U. Lee, S. Lee, J. H. Ryoo, S. Kang, T. Y. Kim, P. Kim, C.-H. Park, J.-G. Park, and H. Cheong, *Ising-Type Magnetic Ordering in Atomically Thin FePS₃*, Nano Lett. **16**, 7433 (2016).
- [49] K. Kim, S. Y. Lim, J.-U. Lee, S. Lee, T. Y. Kim, K. Park, G. S. Jeon, C.-H. Park, J.-G. Park, and H. Cheong, *Suppression of Magnetic Ordering in XXZ-Type Antiferromagnetic Monolayer NiPS₃*, Nature Communications **10**, 1 (2019).
- [50] Z. Ni, A. V. Haglund, H. Wang, B. Xu, C. Bernhard, D. G. Mandrus, X. Qian, E. J. Mele, C. L. Kane, and L. Wu, *Imaging the Néel Vector Switching in the Monolayer Antiferromagnet MnPSe₃ with Strain-Controlled Ising Order*, Nat. Nanotechnol. **16**, 7 (2021).
- [51] N. Chandrasekharan and S. Vasudevan, *Dilution of a Layered Antiferromagnet: Magnetism in Mn_xZn_{1-x}PS₃*, Phys. Rev. B **54**, 14903 (1996).
- [52] D. J. Goossens, A. J. Studer, S. J. Kennedy, and T. J. Hicks, *The Impact of Magnetic Dilution on Magnetic Order in MnPS₃*, J. Phys.: Condens. Matter **12**, 4233 (2000).
- [53] A. M. Mulders, J. C. P. Klaasse, D. J. Goossens, J. Chadwick, and T. J. Hicks, *High-Field Magnetization in the Diluted Quasi-Two-Dimensional Heisenberg Antiferromagnet Mn_{1-x}Zn_xPS₃*, J. Phys.: Condens. Matter **14**, 8697 (2002).

- [54] Y. Takano, A. Arai, Y. Takahashi, K. Takase, and K. Sekizawa, *Magnetic Properties and Specific Heat of New Spin Glass Mn_{0.5}Fe_{0.5}PS₃*, *Journal of Applied Physics* **93**, 8197 (2003).
- [55] J. N. Graham, M. J. Coak, S. Son, E. Suard, J.-G. Park, L. Clark, and A. R. Wildes, *Local Nuclear and Magnetic Order in the Two-Dimensional Spin Glass Mn_{0.5}Fe_{0.5}PS₃*, *Phys. Rev. Materials* **4**, 084401 (2020).
- [56] T. Masubuchi, H. Hoya, T. Watanabe, Y. Takahashi, S. Ban, N. Ohkubo, K. Takase, and Y. Takano, *Phase Diagram, Magnetic Properties and Specific Heat of Mn_{1-x}Fe_xPS₃*, *Journal of Alloys and Compounds* **460**, 668 (2008).
- [57] V. Manríquez, P. Barahona, and O. Peña, *Physical Properties of the Cation-Mixed M²⁺PS₃ Phases*, *Materials Research Bulletin* **35**, 1889 (2000).
- [58] D. J. Goossens, S. Brazier-Hollins, D. R. James, W. D. Hutchison, and J. R. Hester, *Magnetic Structure and Glassiness in Fe_{0.5}Ni_{0.5}PS₃*, *Journal of Magnetism and Magnetic Materials* **334**, 82 (2013).
- [59] Y. He, Y.-D. Dai, H. Huang, J. Lin, and Y. Hsia, *The Ordering Distribution of the Metal Ions in the Layered Cation-Mixed Phosphorus Trisulfides Mn_xFe_{1-x}PS₃*, *Journal of Alloys and Compounds* **359**, 41 (2003).
- [60] D. J. Goossens and T. J. Hicks, *The Magnetic Phase Diagram of Mn_xZn_{1-x}PS₃*, *J. Phys.: Condens. Matter* **10**, 7643 (1998).
- [61] A. Bhutani, J. L. Zuo, R. D. McAuliffe, C. R. dela Cruz, and D. P. Shoemaker, *Strong Anisotropy in the Mixed Antiferromagnetic System Mn_{1-x}Fe_xPSe₃*, *Phys. Rev. Materials* **4**, 034411 (2020).

- [62] Y. Shemerliuk, Y. Zhou, Z. Yang, G. Cao, A. U. B. Wolter, B. Büchner, and S. Aswartham, *Tuning Magnetic and Transport Properties in Quasi-2D $(\text{Mn}_{1-x}\text{Ni}_x)_2\text{P}_2\text{S}_6$ Single Crystals*, *Electronic Materials* **2**, 3 (2021).
- [63] S. Selzer, Y. Shemerliuk, M.-I. Sturza, A. U. B. Wolter, B. Büchner, and S. Aswartham, *Crystal Growth and Anisotropic Magnetic Properties of Quasi-Two-Dimensional $(\text{Fe}_{1-x}\text{Ni}_x)_2\text{P}_2\text{S}_6$* , *Phys. Rev. Materials* **5**, 073401 (2021).
- [64] R. Basnet, A. Wegner, K. Pandey, S. Storment, and J. Hu, *Highly Sensitive Spin-Flop Transition in Antiferromagnetic van Der Waals Material MPS_3 ($M = \text{Ni}$ and Mn)*, *Phys. Rev. Materials* **5**, 064413 (2021).
- [65] F. Wang et al., *Defect-Mediated Ferromagnetism in Correlated Two-Dimensional Transition Metal Phosphorus Trisulfides*, *Science Advances* **7**, eabj4086 (n.d.).
- [66] S. Lee, J. Park, Y. Choi, K. Raju, W.-T. Chen, R. Sankar, and K.-Y. Choi, *Chemical Tuning of Magnetic Anisotropy and Correlations in $\text{Ni}_{1-x}\text{Fe}_x\text{PS}_3$* , *Phys. Rev. B* **104**, 174412 (2021).
- [67] C.-K. Tian, C. Wang, W. Ji, J.-C. Wang, T.-L. Xia, L. Wang, J.-J. Liu, H.-X. Zhang, and P. Cheng, *Domain Wall Pinning and Hard Magnetic Phase in Co-Doped Bulk Single Crystalline Fe_3GeTe_2* , *Phys. Rev. B* **99**, 184428 (2019).
- [68] X. Hu, D.-X. Yao, and K. Cao, *$(\text{Fe}_{1-x}\text{Ni}_x)_5\text{GeTe}_2$: An Antiferromagnetic Triangular Ising Lattice with Itinerant Magnetism*, *Phys. Rev. B* **106**, 224423 (2022).
- [69] C. Tian, F. Pan, S. Xu, K. Ai, T. Xia, and P. Cheng, *Tunable Magnetic Properties in van Der Waals Crystals $(\text{Fe}_{1-x}\text{Co}_x)_5\text{GeTe}_2$* , *Appl. Phys. Lett.* **116**, 202402 (2020).

- [70] G. Drachuck, Z. Salman, M. W. Masters, V. Taufour, T. N. Lamichhane, Q. Lin, W. E. Straszheim, S. L. Bud'ko, and P. C. Canfield, *Effect of Nickel Substitution on Magnetism in the Layered van Der Waals Ferromagnet Fe₃GeTe₂*, Phys. Rev. B **98**, 144434 (2018).
- [71] S. Pan, Y. Bai, J. Tang, P. Wang, Y. You, G. Xu, and F. Xu, *Growth of High-Quality CrI₃ Single Crystals and Engineering of Its Magnetic Properties via V and Mn Doping*, Journal of Alloys and Compounds **908**, 164573 (2022).
- [72] S. Calder, A. V. Haglund, A. I. Kolesnikov, and D. Mandrus, *Magnetic Exchange Interactions in the van Der Waals Layered Antiferromagnet MnPSe₃*, Phys. Rev. B **103**, 024414 (2021).
- [73] P. Jeevanandam and S. Vasudevan, *Magnetism in MnPSe₃: A Layered 3d⁵ Antiferromagnet with Unusually Large XY Anisotropy*, J. Phys.: Condens. Matter **11**, 3563 (1999).
- [74] R. Basnet, K. M. Kotur, M. Rybak, C. Stephenson, S. Bishop, C. Autieri, M. Birowska, and J. Hu, *Controlling Magnetic Exchange and Anisotropy by Nonmagnetic Ligand Substitution in Layered MPX₃ (M = Ni, Mn; X = S, Se)*, Phys. Rev. Research **4**, 023256 (2022).
- [75] H. Han, H. Lin, W. Gan, Y. Liu, R. Xiao, L. Zhang, Y. Li, C. Zhang, and H. Li, *Emergent Mixed Antiferromagnetic State in MnPS₃(1-x)Se_{3x}*, Appl. Phys. Lett. **122**, 033101 (2023).
- [76] M. Abramchuk, S. Jaszewski, K. R. Metz, G. B. Osterhoudt, Y. Wang, K. S. Burch, and F. Tafti, *Controlling Magnetic and Optical Properties of the van Der Waals Crystal CrCl₃-xBr_x via Mixed Halide Chemistry*, Advanced Materials **30**, 1801325 (2018).
- [77] T. A. Tartaglia et al., *Accessing New Magnetic Regimes by Tuning the Ligand Spin-Orbit Coupling in van Der Waals Magnets*, Science Advances **6**, eabb9379 (n.d.).

- [78] D. Tezze et al., *Tuning the Magnetic Properties of NiPS₃ through Organic-Ion Intercalation*, *Nanoscale* **14**, 1165 (2022).
- [79] M. Mi et al., *Variation between Antiferromagnetism and Ferrimagnetism in NiPS₃ by Electron Doping*, *Advanced Functional Materials* **32**, 2112750 (2022).
- [80] R. Basnet, D. Ford, K. TenBarge, J. Lochala, and J. Hu, *Emergence of Ferrimagnetism in Li-Intercalated NiPS₃*, *J. Phys.: Condens. Matter* **34**, 434002 (2022).
- [81] T. Masubuchi, X. Jin, K. Koyama, Y. Takahashi, K. Takase, Y. Uwatoko, Y. Takano, and K. Sekizawa, *Magnetism and Interlayer Distance of MnPS₃ Controlled by Intercalation and Applying High Pressure*, *AIP Conference Proceedings* **850**, 1279 (2006).
- [82] T. Li et al., *Pressure-Controlled Interlayer Magnetism in Atomically Thin CrI₃*, *Nat. Mater.* **18**, 12 (2019).
- [83] S. Mondal, M. Kannan, M. Das, L. Govindaraj, R. Singha, B. Satpati, S. Arumugam, and P. Mandal, *Effect of Hydrostatic Pressure on Ferromagnetism in Two-Dimensional CrI₃*, *Phys. Rev. B* **99**, 180407 (2019).
- [84] Y. Peng et al., *Controlling Spin Orientation and Metamagnetic Transitions in Anisotropic van Der Waals Antiferromagnet CrPS₄ by Hydrostatic Pressure*, *Advanced Functional Materials* **32**, 2106592 (2022).
- [85] X. Li, X. Wu, and J. Yang, *Half-Metallicity in MnPSe₃ Exfoliated Nanosheet with Carrier Doping*, *J. Am. Chem. Soc.* **136**, 11065 (2014).
- [86] X. Ma et al., *The Intercalation of 1,10-Phenanthroline into Layered NiPS₃ via Iron Dopant Seeding*, *Chemical Communications* **56**, 4603 (2020).
- [87] E. Manova, A. Leautic, I. Mitov, D. Gonbeau, and R. Clement, *The NiPS₃-Cobaltocene Intercalation Compound: A New Ferromagnet*, *Molecular Crystals and Liquid Crystals*

- Science and Technology. Section A. Molecular Crystals and Liquid Crystals **311**, 155 (1998).
- [88] M. Mi et al., *Variation between Antiferromagnetism and Ferrimagnetism in NiPS₃ by Electron Doping*, ArXiv:2112.02544 [Cond-Mat] (2022).
- [89] R. Brec, D. M. Schleich, G. Ouvrard, A. Louisy, and J. Rouxel, *Physical Properties of Lithium Intercalation Compounds of the Layered Transition-Metal Chalcogenophosphites*, Inorg. Chem. **18**, 1814 (1979).
- [90] N. Sheremetyeva, I. Na, A. Saraf, S. M. Griffin, and G. Hautier, *Prediction of Topological Phases in Metastable Ferromagnetic MPX₃ Monolayers*.
- [91] J. Yang, Y. Zhou, Y. Dedkov, and E. Voloshina, *Dirac Fermions in Half-Metallic Ferromagnetic Mixed Cr_{1-x}MxPSe₃ Monolayers*, Advanced Theory and Simulations **3**, 2000228 (2020).
- [92] *Physical Property Measurement System (PPMS) Quantum Design | Quantum Design*, <https://qd-europe.com/at/en/product/physical-property-measurement-system-ppms/>.
- [93] G. Ouvrard, R. Brec, and J. Rouxel, *Structural Determination of Some MPS₃ Layered Phases (M = Mn, Fe, Co, Ni and Cd)*, Materials Research Bulletin **20**, 1181 (1985).
- [94] W. Klingen, G. Eulenberger, and H. Hahn, *About the crystal structures of Fe₂P₂Se₆ and Fe₂P₂S₆*, Zeitschrift für anorganische und allgemeine Chemie **401**, 97 (1973).
- [95] K. Du, X. Wang, Y. Liu, P. Hu, M. I. B. Utama, C. K. Gan, Q. Xiong, and C. Kloc, *Weak Van Der Waals Stacking, Wide-Range Band Gap, and Raman Study on Ultrathin Layers of Metal Phosphorus Trichalcogenides*, ACS Nano **10**, 1738 (2016).
- [96] P. J. S. Foot, T. Katz, S. N. Patel, B. A. Nevett, A. R. Piecny, and A. A. Balchin, *The Structures and Conduction Mechanisms of Lithium-Intercalated and Lithium-Substituted*

- Nickel Phosphorus Trisulphide (NiPS₃), and the Use of the Material as a Secondary Battery Electrode*, Phys. Stat. Sol. (a) **100**, 11 (1987).
- [97] L. Silipigni, L. Schirò, T. Quattrone, V. Grasso, G. Salvato, L. Monsù Scolaro, and G. De Luca, *Dielectric Spectra of Manganese Thiophosphate Intercalated with Sodium Ions*, Journal of Applied Physics **105**, 123703 (2009).
- [98] G. Giunta, V. Grasso, F. Neri, and L. Silipigni, *Electrical Conductivity of Lithium-Intercalated Thiophosphate NiPS₃ Single Crystals*, Phys. Rev. B **50**, 8189 (1994).
- [99] L. Silipigni, C. Calareso, G. M. Curró, F. Neri, V. Grasso, H. Berger, G. Margaritondo, and R. Ponterio, *Effects of Lithium Intercalation on the Electronic Properties of FePS₃ Single Crystals*, Phys. Rev. B **53**, 13928 (1996).
- [100] C.-T. Kuo et al., *Exfoliation and Raman Spectroscopic Fingerprint of Few-Layer NiPS₃ Van Der Waals Crystals*, Scientific Reports **6**, 1 (2016).
- [101] D. H. Luong, T. L. Phan, G. Ghimire, D. L. Duong, and Y. H. Lee, *Revealing Antiferromagnetic Transition of van Der Waals MnPS₃ via Vertical Tunneling Electrical Resistance Measurement*, APL Materials **7**, 081102 (2019).
- [102] S. Lee, K.-Y. Choi, S. Lee, B. H. Park, and J.-G. Park, *Tunneling Transport of Mono- and Few-Layers Magnetic van Der Waals MnPS₃*, APL Materials **4**, 086108 (2016).
- [103] H. Chu, C. J. Roh, J. O. Island, C. Li, S. Lee, J. Chen, J.-G. Park, A. F. Young, J. S. Lee, and D. Hsieh, *Linear Magnetoelectric Phase in Ultrathin MnPS₃ Probed by Optical Second Harmonic Generation*, Phys. Rev. Lett. **124**, 027601 (2020).
- [104] X. Wang et al., *Spin-Induced Linear Polarization of Excitonic Emission in Antiferromagnetic van Der Waals Crystals*, ArXiv:2006.07952 [Cond-Mat] (2020).

- [105] S. N. Neal, H.-S. Kim, K. A. Smith, A. V. Haglund, D. G. Mandrus, H. A. Bechtel, G. L. Carr, K. Haule, D. Vanderbilt, and J. L. Musfeldt, *Near-Field Infrared Spectroscopy of Monolayer MnPS₃*, Phys. Rev. B **100**, 075428 (2019).
- [106] G. Long et al., *Isolation and Characterization of Few-Layer Manganese Thiophosphate*, ACS Nano **11**, 11330 (2017).
- [107] K. C. Rule, G. J. McIntyre, S. J. Kennedy, and T. J. Hicks, *Single-Crystal and Powder Neutron Diffraction Experiments on FePS₃: Search for the Magnetic Structure*, Phys. Rev. B **76**, 134402 (2007).
- [108] S. Y. Kim et al., *Charge-Spin Correlation in van Der Waals Antiferromagnet NiPS₃*, Phys. Rev. Lett. **120**, 136402 (2018).
- [109] H.-S. Kim, K. Haule, and D. Vanderbilt, *Mott Metal-Insulator Transitions in Pressurized Layered Trichalcogenides*, Phys. Rev. Lett. **123**, 236401 (2019).
- [110] Y. Wang et al., *Pressure-Driven Cooperative Spin-Crossover, Large-Volume Collapse, and Semiconductor-to-Metal Transition in Manganese(II) Honeycomb Lattices*, J. Am. Chem. Soc. **138**, 15751 (2016).
- [111] C. R. S. Haines, M. J. Coak, A. R. Wildes, G. I. Lampronti, C. Liu, P. Nahai-Williamson, H. Hamidov, D. Daisenberger, and S. S. Saxena, *Pressure-Induced Electronic and Structural Phase Evolution in the van Der Waals Compound FePS₃*, Phys. Rev. Lett. **121**, 266801 (2018).
- [112] M. Tsurubayashi, K. Kodama, M. Kano, K. Ishigaki, Y. Uwatoko, T. Watanabe, K. Takase, and Y. Takano, *Metal-Insulator Transition in Mott-Insulator FePS₃*, AIP Advances **8**, 101307 (2018).

- [113] M. J. Coak et al., *Tuning Dimensionality in Van-Der-Waals Antiferromagnetic Mott Insulators TMPS₃*, J. Phys.: Condens. Matter **32**, 124003 (2019).
- [114] R. A. Evarestov and A. Kuzmin, *Origin of Pressure-Induced Insulator-to-Metal Transition in the van Der Waals Compound FePS₃ from First-Principles Calculations*, Journal of Computational Chemistry **41**, 1337 (2020).
- [115] X. Ma et al., *Dimensional Crossover Tuned by Pressure in Layered Magnetic NiPS₃*, ArXiv:2009.14051 [Cond-Mat] (2020).
- [116] M. J. Coak, S. Son, D. Daisenberger, H. Hamidov, C. R. S. Haines, P. L. Alireza, A. R. Wildes, C. Liu, S. S. Saxena, and J.-G. Park, *Isostructural Mott Transition in 2D Honeycomb Antiferromagnet V_{0.9}PS₃*, Npj Quantum Materials **4**, 1 (2019).
- [117] Y. Wang et al., *Emergent Superconductivity in an Iron-Based Honeycomb Lattice Initiated by Pressure-Driven Spin-Crossover*, Nature Communications **9**, 1 (2018).
- [118] K. Okuda, K. Kurosawa, S. Saito, M. Honda, Z. Yu, and M. Date, *Magnetic Properties of Layered Compound MnPS₃*, J. Phys. Soc. Jpn. **55**, 4456 (1986).
- [119] A. R. Wildes, D. Lançon, M. K. Chan, F. Weickert, N. Harrison, V. Simonet, M. E. Zhitomirsky, M. V. Gvozdikova, T. Ziman, and H. M. Rønnow, *High Field Magnetization of FePS₃*, Phys. Rev. B **101**, 024415 (2020).
- [120] A. P. Dioguardi, S. Selter, U. Peeck, S. Aswartham, M.-I. Sturza, R. Murugesan, M. S. Eldeeb, L. Hozoi, B. Büchner, and H.-J. Grafe, *Quasi-Two-Dimensional Magnetic Correlations in Ni₂P₂S₆ Probed by P₃₁ NMR*, Phys. Rev. B **102**, 064429 (2020).
- [121] F. B. Anderson and H. B. Callen, *Statistical Mechanics and Field-Induced Phase Transitions of the Heisenberg Antiferromagnet*, Phys. Rev. **136**, A1068 (1964).

- [122] L. J. D. Jongh and A. R. Miedema, *Experiments on Simple Magnetic Model Systems*, Advances in Physics **50**, 947 (2001).
- [123] E. Emmanouilidou, J. Liu, D. Graf, H. Cao, and N. Ni, *Spin-Flop Phase Transition in the Orthorhombic Antiferromagnetic Topological Semimetal $\text{Cu}_{0.95}\text{MnAs}$* , Journal of Magnetism and Magnetic Materials **469**, 570 (2019).
- [124] G. Gitgeatpong et al., *High-Field Magnetization and Magnetic Phase Diagram of $A\text{-Cu}_2\text{V}_2\text{O}_7$* , Phys. Rev. B **95**, 245119 (2017).
- [125] S. M. Wu, W. Zhang, A. KC, P. Borisov, J. E. Pearson, J. S. Jiang, D. Lederman, A. Hoffmann, and A. Bhattacharya, *Antiferromagnetic Spin Seebeck Effect*, Phys. Rev. Lett. **116**, 097204 (2016).
- [126] D. Li, Z. Han, J. G. Zheng, X. L. Wang, D. Y. Geng, J. Li, and Z. D. Zhang, *Spin Canting and Spin-Flop Transition in Antiferromagnetic Cr_2O_3 Nanocrystals*, Journal of Applied Physics **106**, 053913 (2009).
- [127] D. Tobia, E. Winkler, R. D. Zysler, M. Granada, and H. E. Troiani, *Size Dependence of the Magnetic Properties of Antiferromagnetic Cr_2O_3 Nanoparticles*, Phys. Rev. B **78**, 104412 (2008).
- [128] W. Zhang, K. Nadeem, H. Xiao, R. Yang, B. Xu, H. Yang, and X. G. Qiu, *Spin-Flop Transition and Magnetic Phase Diagram in CaCo_2As_2 Revealed by Torque Measurements*, Phys. Rev. B **92**, 144416 (2015).
- [129] Y. Gu, Q. Zhang, C. Le, Y. Li, T. Xiang, and J. Hu, *Ni-Based Transition Metal Trichalcogenide Monolayer: A Strongly Correlated Quadruple-Layer Graphene*, Phys. Rev. B **100**, 165405 (2019).

- [130] A. R. C. McCray, Y. Li, R. Basnet, K. Pandey, J. Hu, D. P. Phelan, X. Ma, A. K. Petford-Long, and C. Phatak, *Thermal Hysteresis and Ordering Behavior of Magnetic Skyrmion Lattices*, *Nano Lett.* **22**, 7804 (2022).
- [131] C. Autieri, G. Cuono, C. Noce, M. Rybak, K. M. Kotur, C. E. Agrapidis, K. Wohlfeld, and M. Birowska, *Limited Ferromagnetic Interactions in Monolayers of MPS3 (M = Mn and Ni)*, *J. Phys. Chem. C* **126**, 6791 (2022).
- [132] Z. Lin et al., *Magnetism and Its Structural Coupling Effects in 2D Ising Ferromagnetic Insulator VI3*, *Nano Lett.* **21**, 9180 (2021).
- [133] A. Bedoya-Pinto, J.-R. Ji, A. K. Pandeya, P. Gargiani, M. Valvidares, P. Sessi, J. M. Taylor, F. Radu, K. Chang, and S. S. P. Parkin, *Intrinsic 2D-XY Ferromagnetism in a van Der Waals Monolayer*, *Science* **374**, 616 (2021).
- [134] D. J. Goossens, D. James, J. Dong, R. E. Whitfield, L. Norén, and R. L. Withers, *Local Order in Layered NiPS3 and Ni0.7Mg0.3PS3*, *J. Phys.: Condens. Matter* **23**, 065401 (2011).
- [135] P. Fuentealba, C. Olea, H. Aguilar-Bolados, N. Audebrand, R. C. de Santana, C. Doerenkamp, H. Eckert, C. J. Magon, and E. Spodine, *Physical Properties of New Ordered Bimetallic Phases M0.25Cd0.75PS3 (M = Zn II, Ni II, Co II, Mn II)*, *Physical Chemistry Chemical Physics* **22**, 8315 (2020).
- [136] F. Bougamha, S. Selter, Y. Shemerliuk, S. Aswartham, A. Benali, B. Büchner, H.-J. Grafe, and A. P. Dioguardi, *31P NMR Investigation of Quasi-Two-Dimensional Magnetic Correlations in T2P2S6 (T=Mn, Ni)*, *Phys. Rev. B* **105**, 024410 (2022).
- [137] S. Selter et al., *Crystal Growth, Exfoliation and Magnetic Properties of Quaternary Quasi-Two-Dimensional CuCrP2S6*, arXiv:2112.02590.

- [138] X. Wang et al., *Electrical and Magnetic Anisotropies in van Der Waals Multiferroic CuCrP2S6*, Nat Commun **14**, 1 (2023).
- [139] Y. Peng et al., *Magnetic Structure and Metamagnetic Transitions in the van Der Waals Antiferromagnet CrPS4*, Advanced Materials **32**, 2001200 (2020).
- [140] M. A. McGuire, G. Clark, S. KC, W. M. Chance, G. E. Jellison, V. R. Cooper, X. Xu, and B. C. Sales, *Magnetic Behavior and Spin-Lattice Coupling in Cleavable van Der Waals Layered CrCl3 Crystals*, Phys. Rev. Mater. **1**, 014001 (2017).
- [141] E. J. Telford et al., *Layered Antiferromagnetism Induces Large Negative Magnetoresistance in the van Der Waals Semiconductor CrSBr*, Advanced Materials **32**, 2003240 (2020).
- [142] J. L. Lado and J. Fernández-Rossier, *On the Origin of Magnetic Anisotropy in Two Dimensional CrI3*, 2D Mater. **4**, 035002 (2017).
- [143] B. Mallesh et al., *Incommensurate Antiferromagnetic Order in Weakly Frustrated Two-Dimensional van Der Waals Insulator CrPSe3*, arXiv:2210.15094.
- [144] C. Payen, H. Mutka, J. L. Soubeyroux, P. Molinié, and P. Colombet, *Static and Dynamic Properties of the Quasi-1D Heisenberg Antiferromagnets AgVP2S6 ($S=1$) and AgCrP2S6 ($S = 3/2$)*, Journal of Magnetism and Magnetic Materials **104–107**, 797 (1992).
- [145] S. Selter, Y. Shemerliuk, B. Büchner, and S. Aswartham, *Crystal Growth of the Quasi-2D Quarternary Compound AgCrP2S6 by Chemical Vapor Transport*, Crystals **11**, 5 (2021).
- [146] G. Ouvrard, R. Fréour, R. Brec, and J. Rouxel, *A Mixed Valence Compound in the Two Dimensional MPS3 Family: V0.78PS3 Structure and Physical Properties*, Materials Research Bulletin **20**, 1053 (1985).

- [147] A. R. Wildes, B. Roessli, B. Lebech, and K. W. Godfrey, *Spin Waves and the Critical Behaviour of the Magnetization in MnPS₃*, *J. Phys.: Condens. Matter* **10**, 6417 (1998).
- [148] D. Afanasiev et al., *Controlling the Anisotropy of a van Der Waals Antiferromagnet with Light*, *Science Advances* **7**, eabf3096 (n.d.).
- [149] X. Yan, X. Chen, and J. Qin, *Synthesis and Magnetic Properties of Layered MnPS_xSe_{3-x} (0 < x < 3) and Corresponding Intercalation Compounds of 2,2'-Bipyridine*, *Materials Research Bulletin* **46**, 235 (2011).
- [150] G. Kliche, *Infrared Spectra of the Hexachalcogenohypodiphosphate Mixed Crystals Co_{2-x}Ni_xP₂S₆ and Ni₂P₂S_{6-x}Se_x*, *Zeitschrift Für Naturforschung A* **38**, 1133 (1983).
- [151] B. Zapeka, M. Kostyrko, I. Martynyuk-Lototska, and R. Vlokh, *Critical Behaviour of Sn₂P₂S₆ and Sn₂P₂(Se_{0.28}S_{0.72})₆ Crystals under High Hydrostatic Pressures*, *Philosophical Magazine* **95**, 382 (2015).
- [152] B. Hillman, L. Noren, and D. J. Goossens, *Structural Properties of Compounds in the MPS_{3-x}Se_x Family*, (2011).
- [153] S. L. Dudarev, G. A. Botton, S. Y. Savrasov, C. J. Humphreys, and A. P. Sutton, *Electron-Energy-Loss Spectra and the Structural Stability of Nickel Oxide: An LSDA+U Study*, *Phys. Rev. B* **57**, 1505 (1998).
- [154] G. Kresse and J. Hafner, *Ab Initio Molecular Dynamics for Liquid Metals*, *Phys. Rev. B* **47**, 558 (1993).
- [155] G. Kresse and J. Furthmüller, *Efficiency of Ab-Initio Total Energy Calculations for Metals and Semiconductors Using a Plane-Wave Basis Set*, *Computational Materials Science* **6**, 15 (1996).

- [156] M. Birowska, K. Milowska, and J. Majewski, *Van Der Waals Density Functionals for Graphene Layers and Graphite*, Acta Physica Polonica A **120**, 845 (2011).
- [157] K. Milowska, M. Birowska, and J. A. Majewski, *Mechanical, Electrical, and Magnetic Properties of Functionalized Carbon Nanotubes*, AIP Conference Proceedings **1399**, 827 (2011).
- [158] M. Birowska, M. Marchwiany, C. Draxl, and J. A. Majewski, *Assessment of Approaches for Dispersive Forces Employing Graphene as a Case Study*, ArXiv:1707.09795 [Cond-Mat] (2020).
- [159] S. Grimme, J. Antony, S. Ehrlich, and H. Krieg, *A Consistent and Accurate Ab Initio Parametrization of Density Functional Dispersion Correction (DFT-D) for the 94 Elements H-Pu*, J. Chem. Phys. **132**, 154104 (2010).
- [160] N. Chandrasekharan and S. Vasudevan, *Magnetism and Exchange in the Layered Antiferromagnet NiPS₃*, J. Phys.: Condens. Matter **6**, 4569 (1994).
- [161] S. Kobayashi, H. Ueda, C. Michioka, and K. Yoshimura, *Competition between the Direct Exchange Interaction and Superexchange Interaction in Layered Compounds LiCrSe₂, LiCrTe₂, and NaCrTe₂ with a Triangular Lattice*, Inorg. Chem. **55**, 7407 (2016).
- [162] K. Kurosawa, S. Saito, and Y. Yamaguchi, *Neutron Diffraction Study on MnPS₃ and FePS₃*, Journal of the Physical Society of Japan **52**, 3919 (1983).
- [163] M. Birowska, P. E. Faria Junior, J. Fabian, and J. Kunstmann, *Large Exciton Binding Energies in MnPS₃ as a Case Study of a van Der Waals Layered Magnet*, Phys. Rev. B **103**, L121108 (2021).

- [164] T. Olsen, *Magnetic Anisotropy and Exchange Interactions of Two-Dimensional FePS₃, NiPS₃ and MnPS₃ from First Principles Calculations*, J. Phys. D: Appl. Phys. **54**, 314001 (2021).
- [165] T. G. Aminov, G. G. Shabunina, and E. V. Busheva, *Synthesis and Magnetic Properties of CuCr_{1.5}Sb_{0.5}S₄ – xSex solid Solutions*, Russ. J. Inorg. Chem. **57**, 1428 (2012).
- [166] C. Pughe et al., *Site-Selective D10/D0 Substitution in an S = 1/2 Spin Ladder Ba₂CuTe_{1-x}W_xO₆ (0 ≤ x ≤ 0.3)*, Inorg. Chem. **61**, 4033 (2022).
- [167] V. M. Katukuri, P. Babkevich, O. Mustonen, H. C. Walker, B. Fåk, S. Vasala, M. Karppinen, H. M. Rønnow, and O. V. Yazyev, *Exchange Interactions Mediated by Nonmagnetic Cations in Double Perovskites*, Phys. Rev. Lett. **124**, 077202 (2020).
- [168] C. Pellegrini, T. Müller, J. K. Dewhurst, S. Sharma, A. Sanna, and E. K. U. Gross, *Density Functional Theory of Magnetic Dipolar Interactions*, Phys. Rev. B **101**, 144401 (2020).
- [169] Y. Yu, G. Deng, Y. Cao, G. J. McIntyre, R. Li, N. Yuan, Z. Feng, J.-Y. Ge, J. Zhang, and S. Cao, *Tuning the Magnetic Anisotropy via Mn Substitution in Single Crystal Co₄Nb₂O₉*, Ceramics International **45**, 1093 (2019).
- [170] N. D. Mermin and H. Wagner, *Absence of Ferromagnetism or Antiferromagnetism in One- or Two-Dimensional Isotropic Heisenberg Models*, Phys. Rev. Lett. **17**, 1133 (1966).
- [171] Z. Zhang, J. Shang, C. Jiang, A. Rasmita, W. Gao, and T. Yu, *Direct Photoluminescence Probing of Ferromagnetism in Monolayer Two-Dimensional CrBr₃*, Nano Lett. **19**, 3138 (2019).
- [172] A. M. Ruiz, D. L. Esteras, A. Rybakov, and J. J. Baldoví, *Tailoring Spin Waves in 2D Transition Metal Phosphorus Trichalcogenides via Atomic-Layer Substitution*, Dalton Trans. **51**, 16816 (2022).

- [173] R. R. Rao and A. K. Raychaudhuri, *Magnetic Studies of a Mixed Antiferromagnetic System $Fe_{1-x}Ni_xPS_3$* , Journal of Physics and Chemistry of Solids **53**, 577 (1992).
- [174] S. Chaudhuri, C. N. Kuo, Y. S. Chen, C. S. Lue, and J. G. Lin, *Low-Temperature Magnetic Order Rearrangement in the Layered van Der Waals Compound $MnPS_3$* , Phys. Rev. B **106**, 094416 (2022).
- [175] H. Han et al., *Field-Induced Spin Reorientation in the Néel-Type Antiferromagnet $MnPS_3$* , Phys. Rev. B **107**, 075423 (2023).
- [176] F. Feringa, G. E. W. Bauer, and B. J. van Wees, *Observation of Magnetization Surface Textures of the van Der Waals Antiferromagnet $FePS_3$ by Spin Hall Magnetoresistance*, Phys. Rev. B **105**, 214408 (2022).
- [177] N. Wang et al., *Transition from Ferromagnetic Semiconductor to Ferromagnetic Metal with Enhanced Curie Temperature in $Cr_2Ge_2Te_6$ via Organic Ion Intercalation*, J. Am. Chem. Soc. **141**, 17166 (2019).
- [178] T. Marchandier, N. Dubouis, F. Fauth, M. Avdeev, A. Grimaud, J.-M. Tarascon, and G. Rousse, *Crystallographic and Magnetic Structures of the VI_3 and $LiVI_3$ van Der Waals Compounds*, Phys. Rev. B **104**, 014105 (2021).
- [179] Z. Li et al., *Imprinting Ferromagnetism and Superconductivity in Single Atomic Layers of Molecular Superlattices*, Advanced Materials **32**, 1907645 (2020).
- [180] C. Yang, X. Chen, J. Qin, K. Yakushi, Y. Nakazawa, and K. Ichimura, *Synthesis, Characterization, and Magnetic Properties of Intercalation Compound of 1,10-Phenanthroline with Layered $MnPS_3$* , Journal of Solid State Chemistry **150**, 281 (2000).

- [181] X. Zhang, H. Zhou, X. Su, X. Chen, C. Yang, J. Qin, and M. Inokuchi, *Synthesis, Characterization and Magnetic Properties of Transition Metal Salen Complexes Intercalated into Layered MnPS₃*, *Journal of Alloys and Compounds* **432**, 247 (2007).
- [182] J. S. O. Evans, D. O'Hare, R. Clement, A. Leautic, and P. Thuéry, *Origins of the Spontaneous Magnetization in MnPS₃ Intercalates: A Magnetic Susceptibility and Powder Neutron Diffraction Study***, *Advanced Materials* **7**, 735 (1995).
- [183] F. Xiong, H. Wang, X. Liu, J. Sun, M. Brongersma, E. Pop, and Y. Cui, *Li Intercalation in MoS₂: In Situ Observation of Its Dynamics and Tuning Optical and Electrical Properties*, *Nano Lett.* **15**, 6777 (2015).
- [184] Q. He, Z. Lin, M. Ding, A. Yin, U. Halim, C. Wang, Y. Liu, H.-C. Cheng, Y. Huang, and X. Duan, *In Situ Probing Molecular Intercalation in Two-Dimensional Layered Semiconductors*, *Nano Lett.* **19**, 6819 (2019).
- [185] C. Wang et al., *Monolayer Atomic Crystal Molecular Superlattices*, *Nature* **555**, 7695 (2018).
- [186] W. Bao et al., *Approaching the Limits of Transparency and Conductivity in Graphitic Materials through Lithium Intercalation*, *Nat Commun* **5**, 1 (2014).
- [187] M. Z. Shi, N. Z. Wang, B. Lei, C. Shang, F. B. Meng, L. K. Ma, F. X. Zhang, D. Z. Kuang, and X. H. Chen, *Organic-Ion-Intercalated FeSe-Based Superconductors*, *Phys. Rev. Materials* **2**, 074801 (2018).
- [188] L. Zhu, Q.-Y. Li, Y.-Y. Lv, S. Li, X.-Y. Zhu, Z.-Y. Jia, Y. B. Chen, J. Wen, and S.-C. Li, *Superconductivity in Potassium-Intercalated Td-WTe₂*, *Nano Lett.* **18**, 6585 (2018).
- [189] Y. Wang et al., *Modulation Doping via a Two-Dimensional Atomic Crystalline Acceptor*, *Nano Lett.* (2020).

- [190] C. Autieri, G. Cuono, C. Noce, M. Rybak, K. M. Kotur, C. E. Agrapidis, K. Wohlfeld, and M. Birowska, *Scarce Ferromagnetic Interactions in Monolayers of MPS₃ (M=Mn, Ni)*, ArXiv:2111.15004 [Cond-Mat] (2021).
- [191] M. Rajapakse, B. Karki, U. O. Abu, S. Pishgar, M. R. K. Musa, S. M. S. Riyadh, M. Yu, G. Sumanasekera, and J. B. Jasinski, *Intercalation as a Versatile Tool for Fabrication, Property Tuning, and Phase Transitions in 2D Materials*, Npj 2D Mater Appl **5**, 1 (2021).
- [192] A. Le Méhauté, G. Ouvrard, R. Brec, and J. Rouxel, *Insertion de lithium la structure lamellaire NiPS₃*, Materials Research Bulletin **12**, 1191 (1977).
- [193] P. J. S. Foot and B. A. Nevett, *Lithium Ion Diffusion in LixNiPS₃ Single Crystals*, Solid State Ionics **8**, 169 (1983).
- [194] A. H. Thompson and M. S. Whittingham, *Transition Metal Phosphorus Trisulfides as Battery Cathodes*, Materials Research Bulletin **12**, 741 (1977).
- [195] G. Ouvrard, E. Prouzet, R. Brec, S. Benazeth, and H. Dexpert, *X-Ray Absorption Study of Lithium Intercalated Thiophosphate NiPS₃*, Journal of Solid State Chemistry **86**, 238 (1990).
- [196] J. Li, W. Liu, X. Zhang, Y. Ma, Y. Wei, Z. Fu, J. Li, and Y. Yan, *Heat Treatment Effects in Oxygen-Doped β -Li₃PS₄ Solid Electrolyte Prepared by Wet Chemistry Method*, J Solid State Electrochem **25**, 1259 (2021).
- [197] G. Zhu, J. Liu, Q. Zheng, R. Zhang, D. Li, D. Banerjee, and D. G. Cahill, *Tuning Thermal Conductivity in Molybdenum Disulfide by Electrochemical Intercalation*, Nat Commun **7**, 1 (2016).
- [198] S. J. Clark, D. Wang, A. R. Armstrong, and P. G. Bruce, *Li(V_{0.5}Ti_{0.5})S₂ as a 1 V Lithium Intercalation Electrode*, Nat Commun **7**, 1 (2016).

- [199] I. Kerrache, C. Julien, and C. Sourisseau, *Raman Scattering Studies of Lithium-Intercalated NiPS₃*, *Solid State Ionics* **92**, 37 (1996).
- [200] X. Wang et al., *Spin-Induced Linear Polarization of Photoluminescence in Antiferromagnetic van Der Waals Crystals*, *Nat. Mater.* **20**, 7 (2021).
- [201] C. Berthier, Y. Chabre, and M. Minier, *NMR Investigation of the Layered Transition Metal Phosphorus Trichalcogenides and the Intercalation Compounds LixNiPS₃*, *Solid State Communications* **28**, 327 (1978).
- [202] A. R. Wildes, J. R. Stewart, M. D. Le, R. A. Ewings, K. C. Ruke, G. Deng, and K. Anand, *The Magnetic Dynamics of NiPS₃*, arXiv:2207.07448.
- [203] F. R. Gamble, J. H. Osiecki, and F. J. DiSalvo, *Some Superconducting Intercalation Complexes of TaS₂ and Substituted Pyridines*, *J. Chem. Phys.* **55**, 3525 (1971).
- [204] H. Boller and H. Blaha, *Intercalation Phases of TiS₂, 2H-NbS₂, and 1T-TaS₂ with Ethylenediamine and Trimethylenediamine: A Crystal Chemical and Thermogravimetric Study*, *Journal of Solid State Chemistry* **45**, 119 (1982).

Appendix A: All Publications Published, Submitted and Planned

1. **R Basnet**, T Patel, S Karki Chhetri, D Upreti, M.R.U. Nabi, G Acharya, J Sakon, J Wang, C Autieri, M Birowska, and J Hu “Understanding and tuning magnetism in layered Ising-type antiferromagnet FePSe₃ for potential 2D magnets” (Manuscript in preparation)
2. **R Basnet**, T Patel, S Karki Chhetri, D Upreti, M.R.U. Nabi, G Acharya, J Sakon, C Autieri, M Birowska, and J Hu “Field-induced ferromagnetism in Cr-substituted antiferromagnetic van der Waals material NiPS₃” (Manuscript in preparation)
3. **R Basnet**, D Baral, A Fereidouni, M. H. Doha, C Stephenson, S Bishop, K Pandey, M.R.U. Nabi, G Acharya, J Sakon, J Wang, H. O. H. Churchill, T Chein, and J Hu “Metal-insulator transition in Fe-doped Type-II Weyl Semimetal WTe₂” (Manuscript in preparation)
4. M.R.U. Nabi, **R Basnet**, K Pandey, S Karki Chhetri, D Upreti, G Acharya, F Wang, A Fereidouni, H. O. H. Churchill, Y Guan, Z Mao, and J Hu, “Coupling Between Magnetic and Transport Properties in Magnetic Layered Material Mn_{2-x}Zn_xSb” (Manuscript submitted to Acta Materialia)
5. Y Li, X Hu, A Fereidouni, **R Basnet**, K Pandey, J Wen, Y Liu, H Zheng, H. O. H. Churchill, J Hu, A. K. Petford-Long and C Phatak, “Visualizing the Effect of Oxidation on Magnetic Domain Behavior of Nanoscale Fe₃GeTe₂ for Applications in Spintronics”, ACS Applied Nano Material 6, 4390 (2023)
6. K Pandey, L Sayler, **R Basnet**, J Sakon, F Wang and J Hu, “Crystal Growth and Electronic Properties of LaSbSe” Crystals 12, 1663 (2022)
7. A Fereidouni, M. H. Doha, K Pandey, **R Basnet**, J Hu, and H. O. H. Churchill, “Enhancement of 2D topological semimetal transport properties by current annealing” Appl. Phys. Lett. 121, 113101 (2022)

8. **R Basnet***, D Ford, K TenBarge, J Lochala, and J Hu, “Emergence of Ferrimagnetism in Li-intercalated NiPS₃” J. Phys.: Condens. Matter 34, 434002 (2022) [*Invited paper for a special issue on 2D magnetic materials*]
9. **R Basnet**, K. M. Kotur, M Rybak, C Stephenson, S Bishop, C Autieri, M Birowska, and J Hu, “Controlling magnetic exchange and anisotropy by nonmagnetic ligand substitution in layered MPX₃ ($M = \text{Ni, Mn}; X = \text{S, Se}$)” Physical Review Research 4, 023256 (2022)
10. Y Li, **R Basnet**, K Pandey, J Hu, W Wang, X Ma, A.R.C. McCray, A.K. Petford-Long, and C Phatak, “Field-Dependent Magnetic Domain Behavior in van der Waals Fe₃GeTe₂” JOM 74, 2310 (2022)
11. A.R.C. McCray, Y Li, **R Basnet**, K Pandey, J Hu, D Phelan, X Ma, A.K. Petford-Long, and C Phatak, “Thermal Hysteresis Behavior of Skyrmion Lattices in the van der Waals Ferromagnet Fe₃GeTe₂” Nano Letters 22, 7804 (2022)
12. K Pandey, **R Basnet**, J Wang, B Da, and J Hu, “Evolution of electronic and magnetic properties in the topological semimetal SmSb_xTe_{2-x}” Phys. Rev. B 105, 155139 (2022)
13. M.R.U. Nabi, A Wegner, F Wang, Y Zhu, Y Guan, A Fereidouni, K Pandey, **R Basnet**, G Acharya, H.O.H. Churchill, Z Mao, and J Hu, “Giant topological Hall effect in centrosymmetric tetragonal Mn_{2-x}Zn_xSb” Phys. Rev. B 104, 174419 (2021)
14. Z Ye, W Peng, F Wang, A Balodhi, **R Basnet**, J Hu, A Zevalkink, and J Wang, “Quasi-layered Crystal Structure Coupled with Point Defects Leading to Ultralow Lattice Thermal Conductivity in n-Type Cu_{2.83}Bi₁₀Se₁₆” ACS Appl. Energy Mater. 4, 10 (2021)
15. K Pandey, D Mondal, J.W. Villanova, J Roll, **R Basnet**, A Wegner, G Acharya, M.R.U. Nabi, B Ghosh, J Fujii, J Wang, B Da, A Agarwal, I Vobornik, A Politano, S.B-Lopez, and J

- Hu, "Magnetic Topological Semimetal Phase with Electronic Correlation Enhancement in SmSbTe" *Adv. Quantum Technol.* 4, 2100063 (2021)
16. S. H. Lee, D. Graf, L. Min, Y. Zhu, H. Yi, S. Ciocys, Y. Wang, E. S. Choi, **R. Basnet**, A. Fereidouni, A. Wegner, Y.-F. Zhao, K. Verlinde, J. He, D. Graf, R. Redwing, V. Gopalan, H. O. H. Churchill, A. Lanzara, N. Samarth, C.-Z. Chang, J. Hu, and Z.Q. Mao, "Evidence for a Magnetic-Field induced Type-II Weyl State in Antiferromagnetic Topological Insulator $\text{Mn}(\text{Bi}_{1-x}\text{Sb}_x)_2\text{Te}_4$ " *Phys. Rev. X* 11, 031032 (2021)
17. **R Basnet**, T.T. McCarthy, Z Ju, Y-H Zhang, S-Q Yu, and J Hu, "Electronic Properties of Group-IV SnGe alloy topological quantum materials," 2021 IEEE Photonics Society Summer Topicals Meeting Series (SUM), pp. 1-2 (2021)
18. **R Basnet**, A Wegner, K Pandey, S Storment, and J Hu, "Highly sensitive spin-flop transition in antiferromagnetic van-der Waals material MPS_3 ($M = \text{Ni}$ and Mn)" *Phys. Rev. Materials* 5, 064413 (2021)
19. Y. Wang, J. Balgley, E. Gerber, M. Gray, N. Kumar, X. Lu, J.-Q. Yan, A. Fereidouni, **R. Basnet**, S. J. Yun, D. Suri, H. Kitadai, T. Taniguchi, K. Watanabe, X. Ling, J. Moodera, Y. H. Lee, H. O. H. Churchill, J. Hu, L. Yang, E.-A. Kim, D. G. Mandrus, E. A. Henriksen, and K. S. Burch, "Modulation Doping via a Two-Dimensional Atomic Crystalline Acceptor" *Nano Letters* 20, 8446 (2020)
20. K. Pandey, **R. Basnet***, A. Wegner, G. Acharya, M. R. U. Nabi, J. Liu, J. Wang, Y. Takahashi, B. Da, and J. Hu*, "Electronic and magnetic properties of the topological semimetal candidate NdSbTe" *Physical Review B* 101, 235161 (2020)

* *Corresponding author*

21. S. Davari, J. Stacy, A. M. Mercado, J. D. Tull, **R. Basnet**, K. Pandey, J. Hu, and H. O. H. Churchill, “Gate-defined, accumulation mode quantum dots in monolayer and bilayer WSe₂” *Physical Review Applied* 13, 054058 (2020)
22. **R. Basnet**, M. H. Doha, T. Hironaka, K. Pandey, S. Davari, K.M. Welch, H. O. H. Churchill*, and J. Hu*, “Growth and Strain Engineering of Trigonal Te for Topological Quantum Phases in Nonsymmorphic Chiral Crystals” *Crystals* 9, 486 (2019)